NIELS LÖRCH

LASER THEORY FOR QUANTUM OPTOMECHANICS

LASER THEORY FOR QUANTUM OPTOMECHANICS

Von der QUEST-Leibniz-Forschungsschule der
Gottfried Wilhelm Leibniz Universität Hannover
zur Erlangung des akademischen Grades
Doktor der Naturwissenschaften
Dr. rer. nat.
genehmigte Dissertation von

Dipl.-Phys. Niels Lörch
geboren am 30. April 1985 in Karlsruhe, Deutschland

2015

Referent: Prof. Dr. Klemens Hammerer
(Universität Hannover, ITP und AEI)
Korreferent: Dr. Andreas Nunnenkamp
(University of Cambridge, Cavendish Laboratory)
Korreferent: Prof. Dr. Manfred Lein
(Universität Hannover, ITP)
Vorsitzender der Prüfungskommission: Prof. Dr. Piet Schmidt
(Universität Hannover und PTB Braunschweig)
Tag der Disputation: 22.7.2015

ABSTRACT

This thesis contributes to the field of quantum optomechanics, which studies the interaction of light with mechanical oscillators. In the first part we derive an analytical model to describe optically driven self-sustained oscillations of a mechanical object, which can be understood as the phonon analogue of lasing. Accordingly our model is based on methods first developed in the context of the laser. We examine different experimental setups to prepare non-classical mechanical states in this phonon laser phase and find surprisingly weak conditions on the experimental system parameters to detect quantum signatures such as phonon antibunching and negative density of the mechanical oscillator's Wigner function.

In the second part of the thesis we study the neighboring field of trapped ions. Measuring the recoil of an ion when scattering a photon, a new high precision spectroscopy method (photon recoil spectroscopy) was recently demonstrated. A subtle Doppler-induced systematic frequency shift that occurs in this experiment is theoretically analyzed with an adapted laser theory model. Finally, we present and analyze an efficient quantum algorithmic readout mechanism for multi-ion clocks, which promise record time keeping accuracy.

keywords: laser theory, quantum optomechanics, trapped ions

ZUSAMMENFASSUNG

Dies ist ein Beitrag auf dem Gebiet der Quanten-Optomechanik, welches die Interaktion von Licht mit mechanischen Oszillatoren untersucht. Im ersten Teil der Dissertation entwickeln wir ein Modell zur Beschreibung optisch getriebener, sich selbst erhaltender Oszillationen eines mechanischen Objekts, die als phononisches Analogon eines Laser-Zustands verstanden werden können. Folgerichtig basiert unser Modell auf Methoden, die ursprünglich im Kontext des Lasers entwickelt wurden. Wir untersuchen verschiedene experimentelle Setups auf ihre Eignung nicht-klassische Zustände mechanischer Objekte in der Phononen-Laser-Phase zu erzeugen. Es stellt sich heraus, dass die Anforderungen an die Systemparameter überraschend schwach sind, um Quanteneffekte wie zum Beispiel Antibunching von Phononen oder eine negative Dichte der mechanischen Wignerfunktion nachzuweisen.

Der zweite Teil dieser Dissertation befasst sich mit dem benachbarten Gebiet gefangener Ionen. Eine neue, hochpräzise Spektroskopie-Methode (Photonen-Rückstoß-Spektroskopie) basiert auf der Messung des Impulsübertrags auf ein Ion bei Absorption eines Photons. In diesem Experiment entsteht eine systematische Verschiebung der Resonanzfrequenz durch einen subtilen Einfluss des Doppler-Effekts. Wir analysieren diese Verschiebung mit einem für Ionenfallen adaptierten Lasertheorie-Modell. Schließlich präsentieren und analysieren wir einen effizienten Quanten-Algorithmus zum Auslesen von Multi-Ionen Uhren, die ein Kandidat für die nächste Definition des Zeitstandards sind.

Schlagworte: Laser Theorie, Quanten-Optomechanik, gefangene Ionen

PUBLICATIONS

This thesis is based on the following publications:
Chapters 3 and 4 are based on reference [1], where I contributed the main analytical and numerical results.
Chapter 5 is based on reference [2], where I contributed the main analytical and numerical results.
Chapter 6 is based on reference [3], where the spectroscopy experiment was performed by the group of Piet Schmidt at PTB. Together with Klemens Hammerer I modeled and explained analytically a systematic shift in the measured resonance frequency. Together with Yong Wan and Piet Schmidt I performed the numerical simulations. All authors contributed to the discussion and interpretation of the results, and the writing of the manuscript.
Chapter 7 is based on reference [4], where I contributed to the idea of the readout mechanism, which was calculated by Marius Schulte in his Bachelor thesis [5]. I contributed the main part of the numerical analysis.

ACKNOWLEDGMENTS

First and foremost, I thank my PhD supervisor Klemens Hammerer for giving me the opportunity to learn from his deep knowledge of physics and always taking the time to answer my questions, for teaching me novel subjects and sharing interesting ideas. I am very grateful for all his support throughout this thesis and especially for creating a fantastic atmosphere in his research group. It has been a great pleasure to work in such an enthusiastic environment.

I thank Piet Schmidt for taking us on board his experimental ion trap projects, the joyful collaboration and all his help throughout my thesis.

I thank Aashish Clerk, Florian Marquardt, and Jiang Qian for the fun collaboration on optomechanical limit cycles and sharing their great physical intuition with me on this subject.

I thank Andreas Nunnenkamp for the fruitful discussions on optomechanics, his hospitality during my visit and for agreeing to referee my thesis.

I thank Manfred Lein for agreeing to referee my thesis.

I thank all my colleagues and former colleagues at Hannover: André Xuereb, Denis Vasilyev, and Sebastian Hofer especially for helping me to get started on quantum optomechanics and numerical analysis with Python as a new PhD student. I thank Marius Schulte and Yong Wan for working with me on ion clocks and ion spectroscopy, which I enjoyed very much. I thank Birgit Gemmeke for all her help at the institute. I thank all group members and colleagues at AEI not directly involved in this thesis for making my time in Hannover so very enjoyable.

I am very grateful to my family and my wife Linyao for their support throughout many years and in particular during these last couple of weeks of writing the thesis.

I would like to thank the the cluster system team at the Leibniz University of Hannover for their support in the production of this work and the Centre for Quantum Engineering and Space-Time Research (QUEST) at the Leibniz University Hannover for funding.

CONTENTS

1 INTRODUCTION AND OUTLINE 1

I INTRODUCTION TO QUANTUM OPTOMECHANICS 5

2 STANDARD DESCRIPTION OF QUANTUM OPTOMECHANICAL SYSTEMS 7
- 2.1 The standard optomechanical master equation 8
  - 2.1.1 Optical modes: $\mathcal{L}_c$ 8
  - 2.1.2 Mechanical Oscillator: $\mathcal{L}_m$ 8
  - 2.1.3 Optomechanical Interaction: $\mathcal{L}_i$ 9
  - 2.1.4 Linearized Interaction 10
  - 2.1.5 Optomechanical Sideband-Cooling and Onset of Self-Sustained Oscillations 12
  - 2.1.6 Optomechanical Bistability 15
- 2.2 Physical Realizations 16
  - 2.2.1 Model system: Fabry-Pérot cavity coupled to end mirror 16
  - 2.2.2 Optomechanical setups 17
  - 2.2.3 Trapped ions 19
- 2.3 Outline of the following contributions 22
  - 2.3.1 Self-sustained optomechanical oscillations . . . 22
  - 2.3.2 Ion spectroscopy 22
  - 2.3.3 Ion clocks 23
- 2.A Phase space distributions 25
  - 2.A.1 Definition 25
  - 2.A.2 Calculation of moments 26
  - 2.A.3 Equations of motion 26
  - 2.A.4 Basic properties 27
- 2.B Adiabatic Elimination 28
  - 2.B.1 Introduction to the projection operator method 29
  - 2.B.2 Adiabatic Elimination in phase space 31
- 2.C Numerical Analysis 33
  - 2.C.1 Quantum trajectories 34
  - 2.C.2 Langevin equations 35

II OPTOMECHANICAL SELF-SUSTAINED OSCILLATIONS 37

3 LASER THEORY FOR OPTOMECHANICS 39
- 3.1 Introduction 39
- 3.2 Laser Theory for Optomechanics 41
  - 3.2.1 Haake-Lewenstein Laser Theory Ansatz in Optomechanics 41
  - 3.2.2 Fokker-Planck Equation for the Mechanical Oscillator 45
- 3.3 Conclusion 50

3.A Quantum limit cycles in lasers 51
3.B Semi-Polaron Transformation 52
3.C Transformations for general phase space distribution . 52
3.D Derivation of Fokker-Planck equation 55
4 QUANTUM SIGNATURES IN OPTOMECHANICAL LIMIT CYCLES 59
4.1 Introduction 59
4.2 Outline 60
4.3 Drift and dynamical detuning 63
4.4 Diffusion and Fano factor 64
4.5 Nonpositive Wigner Function 68
4.6 Numerical Analysis 71
4.7 Conclusions 73
5 SUB-POISSONIAN PHONON LASING IN THREE-MODE OPTOMECHANICS 75
5.1 Introduction 75
5.2 System description 76
5.3 Calculation of classical amplitudes 77
5.4 Calculation of quantum amplitude noise 78
5.5 Additional Laser Cooling 80
5.6 Experimental feasibility 81
5.7 Readout of phonon statistics 82
5.8 Outlook and Conclusion 83
5.A Phonon statistics and Numerical Analysis 85

III ION SPECTROSCOPY AND CLOCKS 87
6 PHOTON RECOIL SPECTROSCOPY 89
6.1 Introduction 89
6.1.1 Two point sampling method 90
6.2 The theoretical model 91
6.3 Equation of motion in phase space 92
6.4 Adiabatic elimination of the internal state 94
6.5 Approximate solution as a Gaussian time evolution . . 96
6.6 Quantifying the systematic shift 97
7 QUANTUM ALGORITHMIC READOUT OF MULTI-ION CLOCKS 101
7.1 Introduction 101
7.2 The abstract and idealized readout mechanism 102
7.3 Physical implementation of the readout mechanism . . 103
7.4 Case study: Al^+-Ca^+ clock 105
7.4.1 Normal modes for transversal oscillations . . . 105
7.4.2 Results for our example configuration 107
7.5 Numerical readout noise simulation 108
7.6 Conclusion 109
8 CONCLUSION AND OUTLOOK 111

BIBLIOGRAPHY 113

1

INTRODUCTION AND OUTLINE

Quantum theory describes the laws of nature governing the microscopic world populated by objects such as photons or atoms. Macroscopic objects (cats, etc.) on the other hand cannot be isolated. Therefore any possible quantum coherence is lost on an extremely short timescale due to interaction with the unavoidable environment [6, 7]. For this reason tests of quantum theory on macroscopic scales have been extremely limited. With advancing technology experimentalists have been adding increasingly heavy objects (Fullerenes and larger molecules [8], mechanical oscillators visible to the human eye [9]) to the zoo of tamed quantum systems and it is an exciting research perspective to keep pushing this frontier of quantum mechanics: Will we encounter a fundamental border between the microscopic and macroscopic realm so that quantum theory has to be altered [10, 11] or extended at some scale? Or are we only limited by human technological capabilities to isolate and control [12, 6] larger experiments?

Optomechanical systems [13, 14], consisting in their most basic form of an optical cavity mode coupled to a resonance mode of a mechanical oscillator, are very promising for this endeavor: Spectacular progress is being made in increasing the coupling strength of light to larger-scale, well-isolated mechanical objects. Using red detuned laser-light with respect to the cavity resonance it is possible to extract energy from the mechanical oscillator to realize an optical cooling mechanism. In recent years even optical cooling to the quantum ground state has been achieved [15, 16]. Near the ground state quantum effects such as coherent transfer of quantum states between light and mechanics [17, 18], light-matter entanglement [19], and observation of radiation pressure shot noise on the oscillator [20, 21] have been demonstrated on unprecedented mass scales.

Experiments on the reversed process [22, 23, 24, 25, 26, 27, 28, 29, 30], where mechanical oscillations are driven with blue detuned light can be understood as the phonon analogue of lasing with the optical cavity playing the role of the gain medium that pumps the mechanical oscillator into a highly excited state. Such setups are now reaching quantum level precision, even readout of the phonon statistics [30] has been demonstrated to prove the coherence in these mechanical oscillations. In future experiments it will be most exciting to create phonon laser states with truly quantum signatures such as phonon anti-bunching or negative density of the mechanical oscillator's Wigner function.

In this thesis we contribute to the theory of optomechanical oscillations. Exploiting the aforementioned laser analogy, we derive in Chapter 3 an analytical model based on techniques due to Haake and Lewenstein [31] first developed in the context of lasers. In this framework the gain medium is treated as a density matrix, while the laser state is described in a phase space picture by means of a Fokker-Planck equation. The model allows for a flexible treatment of the oscillator's back-action on the gain medium and correctly describes optomechanical oscillations in the quantum regime. It provides a natural starting point for further studies of quantum effects in optomechanics.

In Chapter 4 we apply laser theory to the standard optomechanical setup, where one optical and one mechanical mode are coupled dispersively, we compare the analytical model with numerical simulations and find very good agreement over a wide and previously unexplored regime of system parameters. As one main conclusion, we predict negative Wigner functions to be observable even for surprisingly classical parameters, i.e. outside the single-photon strong-coupling regime, for strong cavity drive and rather large limit-cycle amplitudes.

For verification of these analytical results we used (Monte-Carlo) Quantum Jump Trajectories as implemented in QuTiP [32, 33]. We optimized this numerical method to simulate optomechanical systems in the numerically most challenging regime on the border between quantum and classical parameters. As it is neither sufficient to expand the system on a small Hilbert space nor to simulate classical phase space trajectories, we developed an algorithm that dynamically adapts the numerical Hilbert space following the quantum trajectories.

In Chapter 5 we conclude the study of optomechanical limit cycles with a proposition to make use of the enhanced nonlinearity of an optomechanical system with two cavity modes. We find that this setup allows for sub-Poissonian limit cycle states with small mechanical amplitudes, making it an ideal candidate for the demonstration of phonon antibunching in future experiments.

Alongside the study of quantum physics on macroscopic scales, the field of optomechanics offers great perspectives with regard to many applications [34]. In particular we will consider here setups of trapped ions [35, 36], which in a wider sense can be viewed as optomechanical systems: The ions' internal energy states are coupled to their motional degrees of freedom via the momentum transfer upon absorption of photons e.g. from a laser tuned to a transition frequency. Due to their small size, ions can be very well isolated from their environment. In consequence trapped ions are among the best controlled quantum systems to date with applications ranging from optical clocks [37] to spectroscopy experiments [38] and even prototypes for quantum computers and simulators [36]. In the second part of this thesis we study two metrology experiments developed at PTB:

In Chapter 6 we study a spectroscopy experiment [3] with trapped ions, which demonstrated a new method to measure an ion's internal level structure via the transferred momentum of a photon when absorbed by the ion. This photon recoil spectroscopy experiment is an extension of quantum logic spectroscopy to a wider class of objects, allowing spectroscopy also on short-lived transitions of ions or molecules. Use of the effective two point sampling method results in a systematic error of the resonance frequency, which must be corrected to obtain a reasonable result. Adapting the model developed in Chapter 3 to the situation of trapped ions, we can attribute the systematic error to a subtle Doppler induced shift.

Optical ion clocks are a candidate for the next definition of the time standard. Clocks based on a single ion have been built and multiple ion clocks are soon to come. Due to unavoidable electric field gradients in ion traps, the electric quadrupole moments of the clock ions have to be negligible to avoid systematic frequency shifts. This severely limits the choice of clock ion species and for most suitable species the readout has to be done indirectly via co-trapped logic ions. In Chapter 7 we present and analyze an efficient scheme for a setup with multiple clock ions, which is based on a quantum algorithm first developed in the context of entanglement concentration to read out the Hamming weight.

In the following Chapter 2 we review some basic results in the field of optomechanical systems and introduce some textbook methods of quantum optics before presenting our new contributions presented in Chapters 3-7, which are based on the publications [1], [2], [3] and [4].

Part I

INTRODUCTION TO QUANTUM OPTOMECHANICS

2

STANDARD DESCRIPTION OF QUANTUM OPTOMECHANICAL SYSTEMS

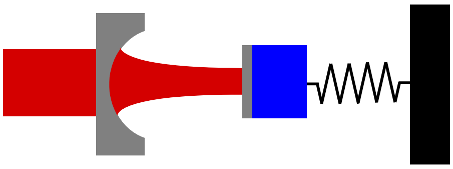

Figure 1: Schematic drawing of the most basic optomechanical system: An optical mode (red) trapped inside a Fabry-Pérot cavity couples to a movable mechanical object (blue), in this case one of the cavities' end mirrors.

Optomechanical systems are, as the name suggests, composed of optical and mechanical degrees of freedom that are coupled to each other. The most basic example is schematically depicted in Figure 1. Before introducing the various concrete physical setups that realize this concept, we develop their theoretical description with the quite general formalism of Lindblad master equations as our starting point following standard treatments found e.g. in the reviews [13, 14]. In this formalism the time derivative of the density matrix ρ, describing the state of the composite optomechanical system, is given by a Lindblad (super-) operator $\mathcal{L}$ acting on ρ:

$$\dot{\rho} = \mathcal{L}\rho. \tag{1}$$

It is convenient to decompose

$$\mathcal{L} = \mathcal{L}_c + \mathcal{L}_m + \mathcal{L}_i \tag{2}$$

into an operator $\mathcal{L}_c$ acting only on the optical (cavity) degrees of freedom, an operator $\mathcal{L}_m$ acting only on the mechanics and an interaction operator $\mathcal{L}_i$ describing the optomechanical coupling.

Both optical and mechanical systems exist in a multitude of physical realizations. Also the optomechanical coupling can be achieved in different ways. Nevertheless a small set of Lindblad operators can describe most experiments of the field. In the following three sections we introduce these variations of $\mathcal{L}_c, \mathcal{L}_m$ and $\mathcal{L}_i$, which are also sufficient for all setups discussed in this thesis. For convenience of notation the dimension of all Lindblad and Hamiltonian terms will be frequency (and not energy).

2.1 THE STANDARD OPTOMECHANICAL MASTER EQUATION

2.1.1 *Optical modes:* $\mathcal{L}_c$

The time evolution of a free optical mode a of frequency ω_c is given by the Hamiltonian

$$H_c = \omega_c \hat{a}^\dagger \hat{a}, \tag{3}$$

where $\hat{a}$ ($\hat{a}^\dagger$) is the annihilation (creation) operator of mode a. When such a mode is associated with a cavity, the tunneling of photons in and out of the cavity can be described by the operator

$$\begin{aligned} L_c\rho = {} & \kappa\left(1+\bar{n}_c\right)\left(\hat{a}\rho\hat{a}^\dagger - \tfrac{1}{2}\hat{a}^\dagger\hat{a}\rho - \tfrac{1}{2}\rho\hat{a}^\dagger\hat{a}\right) \\ & +\kappa\bar{n}_c\left(\hat{a}^\dagger\rho\hat{a} - \tfrac{1}{2}\hat{a}\hat{a}^\dagger\rho - \tfrac{1}{2}\rho\hat{a}\hat{a}^\dagger\right) \end{aligned} \tag{4}$$

as the interaction with the outside modes is usually Markovian. Here $\bar{n}_c = (e^{\hbar\omega_c/k_B T} - 1)^{-1}$ is the occupation number of the surrounding thermal radiation environment. Disregarding technical laser noise, in the optical domain $\bar{n} \approx 0$ even at room temperature. In the microwave domain however, where frequencies are lower, one cannot neglect $\bar{n}_c$. We denote the cavity energy decay rate with κ.

A laser drive of power P_L and frequency ω_L is modeled by the additional time-dependent Hamiltonian

$$H_L(t) = -iE\hat{a}e^{-i\omega_L t} + \text{h.c.}, \tag{5}$$

where $E = \sqrt{2\kappa P_L/\hbar\omega_L}$ parameterizes the laser strength and we neglect the laser's line width. In a frame rotating at the laser frequency ω_L with $\rho \to e^{i\omega_L t}\rho e^{-i\omega_L t}$, the total cavity Lindblad operator is time independent and given by

$$\mathcal{L}_c\rho = -i\left[-\Delta\hat{a}^\dagger\hat{a} + iE\left(\hat{a}^\dagger - \hat{a}\right), \rho\right] + L_c\rho, \tag{6}$$

where $\Delta = \omega_L - \omega_c$ is the detuning of the laser with respect to the cavity. If the cavity is driven at more than one frequency, the laser can be described as a slowly (on the scale of ω_l) varying amplitude $E = E(t)$ and hence the cavity Lindblad operator is time dependent.

2.1.2 *Mechanical Oscillator:* $\mathcal{L}_m$

The motion along one dimension of a mechanical object of mass m in a harmonic potential $V = \frac{1}{2}kx^2$ is described by the Hamiltonian

$$H_m = \omega_m \hat{b}^\dagger \hat{b} \tag{7}$$

for the mechanical mode b, where the frequency is given by $\omega_m = \sqrt{k/m}$. A mechanical system composed of N subsystems with harmonic interaction can always be decomposed into normal modes b_j.

While the effective mass of these normal modes depends on the scale used to measure their displacement, the frequency of each normal mode is uniquely defined.

Each mode also unavoidably interacts with its environment. E.g. scattering events with the gas molecules of the surrounding atmosphere or with phonons from modes that are not considered as part of the system can be effectively described by a mechanical damping γ that couples the mode to its environment with phononic occupation number $\bar{n}_m$. In analogy to Equation (4) the corresponding Lindblad operator is

$$\begin{aligned} L_m\rho = \gamma\,(1+\bar{n}_m)\left(\hat{b}\rho\hat{b}^\dagger - \tfrac{1}{2}\hat{b}^\dagger\hat{b}\rho - \tfrac{1}{2}\rho\hat{b}^\dagger\hat{b}\right) \\ +\gamma\bar{n}_m\left(\hat{b}^\dagger\rho\hat{b} - \tfrac{1}{2}\hat{b}\hat{b}^\dagger\rho - \tfrac{1}{2}\rho\hat{b}\hat{b}^\dagger\right). \end{aligned} \tag{8}$$

In combination with the harmonic evolution the full Lindblad operator for a harmonic mechanical mode is

$$\mathcal{L}_m\rho = -i\left[\omega_m\hat{b}^\dagger\hat{b},\rho\right] + L_m\rho. \tag{9}$$

In order to obtain good control of the mechanical oscillator the damping to its environment should be small. One way to quantify this quality is given by the quality factor (Q-factor)

$$Q_m = \omega_m/\gamma, \tag{10}$$

which corresponds to the number of oscillations a phonon survives during its lifetime.

2.1.3 *Optomechanical Interaction: $\mathcal{L}_i$*

Most commonly in today's experiments the dominant interaction is dispersive: The position of the mechanical system couples to the energy of the optical system (and not e.g. to its decay rate, which would be "dissipative coupling"). The simplest such interaction Hamiltonian

$$H_i = -g_0\hat{a}^\dagger\hat{a}(\hat{b}+\hat{b}^\dagger), \tag{11}$$

couples the number of photons $\hat{n} = \hat{a}^\dagger a$ of an optical mode to the position $\hat{x} = \hat{b}+\hat{b}^\dagger$ of a mechanical mode. Here g_0 denotes the coupling constant on the level of single quanta. Coupling to higher orders of the position are negligible for the situation studied in this thesis, we note however that alternative experimental setups exist where e.g. a term quadratic in $\hat{x}$ proportional to $\hat{a}^\dagger\hat{a}(\hat{b}+\hat{b}^\dagger)^2$ or higher order terms cannot be neglected or may even be dominant.

The general multimode version of Equation (11) is

$$H_i = \sum_{j,k,l} - [g_0]^l_{jk}\,\hat{a}^\dagger_j\hat{a}_k(\hat{b}_l+\hat{b}^\dagger_l), \tag{12}$$

where $[g_0]_{jk}$ is a Hermitian Matrix for each l. While in almost all realistic optomechanical systems many modes are present and thus Equation (12) should be used, it is often possible to use Equation (11) as a very good approximation if only one mechanical mode is addressed. In this thesis we will encounter both situations, in any case the Lindblad interaction operator only has the Hamiltonian contribution and

$$\mathcal{L}_i\rho = -i\left[H_i, \rho\right]. \tag{13}$$

2.1.4 *Linearized Interaction*

For the standard system consisting of one optical and one mechanical mode as described by the master equation $\dot{\rho} = \left(\mathcal{L}_c + \mathcal{L}_m + \mathcal{L}_i\right)\rho$ with Lindblad operators

$$\mathcal{L}_c\rho = -i\left[-\Delta a^\dagger a + iE\left(a^\dagger - a\right), \rho\right] + L_c\rho, \tag{14}$$

$$\mathcal{L}_m\rho = -i\left[\omega_m b^\dagger b, \rho\right] + L_m\rho, \tag{15}$$

$$\mathcal{L}_i\rho = -i\left[-g_0 a^\dagger a\left(b + b^\dagger\right), \rho\right], \tag{16}$$

it is often possible to approximate the interaction Hamiltonian by its linearized version: If the amplitude $\beta = \langle b\rangle$ of the mechanical oscillations is small on the scale of ω_m/g_0, its modulation of the optical amplitude $\alpha = \langle a\rangle$ is also small. For this situation the linearization around *time-constant* mean amplitudes α_0 and β_0 is a good approximation.

Formally this is achieved by switching to a displaced frame

$$\tilde{\rho} = D(-\alpha_0)\otimes D(-\beta_0)\rho D(-\alpha_0)^\dagger \otimes D(-\beta_0)^\dagger. \tag{17}$$

for both cavity and oscillator, where $\hat{D}(\alpha) = \exp\left(\alpha\hat{a}^\dagger - \alpha^*\hat{a}\right)$ denotes the displacement operators for the respective systems. We demand that all displacement terms (those proportional to a single destruction or creation operator) in the master equation for $\tilde{\rho}$ drop out, so that the system undergoes no DC-drift of its mean amplitudes. This condition is met if α_0 and β_0 fulfill the set of equations

$$\alpha_0 = \frac{E}{\kappa/2 - i\left(\Delta + 2g_0\Re\left(\beta_0\right)\right)}, \tag{18}$$

$$\beta_0 = \frac{g_0|\alpha_0|^2}{(\omega_m - i\gamma/2)}. \tag{19}$$

Depending on the system parameters, this can have not only one but three different solutions for (α_0, β_0), making the system bistable [1], which is further discussed in Section 2.1.6. Here we proceed assuming a unique solution. We note that this bistability is relevant only for red detuning.

---

[1] Only two solutions are stable.

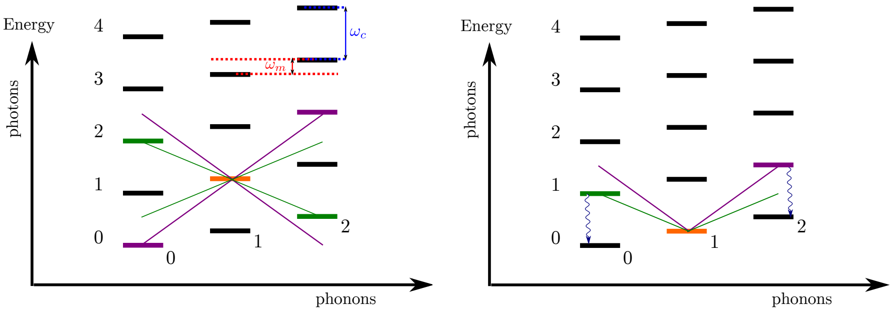

(a) Detailed level scheme.

(b) Optomechanical cooling and heating.

Figure 2: a) The energy levels of photons and phonons are plotted along the two axes, with energy ω_m for each mechanical excitation and energy ω_c for each photon. We choose the orange energy level as a starting point to illustrate both the state swap and the two mode squeezing interaction: For both the green ($\Delta = -\omega_m$) and the purple ($\Delta = +\omega_m$) lines all four possible transitions are drawn and the resonant levels are highlighted in the respective color.
b) If the cavity is effectively in the (displaced) vacuum state, only the transitions where one photon is created can contribute. Thus the state swap interaction realizes cooling and the two-mode squeezing interaction realizes excitation of mechanical motion, as illustrated in this Figure. The curved arrows symbolize the loss of photons due to the cavity decay.

Defining the effective detuning as $\tilde{\Delta} = \Delta + 2g_0\Re(\beta)$, the linear coupling enhanced by the coherent amplitude as $g = g_0|\alpha|$, as well as phase-adjusted annihilation operator $\tilde{a} = -\frac{\alpha^*}{|\alpha|}a$, the master equation for $\tilde{\rho}$ with amplitudes according to (18) and (19) is

$$\mathcal{L}_c\tilde{\rho} = -i\left[-\tilde{\Delta}\tilde{a}^\dagger\tilde{a}, \tilde{\rho}\right] + L_c\tilde{\rho}, \tag{20}$$

$$\mathcal{L}_m\tilde{\rho} = -i\left[\omega_m b^\dagger b, \tilde{\rho}\right] + L_m\tilde{\rho}, \tag{21}$$

$$\mathcal{L}_i\tilde{\rho} = -i\left[g\left(\tilde{a} + \tilde{a}^\dagger\right)\left(b + b^\dagger\right), \tilde{\rho}\right], \tag{22}$$

where we neglected a term $-g_0 a^\dagger a\left(b + b^\dagger\right)$ in the Hamiltonian. This is justified if two conditions are met:

- The optical amplitude $|\alpha_0| \gg 1$ is large enough so that $g \gg g_0$, making the g-term dominant.
- The mechanical oscillation is small on the scale of g_0/ω_m, so that its modulation of the optical detuning can be neglected.

Note that Equations (20)-(22) form a time-independent set of linearized equations that can describe the system dynamics.

Finally, in an interaction picture where $\rho' = e^{iH_0t}\tilde{\rho}e^{-iH_0t}$ with respect to $H_0 = \omega_m\hat{b}^\dagger\hat{b} - \tilde{\Delta}\hat{a}^\dagger\hat{a}$ all Hamiltonian terms except for the interaction cancel and the interaction becomes time dependent, so that the dynamics of the system is given by the set

$$\mathcal{L}_c = L_c, \tag{23}$$

$$\mathcal{L}_m = L_m, \tag{24}$$

$$H_i = -g\left(\tilde{a}^\dagger b e^{-i(\tilde{\Delta}+\omega_m)t} + \tilde{a}^\dagger b^\dagger e^{-i(\tilde{\Delta}-\omega_m)t}\right) + \text{h.c.} \tag{25}$$

Operating the laser at a detuning where $\tilde{\Delta} = -\omega_m$ the $\tilde{a}^\dagger b + \text{h.c.}$ term becomes resonant, which is a state swap interaction, i.e. it swaps the states of the two systems. This can be used e.g. for laser cooling, where the vacuum state of the cavity is swapped onto the thermal state of the mechanical oscillator [15, 16] and the mechanical oscillator's energy is dissipated by the cavity mode into the environment. For $\tilde{\Delta} = \omega_m$ the $\tilde{a}^\dagger b^\dagger + \text{h.c.}$ term becomes resonant, which is a two mode squeezing interaction that can entangle [19] the two systems and excite oscillations of the mechanical oscillator. At $\tilde{\Delta} = 0$ the interaction is balanced, which can be used for quantum non-demolition measurements [39]. The regimes $\tilde{\Delta} = \pm\omega_m$ are visualized in Figure 2 and quantitatively treated in the following Section 2.1.5.

2.1.5 *Optomechanical Sideband-Cooling and Onset of Self-Sustained Oscillations*

Let us assume that initially the mechanical oscillator is near the ground state. We may thus start from the fact, at least for small times, that the mirror amplitudes are small and we may use the Lindblad operators (23)-(25). If the cavity decay rate κ is much larger than the coupling rates $g, \gamma\bar{n}$ of the mechanical oscillator, the cavity adiabatically follows the state of the mechanical oscillator, which then moves at a much slower timescale. In this situation it is possible to derive an effective equation for the mechanical oscillator by adiabatically eliminating the cavity as described in Appendix 2.B leading to Equation (90). In this framework the role of $\mathcal{L}_A$ is taken by $\mathcal{L}_c$ and the role of $\mathcal{L}_B$ is taken by $\mathcal{L}_m$.

Equation (90) applied to this optomechanical situation yields

$$\partial_t \mathcal{P}\rho(t) = L_m \mathcal{P}\rho(t) + \mathcal{P}\mathcal{L}_i(t) \int_{-\infty}^{t} dt' e^{\mathcal{Q}L_c\cdot(t-t')} \mathcal{Q}\mathcal{L}_i(t')\mathcal{P}\rho(t), \tag{26}$$

where $\mathcal{P}$ projects the cavity into the vacuum for $n_c = 0$. In leading order in g we obtain for $\rho_m = \text{Tr}_c\rho$ in the lab frame

$$\begin{aligned}\partial_t \rho_m = &- i(\omega_m + \delta\omega_+ + \delta\omega_-)\left[b^\dagger b, \rho_m\right] \\ &+ \gamma\left(1 + \bar{n}_m + \mathcal{C}_+\right)\left(\hat{b}\rho\hat{b}^\dagger - \tfrac{1}{2}\hat{b}^\dagger\hat{b}\rho - \tfrac{1}{2}\rho\hat{b}^\dagger\hat{b}\right) \\ &+ \gamma(\bar{n}_m + \mathcal{C}_-)\left(\hat{b}^\dagger\rho\hat{b} - \tfrac{1}{2}\hat{b}\hat{b}^\dagger\rho - \tfrac{1}{2}\rho\hat{b}\hat{b}^\dagger\right)\end{aligned} \tag{27}$$

where

$$\delta\omega_+ = g^2 \frac{\Delta + \omega_m}{\kappa^2/4 + (\Delta + \omega_m)^2}, \qquad \delta\omega_- = g^2 \frac{\Delta - \omega_m}{\kappa^2/4 + (\Delta - \omega_m)^2} \tag{28}$$

are frequency shifts induced by the state swap interaction (for ω_+) and the two-mode squeezing interaction (for ω_-) from Hamiltonian (25). Furthermore,

$$\mathcal{C}_+ = \frac{g^2}{\gamma} \frac{\kappa}{\kappa^2/4 + (\Delta + \omega_m)^2}, \qquad \mathcal{C}_- = \frac{g^2}{\gamma} \frac{\kappa}{\kappa^2/4 + (\Delta - \omega_m)^2} \tag{29}$$

parameterize the light induced phonon loss ($\mathcal{C}_+$, caused by the state swap interaction) and gain ($\mathcal{C}_-$, caused by the two-mode squeezing interaction) of phonons. Note that both $\omega_\pm$ and $\mathcal{C}_\pm$ have resonances at $\tilde{\Delta} = \pm\omega_m$. The ratio of the optically induced phonon transition rates and the intrinsic transition rates is given by $\mathcal{C} = |\mathcal{C}_+ + \mathcal{C}_-|$ at temperature zero) and, correspondingly, $\mathcal{C}_{\text{th}} = \mathcal{C}/(\bar{n}_m + 1)$ for finite temperature. In the sideband resolved regime ($\kappa \ll \omega_m$) and the detuning chosen at one of the resonances $\Delta = \pm\omega_m$ one can neglect $\mathcal{C}_\mp$ in comparison to $\mathcal{C}_\pm$ so that

$$\mathcal{C} = \frac{4g^2}{\gamma\kappa}, \qquad \mathcal{C}_{\text{th}} = \frac{4g^2}{\gamma\kappa(\bar{n}_m + 1)}, \tag{30}$$

which are referred to as (linearized) cooperativity and thermal (linearized) cooperativity. The corresponding single-photon cooperativities are defined by replacing the linearized coupling g by the single-photon couling g_0.

For $\kappa \gg \omega_m$ the shift of the resonance frequency $\delta\omega_m = (\delta\omega_+ + \delta\omega_-)$ caused by the optical spring effect can be approximated as $\delta\omega_m = g^2 \frac{2\tilde{\Delta}}{\kappa^2/4 + \tilde{\Delta}^2}$. In the free mass limit where $\omega_m \approx 0$ this optically mediated shift is even the dominant contribution to the spring. In the sideband resolved regime ($\kappa \ll \omega_m$) the relative shift $\delta\omega_m/\omega_m$ is very small (on the order of $g^2/\kappa\omega_m$) and can usually even be neglected for high frequency oscillators.

In any case, to discuss the optomechanical damping or anti-damping we transform Equation (27) to a Fokker-Planck equation for the mechanical oscillator's phase space distribution, as introduced in Appendix 2.A. (As an example we choose here the Glauber-Sudarshan-P distribution because the cooling dynamics is essentially classical. For the description of the nonclassical states in Chapter 3 onwards we choose to work with the Wigner distribution or the Husimi Q-distribution instead.) While there are more direct ways to discuss this, e.g. in terms of transition rates between phonon occupation states, we choose here to work with the phase space distributions, as this is the formalism in which we discuss the self-induced oscillations later. Switching for convenience to a rotating frame oscillating at $\omega_m + \delta\omega_m$, we use the translation rules for the equation of motion from Appendix 2.A (with Equation (65) applicable for the P-distribution) to obtain the equation of motion for the mechanical distribution $P_m(\beta, \beta^*)$ as

$$\begin{aligned}\partial_t P_m(\beta,\beta^*) = &\left(\partial_\beta \beta + \partial_{\beta^*}\beta^*\right)\Gamma_T P_m(\beta,\beta^*) \\ &+ 2\partial_\beta\partial_{\beta^*} D P_m(\beta,\beta^*),\end{aligned} \tag{31}$$

with damping Γ_T and diffusion D given by

$$\Gamma_T = \frac{\gamma}{2}\left(1 + \mathcal{C}_+ - \mathcal{C}_-\right), \qquad D = \frac{\gamma}{2}\left(\bar{n}_m + \mathcal{C}_-\right). \tag{32}$$

If the damping $\Gamma_T > 0$ is positive, Equation (31) can be solved for its steady state: We set the time derivative on the left side to zero and choose to work with Cartesian coordinates $\beta = x + iy$, where the equation conveniently factorizes to

$$\partial_x x \Gamma_T P_x = -\tfrac{1}{2}\partial_x^2 D P_x \tag{33}$$

and the same equation for y, with $P_m = P_x P_y$. Equation (33) is integrated to $x P_x = -\frac{1}{2}\partial_x \frac{D}{\Gamma_T} P_x$ and hence the solution for P_m is

$$P_m \propto e^{-\frac{\Gamma_T}{D}x^2} e^{-\frac{\Gamma_T}{D}y^2}. \tag{34}$$

In the case of $\Gamma_T > 0$ this can be normalized to a Gaussian (hence the state is automatically thermal) with variance $\sigma^2 = D/2\Gamma_T$ for each quadrature. With (62) we obtain for the mean number $\langle\hat{n}\rangle = \langle b^\dagger b\rangle$ of phonons

$$\langle\hat{n}\rangle = D/\Gamma_T = \frac{\bar{n}_m + \mathcal{C}_-}{1 + \mathcal{C}_+ - \mathcal{C}_-}. \tag{35}$$

However, in the case of negative damping $\Gamma_T < 0$, the system is unstable and no steady state exists in this description which relies on the linearization of the optomechanical interaction. We stress however, that due to this instability our original assumption of small mechanical amplitudes is violated and the system dynamics needs to be described taking into account the full nonlinear Hamiltonian $H - g_0 a^\dagger a\left(b + b^\dagger\right)$ from Equation (16) and the more elaborate method of adiabatic elimination presented in Section 2.B.2.

Chapter 3 is dedicated to the dynamics in this regime and the quantum steady state is derived. We will find that the damping and diffusion corresponding to Equation (32) are in fact a nonlinear function of the amplitude $r = |\beta|$ of mechanical oscillations, so that the system is driven to a limit cycle at an amplitude where the damping $\Gamma_T(r) = 0$.

Here we briefly discuss the limits of optomechanical cooling as derived in (35). The damping process is resonant at $\tilde{\Delta} = -\omega_m$ and most efficient in the sideband-resolved regime, ($\kappa \ll \omega_m$), where the resonances of $\mathcal{C}_\pm$ at $\tilde{\Delta} = \pm\omega_m$ become sharp and

$$\mathcal{C}_+ = 4\frac{g^2}{\gamma\kappa}, \qquad \mathcal{C}_- \approx \frac{1}{4}\frac{g^2}{\gamma\kappa}\frac{\kappa^2}{\omega_m^2}, \tag{36}$$

cf. Equation (30). We then approximate $\Gamma_T \approx \frac{\gamma}{2}(1+\mathcal{C}_+)$ to obtain

$$\langle \hat{n} \rangle \approx \frac{\bar{n}_m + \mathcal{C}_-}{1+\mathcal{C}_+}, \tag{37}$$

from which we can read off that a large thermal cooperativity is required to approach the quantum ground state and that the minimal achievable phonon occupation for $\mathcal{C} \to \infty$ is $\langle \hat{n} \rangle = \kappa^2/16\omega_m^2$. There is however the caveat that the cooperativity scales with the circulating intra cavity power via the linearized coupling parameter $g = g_0|\alpha|$. But the circulating intra cavity power leads to additional phonon excitations through photon absorption processes, so that one should actually consider the bath occupation number $\bar{n}_m$ as a function of the cooperativity $\mathcal{C}$ in Equation (37).

We conclude this introduction to linearized optomechanics with a discussion of the optomechanical bistability in the next section.

2.1.6 *Optomechanical Bistability*

Let us consider the classical equations of motion corresponding to the standard optomechanical master equation (14)-(16). The time evolution of $(\hat{a}, \hat{b})$ in the Heisenberg picture directly follows from (14)-(16) and by changing the operators to amplitudes (α, β) and dropping quantum noise we obtain

$$\dot{\alpha} = -(\kappa/2 - i\Delta - 2ig_0\Re(\beta))\alpha + E, \tag{38}$$
$$\dot{\beta} = -(\gamma/2 + i\omega_m)\beta + ig_0|\alpha|^2. \tag{39}$$

Solving for steady state amplitudes α_0 and β_0 where $\partial_t(\alpha, \beta) = 0$ must be fulfilled gives the same condition as (18)-(19). The shift of β_0 can be understood as the point where the constant radiation pressure force $g_0|\alpha|^2$ and the restoring force due to the mechanical spring $\omega_m|\beta_0|$ are in equilbrium. The shift of α_0 in turn is due to the shifted detuning caused the cavity length change through displacement of β_0.

Inserting (19) into (18) and squaring both sides leads to the laser input $|E|^2$ as a third order polynomial in the intra cavity photon number $n = |\alpha_0|^2$,

$$|E^2| = \left(4\frac{g_0^4}{\omega_m^2}n^2 + 4\frac{\Delta g_0^2}{\omega_m}n + \Delta^2 + \frac{\kappa^2}{4}\right)n, \tag{40}$$

where we approximated $\omega_m/(\omega^2 + \gamma^4/4) \approx 1/\omega_m$ assuming a high mechanical Q. For $\Delta > 0$ the polynomial (40) is strictly a monotonically increasing function. Hence $\Delta < 0$ is necessary for bistability. In addition the point of inflection

$$n = \frac{-4g_0^2\omega_m\Delta \pm \sqrt{4g_0^4\omega_m^2\Delta^2 - 3g_0^4\omega_m^2\kappa^2}}{12g_0^4} \tag{41}$$

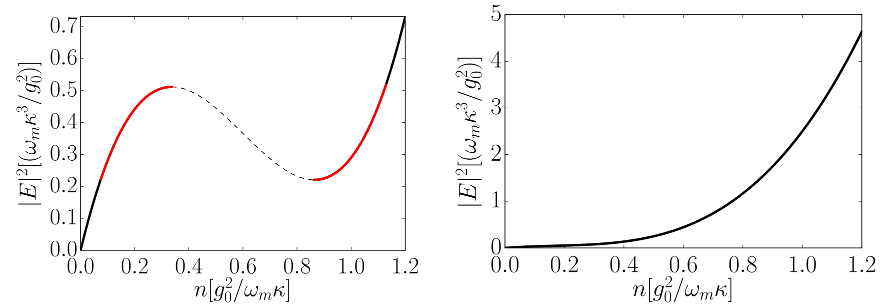

Figure 3: Laser drive E as a function of the intra cavity photon number n for parameters with (left plot, $\Delta = -1.8\kappa$) and without (right plot, $\Delta = -0.5\kappa$) bistability. The black solid line represents areas, where there exists a unique solution of Equations (18)-(19). The red solid line represents areas where two stable solutions are possible. There is then also a third solution on the dashed line lying exactly between the two points of inflection. A detailed stability analysis shows however, that this solution is not stable. Note that for convenience of the theoretical discussion we plot here E as a function of n, but it is E that can be controlled in an experiment by adjusting the laser power.

of Equation (40) must be real, requiring $4\Delta^2 > 3\kappa^2$. We conclude that the standard optomechanical system shows bistability of its intracavity amplitude if and only if

$$\Delta < -\sqrt{3/4}\kappa. \tag{42}$$

For such parameters there can be three possible solutions, out of which only two are stable, as visualized in Figure 3, showing the dependence of the laser drive E as a function of the intra cavity photon number n for parameters with and without bistability. We stress again that Equation (42) can only be fulfilled for negative detuning. Thus the static bistability is typically not relevant for the regime of self-sustained oscillations that requires $\tilde{\Delta} > 0$.

2.2 PHYSICAL REALIZATIONS

2.2.1 *Model system: Fabry-Pérot cavity coupled to end mirror*

The simplest realization of the optomechanical system described above is the optical mode of a Fabry-Pérot cavity coupled via radiation pressure force to the center of mass motion of one of its end mirrors along the cavity axis. The Fabry-Pérot cavity consists of two highly reflective mirrors facing each other. Inside the distance L between the mirrors standing light modes are resonantly trapped if their wavelength λ fulfills $n\lambda/2 = L$ for some integer n. As $\lambda = 2\pi c/\omega$ for light with speed c the cavity can support modes at frequencies

$$\omega_c = n \cdot \pi \frac{c}{L}. \tag{43}$$

As no mirror is perfectly reflective photons have a finite linewidth κ inside the cavity. The ratio of mode distance $\pi c/L$ and linewidth

$$\mathcal{F} = \pi \frac{c}{L\kappa}, \tag{44}$$

is called the finesse. For high finesse cavities it is possible to address the different resonances individually and leave out all irrelevant resonances from the description of the system. In the following we will thus focus on only one cavity mode.

In our model system one of the Fabry-Pérot cavity's end mirrors is fixed and the other mirror (mass m) is movable and attached to a spring with spring constant k. We will consider only the displacement δX of the center of mass of this mirror as the system mode with approximate (neglecting e.g. the mass of the spring) resonance frequency $\omega_m = \sqrt{k/m}$. All other modes are treated as part of the environment and their effect on the system is approximately incorporated in the Lindblad operator (8).

According to Equation (43) the cavity frequency ω_c is proportional to $(L + \delta X)^{-1}$. Expanding in a Taylor series around $\delta X = 0$ this gives

$$\omega_c = \frac{2\pi c}{\lambda} \sum_{n=0}^{\infty} \left(\frac{-\delta X}{L} \right)^n . \tag{45}$$

As the ratio $\delta X/L$ is very small we neglect all terms of higher than first order in $\delta X/L$. The only additional term in the Hamiltonian stemming from the mirror displacement then is

$$H_i = -\frac{2\pi c}{\lambda L} \hat{a}^\dagger \hat{a} \cdot \delta \hat{X}, \tag{46}$$

which has the structure of Hamiltonian (11). As the force on the mirror $\hat{F} = -\hbar \partial_{\delta \hat{X}} H_i = \hbar \frac{2\pi c}{\lambda L} \hat{a}^\dagger \hat{a}$ can be decomposed into the momentum $2\hbar k$ of $\hat{a}^\dagger \hat{a}$ photons reflected from the mirror per round trip time $T = 2L/c$ in the cavity, it is commonly referred to as the radiation pressure force.

Note that with $\delta \hat{X} = x_{\mathrm{ZPF}} \left(\hat{b} + \hat{b}^\dagger \right)$, where

$$x_{\mathrm{ZPF}} = \sqrt{\hbar / 2m\omega_m} \tag{47}$$

is the zero point fluctuation of mechanical motion, the coupling constant in (11) for the Fabry-Pérot setup is

$$g_0 = \frac{2\pi c}{\lambda L} \sqrt{\frac{\hbar}{2m\omega_m}}. \tag{48}$$

2.2.2 *Optomechanical setups*

While the Fabry-Pérot setup described above is perhaps the conceptually simplest realization of an optomechanical setup, other architectures exist with unique properties and tailored for different purposes.

We give below a brief overview based on the review article [13] with visualization in Figure 4.

a Fabry-Pérot cavity with one movable end mirror, see discussion above.

b Gravitational wave detectors [40]: The length difference of the perpendicular arms in a Michelson Interferometer is measured in the interference of their transmitted light in the signal port. Such a signal may be caused by a gravitational wave that distorts spacetime. In order to reach high sensitivity it is necessary to increase the laser power P_l to reduce the quantum shot noise scaling with $1/P_l$. In consequence, even with the massive end mirrors of these setups the optomechanical back-action on the mirror motion becomes non-negligible resulting in back-action noise (scaling with P_l) that disturbs the signal. The best signal is reached at the standard quantum limit, where back action noise and shot noise are of the same size.

c Optical Microresonators [41]: Light travels in a whispering gallery mode that couples e.g. to the breathing mode of the mechanical object. Due to the small size of the resonators high coupling rates are achieved in these setups. Addressable mechanical frequencies range from a few MHz to the GHz regime.

d Optomechanical crystals [42]: The optical modes of optical crystals can be coupled to highly localized mechanical modes of the crystal. These nanofabricated devices are considered a very promising candidate to reach the single-photon strong-coupling regime, where g_0 becomes comparable to the cavity decay rate κ and quantum effects are observable on the level of single quanta.

e Levitated objects [43, 44]: Freeing the mechanical resonator from a mounting drastically reduces its coupling to the environment and thereby also decoherence. It has been proposed to use e.g. optically levitated nanospheres to test modifications of standard quantum mechanics such as the Penrose interpretation or Ghirardi-Rimini-Weber theory, which both propose additional decoherence processes, due to an objective collapse of the wave function that would scale with the mass of the oscillator. Also a cloud of cold atoms can be used as the mechanical oscillator. Such setups can get very close to the single-photon strong-coupling regime due to the tiny mass of the oscillator.

f Microwave resonators [45]: Mechanical motion can also be coupled to radiation on scale of microwaves. Typical architectures consist of a several micrometer sized membrane (resonance frequency around 10 MHz) capacitively coupled to an LC circuit.

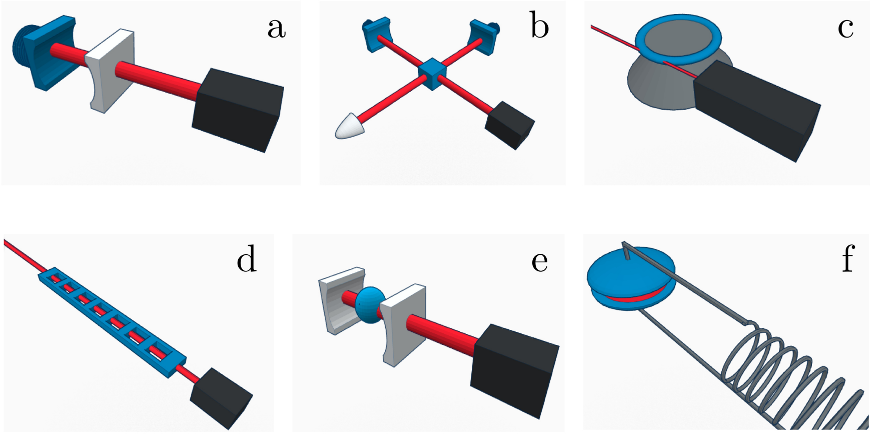

Figure 4: Schematic drawings of common optomechanical systems: Optical or microwave modes (red) couple to the motion of mechanical objects (blue). As described above, the systems are respectively: a) Fabry-Pérot cavity with movable end mirror. b) Gravitational wave detector. c) Toroid shaped optical microresonator. d) Optomechanical Crystal e) Levitated object. f) Microwave resonator.

Such setups hold the record for the highest cooperativity, which is the ratio of optically induced mechanical damping to intrinsic mechanical damping.

So far we have only considered coupling of a mechanical oscillator to an optical mode. Stretching a bit the definition of optical, mechanical oscillators can also form optomechanical systems with e.g. nitrogen-vacancy centers [46], superconducting qubits [9] or the internal level structure of atoms [35, 36]. While the Lindblad equation for these systems is not necessarily identical to the standard optomechanical setup, phenomena such as sideband cooling or heating can be understood in close analogy and have been experimentally realized first in these setups.

In particular a focus of this thesis lies also on optomechanics with trapped ions [35, 36], where the ions' oscillations inside the trap are coupled to their internal energy structure via radiative forces. The Lindblad equation for such a setup is introduced in the next section.

2.2.3 *Trapped ions*

A typical ion trap (Paul Trap) consists of two electrodes that create a static potential for the ion along the z-axis. While no static electromagnetic potential exists that could create a stable stationary equilibrium in three dimensions, it is possible to trap the ions simultaneously along the x and y axis also, using a time dependent field that oscillates at a radio frequency along these directions. Effectively this can be described as a static harmonic potential for the ions. We assume

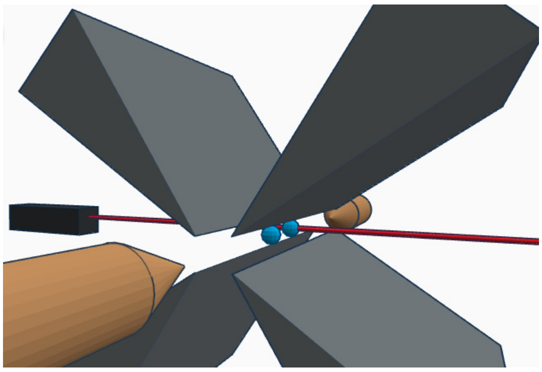

Figure 5: Schematic picture of an ion trap with two trapped ions (blue). A transition of one ion is driven here by a laser, establishing the coupling between its internal levels and the ion crystal's motion via photon recoil.

here that the trapping along the x- and y- direction is so tight that we need to consider only the oscillations along the z-axis. Also we consider here only one ion to introduce the Lindblad operator

$$\mathcal{L}_m \rho = -i \left[\nu b^\dagger b, \rho \right] , \tag{49}$$

describing the motion of the ions. More complex setups with many ions can be mapped onto this simple model. We will address the description of such a multi ion setup in Section 7.4.1.

Note that Equation (49) is the same as Equation (15), but neglecting dissipation. In the context of ions the mechanical resonance frequency ω_m is usually referred to as ν and we adopt this convention here as well. We keep the notation for the destruction operator of a motional excitation as b. While an ion has many internal levels, we use here the approximation of a two level ion described by the Lindblad operator

$$\mathcal{L}_A \rho = -i \left[\frac{\omega_A}{2} \sigma_z, \rho \right] + \Gamma \left(\sigma_- \rho \sigma_+ - \tfrac{1}{2} \sigma_+ \sigma_- \rho - \tfrac{1}{2} \rho \sigma_+ \sigma_- \right) , \tag{50}$$

where ω_A is the transition's frequency and Γ its linewidth. The interaction of the internal ion state to its motion can be turned on with an external laser that drives e.g. a dipole transition between the two levels, leading to an interaction Hamiltonian of the form

$$H_I = \frac{\Omega}{2} \sigma_- \exp \left(i \omega_l t - i \eta (b + b^\dagger) \right) + \text{h.c.} \tag{51}$$

The parameter η is referred to as the Lamb-Dicke parameter and given by $\eta = k X_{\text{ZPF}}$ where k is the lasers wave number in z-direction and $X_{\text{ZPF}} = \sqrt{\hbar / 2 \nu M}$ is the position's zero point fluctuation for an

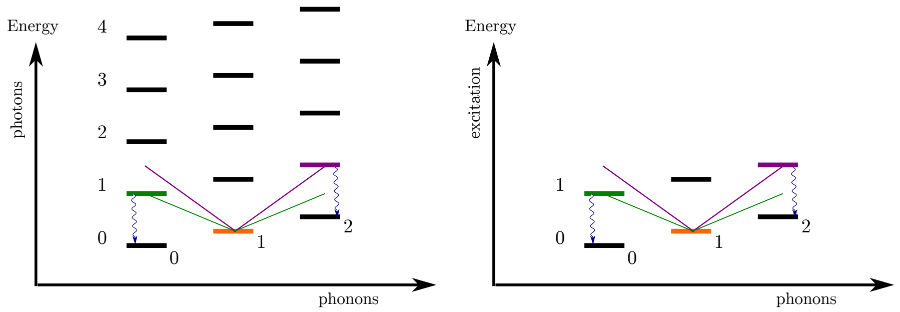

(a) Level scheme for mechanical oscillator coupled to an optical cavity.

(b) Level scheme for mechanical oscillator coupled to the intrinsic state of an ion.

Figure 6: Comparison of optomechanical cooling for a system of an optical cavity coupled to a mechanical oscillator (a), and for a trapped ion (b).

ion of mass M. In a rotating frame for the internal level at the laser frequency ω_l the full set of Lindblad operators is

$$\mathcal{L}_m\rho = -i\left[\nu b^\dagger b, \rho\right], \tag{52}$$

$$\mathcal{L}_A\rho = -i\left[-\frac{\Delta}{2}\sigma_z, \rho\right] + \Gamma\left(\sigma_-\rho\sigma_+ - \tfrac{1}{2}\sigma_+\sigma_-\rho - \tfrac{1}{2}\rho\sigma_+\sigma_-\right), \tag{53}$$

$$\mathcal{L}_i\rho = -i\left[\frac{\Omega}{2}\sigma_- \exp\left(-i\eta(b+b^\dagger)\right) + \text{h.c.}, \rho\right] \tag{54}$$

with $\Delta = \omega_L - \omega_a$.

We note that in many setups X_{ZPF} is small on the scale of the laser's wavelength, allowing for an approximation of Equation (51) to first order in the Lamb-Dicke parameter for small oscillation amplitudes. This Hamiltonian then is very similar to the linearized version of the optomechanical interaction between an oscillator and a cavity given by Equations (20)-(22), where the cavity degree of freedom is replaced by the internal degree of freedom of the ion:

At a detuning $\Delta = -\nu$ the resonant term of the interaction is proportional to $\sigma_+ b + \sigma_- b^\dagger$ and for $\Delta = +\nu$ the resonant term of the interaction is proportional to $\sigma_+ b^\dagger + \sigma_- b$. Viewing σ_- and σ_+ as the qubit analogue of the destruction operator a and the construction operator $a^\dagger$, this is similar to the state-swap and two-mode squeezing interaction discussed in the oscillator-cavity coupling above, if the cavity is truncated only on its lowest two excitation states around the shifted vacuum. The truncation is indeed a good approximation and the two systems can be understood in analogy, as visualized in Figure 6, if the following two conditions are fulfilled: First, the mechanical oscillations have to be small enough to ensure the applicability of the linearized interaction. Second, the atomic transition decay rate Γ has to be much faster than $\eta\Omega$ for a trapped ion, respectively the cavity decay rate κ has to be much faster than the linearized coupling g, so that both the cavity and internal state approximately occupy only the lowest two levels.

2.3 OUTLINE OF THE FOLLOWING CONTRIBUTIONS

In this first chapter, we introduced the basic concepts and methods for quantum optomechanics that are needed for the following chapters, where our new contributions to the field are presented. To provide the context to these contributions, this last introductory section gives a brief overview on the respective experiments considered and the questions we will address.

2.3.1 *Self-sustained optomechanical oscillations*

For the analytical description of optomechanical self-sustained oscillations [22, 23, 24, 25, 26, 27, 28, 29, 30] in the quantum regime, we develop in Chapter 3 a formalism based on the projection operator method from Appendix 2.B.2, which allows to eliminate the cavity with a different reference state for each point of the oscillator in phase space. This flexibility of the reference state is necessary as an excited mechanical oscillator is spread out in phase space, in contrast to the situation of optomechanical cooling, where the oscillator is approximately in its ground state and it is sufficient to use one reference state for the cavity. In Chapter 4 we then use the formalism to derive conditions on the system parameters to generate a steady state with non-classical phonon statistics for the standard optomechanical system (coupling one cavity mode to a mechanical oscillator). In Chapter 5 we show that an optomechanical system with two cavity modes can significantly ease these conditions: By supporting both carrier and sideband photons, the phonon excitation process becomes resonant. In both setups the phonon statistics can be mapped out via a Hanburry-Brown-Twiss measurement on the sideband-photons emitted from the optomechanical cavity, as was experimentally demonstrated in [30].

2.3.2 *Ion spectroscopy*

In Chapter 6 we turn to the theoretical description of a spectroscopy experiment [3] with trapped ions, which demonstrated a new method to measure an ion's internal level structure via the recoil of the photons on the ion. This recoil excites the center of mass motion of the spectroscopy ion and a co-trapped logic ion of a different, well-controlled species. The motional excitation finally is transferred onto the internal state of the logic ion, where it can be measured with extremely high efficiency. [2] The scheme [3] is an extension of quantum logic spectroscopy [47] to a wider class of objects, allowing spectroscopy also on transitions of ions (or molecules) with a short lifetime. When measuring the resonance with the effective two point sampling method, a systematic shift occurs. It is analyzed within the framework from Section 2.B.2, adiabatically eliminating the internal state of the ions with a reference state depending on the Doppler shift caused by the ions' momentum in phase space.

2.3.3 *Ion clocks*

Chapter 7 is concerned with optical clocks in the context of trapped ions. Such clocks provide record frequency accuracy and a good short-term stability. For most ion species suitable to build an optical clock a direct readout is not possible due to their lack of a transition allowing for laser cooling and state detection. In analogy to the quantum logic spectroscopy experiment described above, one can indirectly read out their state via co-trapped logic ions with an appropriate transition. Optical clocks based on a single ion employing such indirect readout have been built [48, 49] and clocks with multiple ions are soon to come. We present and analyze an efficient scheme for a setup with *multiple* clock ions, which is based on the quantum algorithm to read out the Hamming weight.

---

[2] The logic ion is chosen from a species where this is possible.

APPENDIX TO CHAPTER 2: ANALYTICAL AND NUMERICAL METHODS FOR QUANTUM OPTICS IN PHASE SPACE

In this appendix we introduce a number of methods for the description of quantum optical systems, which we apply in the following chapters to the optomechanical setups studied in this thesis.

2.A PHASE SPACE DISTRIBUTIONS

The state of a bosonic mode can be represented not only as a density matrix, but also in terms of a phase space distribution in the oscillator's complex amplitude α. The most prominent distributions are the Glauber-Sudarshan P-distribution, the Wigner-distribution (W) and the Husimi Q-distribution. As we will use these three representations for some of the calculations in this thesis, we give an overview below.

2.A.1 *Definition*

We define the phase space distributions via the (normally ordered, anti-normally ordered and symmetrically ordered) quantum characteristic functions

$$\chi_N(\lambda,\lambda^*) = \mathrm{Tr}\left(\hat{\rho}\exp(\lambda\hat{a}^\dagger)\exp(-\lambda^*\hat{a})\right), \tag{55}$$

$$\chi_A(\lambda,\lambda^*) = \mathrm{Tr}\left(\hat{\rho}\exp(-\lambda^*\hat{a})\exp(\lambda\hat{a}^\dagger)\right), \tag{56}$$

$$\chi_S(\lambda,\lambda^*) = \mathrm{Tr}\left(\hat{\rho}\exp(\lambda\hat{a}^\dagger-\lambda^*\hat{a})\right), \tag{57}$$

where the ordering is with respect to the operators $\hat{a}^\dagger$ and $\hat{a}$ and the indices N, A and S indicate the ordering of the used displacement operator

$$\hat{D}(\lambda) = \exp\left(\lambda\hat{a}^\dagger - \lambda^*\hat{a}\right). \tag{58}$$

In analogy to the characteristic function in classical statistics, the derivative of the quantum characteristic functions evaluated at the origin gives the expectation values of the moments. However, as $\hat{a}$ and $\hat{a}^\dagger$ don't commute, it is necessary to specify the ordering in the quantum case, as we did above. Again in analogy to classical statistics the quasi probability distributions can be defined as the Fourier transformation of the characteristic functions, i.e.

$$P(\alpha,\alpha^*) = \frac{1}{\pi^2}\int \mathrm{d}^2\lambda \exp\left(\alpha\lambda^* - \alpha^*\lambda\right)\chi_N(\lambda,\lambda^*), \tag{59}$$

$$Q(\alpha,\alpha^*) = \frac{1}{\pi^2}\int \mathrm{d}^2\lambda \exp\left(\alpha\lambda^* - \alpha^*\lambda\right)\chi_A(\lambda,\lambda^*), \tag{60}$$

$$W(\alpha,\alpha^*) = \frac{1}{\pi^2}\int \mathrm{d}^2\lambda \exp\left(\alpha\lambda^* - \alpha^*\lambda\right)\chi_S(\lambda,\lambda^*), \tag{61}$$

where P, Q and W correspond to normal, anti-normal and symmetrical ordering.

2.A.2 *Calculation of moments*

The normally ordered, anti-normally ordered and symmetrically ordered moments of $\hat{a}^\dagger$ and $\hat{a}$ are obtained from the phase space distributions as

$$\langle \hat{a}^{\dagger m}\hat{a}^n\rangle = \int d^2\alpha P(\alpha,\alpha^*)\alpha^{*m}\alpha^n \tag{62}$$

$$\langle \hat{a}^m\hat{a}^{\dagger n}\rangle = \int d^2\alpha Q(\alpha,\alpha^*)\alpha^m\alpha^{*n} \tag{63}$$

$$\langle S\left(\hat{a}^m,\hat{a}^{\dagger n}\right)\rangle = \int d^2\alpha W(\alpha,\alpha^*)\alpha^m\alpha^{*n}, \tag{64}$$

where $S\left(\hat{a}^m,\hat{a}^{\dagger n}\right)$ stands for the symmetric ordering of the operators, where the average over all possible orderings is taken. Note that the relations (62)-(64) can be used e.g. to calculate the mean values $\langle n\rangle = \langle \hat{a}^\dagger\hat{a}\rangle$ and $\langle n^2\rangle = \langle(\hat{a}^\dagger\hat{a})^2\rangle$.

2.A.3 *Equations of motion*

The time derivative of the phase space distributions can be obtained from the master equation via the following translation rules and their adjoints for the

- Glauber-Sudarshan P-distribution:

$$\hat{a}\rho \rightarrow \alpha P, \qquad \hat{a}^\dagger\rho \rightarrow \left(\alpha^* - \frac{\partial}{\partial\alpha}\right)P. \tag{65}$$

- Husimi Q-distribution:

$$\hat{a}\rho \rightarrow \left(\alpha + \frac{\partial}{\partial\alpha^*}\right)Q, \qquad \hat{a}^\dagger\rho \rightarrow \alpha^* Q. \tag{66}$$

- Wigner distribution:

$$\hat{a}\rho \rightarrow \left(\alpha + \frac{1}{2}\frac{\partial}{\partial\alpha^*}\right)W, \qquad \hat{a}^\dagger\rho \rightarrow \left(\alpha^* - \frac{1}{2}\frac{\partial}{\partial\alpha}\right)W. \tag{67}$$

The translation rules can be verified using Equations (55)-(57), as well as Equations (59)-(61) and applying the cyclicity of the trace, the Baker-Campbell-Hausdorff formula and partial integration.

2.A.4 *Basic properties*

- The P-distribution of a density operator $\hat{\rho}$ fulfills

  $$\hat{\rho} = \int d^2\alpha P(\alpha)|\alpha\rangle\langle\alpha|. \tag{68}$$

  While unique, P is not always an ordinary, well-behaved function, but can sometimes only be defined in the more general framework of (sufficiently singular) distributions. As one can immediately read off from the definition, a coherent state's P-distribution is given by a Dirac delta distribution $\delta(\alpha - \alpha_0)$. Thus, roughly speaking, anything more thermal than a coherent state can be obtained by a convolution of a positive continuous function with a Dirac delta distribution, which is again a positive continuous function. On the other hand, states with less uncertainty than a coherent state in a quadrature (e.g. Gaussian squeezed states) or energy (e.g. number squeezed states) will have a highly singular P-distribution. In the context of optics, where the measurement statistics of photons is derived from the normal ordered operators described by the P-distribution, a singular P-function indicates a nonclassical state of light.

- The Wigner distribution for density matrices was historically first defined in position and momentum as

  $$W(x,p) = \frac{1}{\pi\hbar}\int_{-\infty}^{\infty} \mathrm{d}y e^{-2ipy/\hbar}\langle x+y|\rho|x-y\rangle, \tag{69}$$

  which is equivalent to (61). It exists for any ρ and is positive for any Gaussian state. According to Hudson's theorem [50] for any non-Gaussian pure state it will have some negative area. An extension to mixed states was given in [51]. Recently it was shown [52] that negative Wigner density can be understood as a resource in quantum computing in the sense that quantum circuits exhibiting only positive Wigner distributions can be efficiently simulated classically. The Wigner function is the quantum analogue of the classical Liouville phase space probability density, which is always positive. Thus, negativity of the Wigner function is often used to as an indicator of quantum mechanical interference.

  A useful property of the Wigner function is that the marginal distributions of the quadratures give their (positive) probability densities

  $$\int_{-\infty}^{\infty} dp\, W(x,p) = \langle x|\rho|x\rangle \tag{70}$$

  $$\int_{-\infty}^{\infty} dx\, W(x,p) = \langle p|\rho|p\rangle. \tag{71}$$

- The Husimi Q-function may alternatively be defined as

  $$Q(\alpha,\alpha^*) = \frac{1}{\pi}\langle\alpha|\rho|\alpha\rangle \tag{72}$$

  and, being always a positive continuous function, it is the most regular of all phase space distribution. This is also reflected in the relations

  $$W(\alpha,\alpha^*) = \frac{2}{\pi}\int_{-\infty}^{\infty} d\beta^2\, P(\beta,\beta^*)\exp(-2|\alpha-\beta|^2), \tag{73}$$
  $$Q(\alpha,\alpha^*) = \frac{1}{\pi}\int_{-\infty}^{\infty} d\beta^2\, P(\beta,\beta^*)\exp(-|\alpha-\beta|^2), \tag{74}$$

  which means that both Q and W are obtained from P via convolution with a Gaussian that smoothes out irregularities. For the Q function the Gaussian's variance is largest, making even areas of negative density become positive.

- More generally it is possible to define for $s \in [-1,1]$ an s-parameterized characteristic function

  $$\chi_s(\alpha,\alpha^*) = \exp\left(\tfrac{1}{2}s|\alpha|^2\right)\mathrm{Tr}\left(\hat{\rho}\hat{D}(\alpha)\right) \tag{75}$$

  and corresponding s-parameterized phase space distribution

  $$P_s(\alpha,\alpha^*) = \frac{1}{\pi^2}\int \mathrm{d}^2\lambda\,\exp\left(\alpha\lambda^* - \alpha^*\lambda\right)\chi_s(\lambda,\lambda^*), \tag{76}$$

  obtained again via Fourier transformation. The translation rules for the equation of motion of an s-parameterized distribution are

  $$b\rho \to (\beta + \tfrac{1-s}{2}\partial_{\beta^*})P_s, \qquad b^\dagger\rho \to (\beta^* - \tfrac{1+s}{2}\partial_\beta)P_s. \tag{77}$$

  Choosing s at $1, 0, -1$ corresponds to respectively normal, symmetric and anti-normal operator ordering so that the phase space distributions introduced above correspond to $P_1 = P$, $P_0 = W$ and $P_{-1} = Q$.

2.B ADIABATIC ELIMINATION

For dynamical systems where one process happens on a much faster timescale than all other processes it can be possible to adiabatically eliminate the fast process and retain an effective description of the system on the slower timescales only. We review here a text book approach found e.g. in [53, 54] for the situation where one subsystem of a composite quantum system decays so fast that it can be adiabatically eliminated. Particularly, the approach is applicable for the following commonly encountered situation: Two subsystems A and

B with independent environments are coupled to each other. If system A is driven (by interaction with its environment) into a particular steady state at a decay rate exceeding all other relevant timescales (in particular the independent time evolution of subsystem B and the interaction between the subsystems), it is possible to adiabatically eliminate system A and derive an approximate equation of motion for system B.

Formally, assuming Markovian interaction with the environment, we describe this situation by a master equation of the form

$$\dot{\rho} = \mathcal{L}\rho, \qquad \mathcal{L} = \mathcal{L}_i + \mathcal{L}_A + \mathcal{L}_B \tag{78}$$

with operators for interaction ($\mathcal{L}_i$), system A ($\mathcal{L}_A$) and system B ($\mathcal{L}_B$). The adiabatic elimination is a good approximation if $\mathcal{L} \approx \mathcal{L}_A$ in a sense we will explain below, after the necessary framework is introduced.

2.B.1 *Introduction to the projection operator method*

The adiabatic elimination can be done with various formalisms. Here we introduce a projection operator method resembling the Nakajima-Zwanzig formalism [3] in the notation of [54], which can be applied on the level of master equations. We assume that $\mathcal{L}_A$ is time independent and has a unique steady state σ_{ss} (fulfilling $\mathcal{L}_A\sigma_{\mathrm{ss}} = 0$) in system A to define the projector $\mathcal{P}$ as

$$\mathcal{P}\rho = \lim_{t\to\infty} e^{\mathcal{L}_A t}\rho. \tag{79}$$

From this definition follows the property

$$\mathcal{P}\rho = \sigma_{\mathrm{ss}} \otimes \mathrm{Tr}_A\left(\rho\right), \tag{80}$$

where Tr_A is the partial trace over system A. As system A is assumed to be almost completely in its steady state, $\mathcal{P}$ is called the projector on the relevant part of the system. We also define the complementary projector $\mathcal{Q} = 1 - \mathcal{P}$ on the complementary, irrelevant part of the system. Inserting the identity as $1 = \mathcal{P} + \mathcal{Q}$ we can now write the equation of motion for both subspaces as

$$\partial_t\mathcal{P}\rho = \mathcal{P}\mathcal{L}(\mathcal{P} + \mathcal{Q})\rho \tag{81}$$

$$\partial_t\mathcal{Q}\rho = \mathcal{Q}\mathcal{L}(\mathcal{P} + \mathcal{Q})\rho. \tag{82}$$

Equation (82) is a standard linear differential equation for $\mathcal{Q}\rho$ with linear operator $\mathcal{Q}\mathcal{L}$ and inhomogeneity $\mathcal{Q}\mathcal{L}\mathcal{P}\rho$. Defining the propagator $\mathcal{G}(t, t_0)$ as the solution of

$$\partial_t\mathcal{G}(t, t_0) = \mathcal{Q}\mathcal{L}(t)\mathcal{G}(t, t_0) \tag{83}$$

$$\mathcal{G}(t_0, t_0) = 1 \tag{84}$$

---

[3] The Nakajima-Zwanzig formalism is tailored to study non-Markovian dynamics. We will use it as our general framework, but finally derive a Markovian equation.

Equation (82) can be solved as

$$\mathcal{Q}\rho(t) = \mathcal{G}(t, t_0)\mathcal{Q}\rho(t_0) + \int_{t_0}^{t} dt' \mathcal{G}(t, t')\mathcal{Q}\mathcal{L}(t')\mathcal{P}\rho(t').$$

for arbitrary initial state $\rho(t_0)$ at initial time t_0. The first expression $\mathcal{G}(t, t_0)\mathcal{Q}\rho(t_0)$ can be dropped if (at least) one of the following two conditions is met:

- The system is initialized such that $\mathcal{Q}\rho(t_0) = 0$.
- $t - t_0$ is large on the decay time of $\mathcal{G}(t, t_0)$, which we may assume e.g. when calculating a steady state. As all eigenvalues of $\mathcal{Q}\mathcal{L}$ restricted on the $\mathcal{Q}$-subspace have negative real part, it follows that $\lim_{t\to\infty} \mathcal{G}(t, t_0)\mathcal{Q} = 0$.

As one of these conditions is always fulfilled in this thesis, we insert only the second term of Equation (85) into (81) to obtain for the relevant subspace

$$\partial_t \mathcal{P}\rho(t) = \mathcal{P}\mathcal{L}(t)\mathcal{P}\rho(t) + \mathcal{P}\mathcal{L}(t) \int_{t_0}^{t} dt' \mathcal{G}(t, t')\mathcal{Q}\mathcal{L}(t')\mathcal{P}\rho(t'). \tag{85}$$

While still exact, this equation is in general just as hard to solve as the original master equation, due to the appearance of $\rho(t')$ and $\mathcal{G}(t, t')$ in the integral. Thus we make two approximations at this point:

- All eigenvalues of $\mathcal{Q}\mathcal{L}_A\mathcal{Q}$ automatically have negative real part by construction. The real part of the eigenvalue with least negative real part shall be denoted as $-\kappa$, making κ a decay rate. We denote $G = \max_\rho \|\mathcal{Q}\mathcal{L}_i\mathcal{Q}\rho\|, \gamma = \max_\rho \|\mathcal{Q}\mathcal{L}_B\mathcal{Q}\rho\|$ for all density matrices ρ encountered during the time evolution. [4] If $\kappa \gg G, \gamma$, we can make the approximation

  $$\mathcal{G}(t, t')\mathcal{Q} \approx e^{\mathcal{Q}\mathcal{L}_A \cdot (t-t')}\mathcal{Q} \tag{86}$$

  with a relative error of at most $(G + \gamma)/\kappa$. If only $\kappa \gg G$ is fulfilled, it is possible to make the analogous weaker approximation $\mathcal{G}(t, t')\mathcal{Q} \approx e^{\mathcal{Q}(\mathcal{L}_A+\mathcal{L}_B)\cdot(t-t')}\mathcal{Q}$, but here we assume the stronger condition $\kappa \gg G, \gamma$ for simplicity.
- We anticipate here that $\|\mathcal{P}\rho(t') - \mathcal{P}\rho(t)\|$ will turn out to be smaller than $(\gamma + \frac{G^2}{\kappa})(t - t')$, justifying the approximation

  $$\mathcal{P}\rho(t') \approx \mathcal{P}\rho(t), \tag{87}$$

  as the integration kernel decays at a rate faster than κ. The relative error of this approximation is smaller than $(\gamma/\kappa + G^2/\kappa^2)$.

---

[4] $\mathcal{L}_i$ and $\mathcal{L}_B$ can be unbounded on the whole Hilbert space, but often ρ can nevertheless be considered on a subspace where $\mathcal{L}_i$ and $\mathcal{L}_B$ are bounded, e.g. if the system's energy is bounded.

With these approximations we get the expression

$$\partial_t \mathcal{P}\rho(t) = \mathcal{P}\mathcal{L}(t)\mathcal{P}\rho(t) + \mathcal{P}\mathcal{L}(t) \int_{t_0}^{t} dt' e^{\mathcal{Q}\mathcal{L}_A \cdot (t-t')} \mathcal{Q}\mathcal{L}(t')\mathcal{P}\rho(t), \tag{88}$$

where the $\mathcal{L}$ operators can be simplified using the following properties:

- $\mathcal{L}_A\mathcal{P} = 0$ because $\mathcal{L}_A\sigma_{\text{ss}} = 0$.
- $\mathcal{P}\mathcal{L}_A = 0$ as $\mathcal{L}_A$ must preserve the trace on subsystem A.
- $\mathcal{Q}\mathcal{L}_B\mathcal{P} = \mathcal{P}\mathcal{L}_B\mathcal{Q} = 0$ as all three operators commute and $\mathcal{P}\mathcal{Q} = 0$.
- We demand that $\mathcal{P}\mathcal{L}_i\mathcal{P} = 0$. If this is not the case $\mathcal{L}_i$ should be redefined (before starting the calculation) by shifting the nonzero term to $\mathcal{L}_B$. Formally: Define the operator $\mathcal{L}_{I,B}$ acting only on system B as $\mathcal{L}_{I,B}\rho_B = \text{Tr}_A\left(\mathcal{L}_i\rho_B \otimes \sigma_{\text{SS}}\right)$ and change

  $$\mathcal{L}_i \to \mathcal{L}_i - \mathcal{L}_{I,B}, \qquad \mathcal{L}_B \to \mathcal{L}_B + \mathcal{L}_{I,B}. \tag{89}$$

  Note that this redefinition decreases G (possibly at the cost of increasing γ) and thereby helps to fulfill $G \ll \kappa$.

Our final result is

$$\partial_t \mathcal{P}\rho(t) = \mathcal{P}\mathcal{L}_B(t)\mathcal{P}\rho(t) + \mathcal{P}\mathcal{L}_i(t) \int_{t_0}^{t} dt' e^{\mathcal{Q}\mathcal{L}_A \cdot (t-t')} \mathcal{Q}\mathcal{L}_i(t')\mathcal{P}\rho(t), \tag{90}$$

where $t_0 \approx -\infty$ is applicable for large times $t \gg 1/\kappa$.

2.B.2 *Adiabatic Elimination in phase space*

In the previous Section 2.B.1 we assumed that $\mathcal{L}_A$ has a unique steady state into which system A decays at a rate much faster than the interaction with system B can drive it somewhere else. In this section we introduce a more versatile method of adiabatic elimination that can be applied even if this condition is not fulfilled. It is tailored for setups where system B is a bosonic mode and the interaction is such that system A is driven into a different steady state depending on the amplitude β of the mode. It was first developed [31] to theoretically describe a laser cavity pumped by atoms, where the atoms decay into a different steady state depending on the amplitude of the cavity amplitude.

Formally we again start from a master equation of the form

$$\dot{\rho} = \mathcal{L}\rho, \qquad \mathcal{L} = \mathcal{L}_i + \mathcal{L}_A + \mathcal{L}_B \tag{91}$$

with operators for interaction ($\mathcal{L}_i$), system A ($\mathcal{L}_A$) and system B ($\mathcal{L}_B$). Remember that one condition for the applicability of the standard adiabatic elimination was that $\kappa \gg G, \gamma$, with κ and G defined just above Equation (86). We stress that the definition of $G = \max_\rho \|\mathcal{Q}\mathcal{L}_i\mathcal{Q}\rho\|$ depends on the possible density matrices considered. If highly excited states of system B (encountered e.g. if system B undergoes self-induced oscillations, cf. end of Section 2.1.5) must be taken into account, G may grow too large.

This problem can often be solved by switching to one of the phase space distributions defined in Section 2.A for system B. The state of the system is then described by an object $\sigma(\beta, \beta^*)$, which is a density matrix for system A at each point of phase space β of system B. (Note that nonlinear dependence of σ on β is possible and thus the method presented here allows for the accurate description of nonlinear interaction.) Tracing out system A then yields the phase space distribution for system B

$$P(\beta, \beta^*) = \mathrm{Tr}\sigma(\beta, \beta^*), \tag{92}$$

if we choose e.g. to work with the P-distribution. The equation of motion for $\sigma(\beta, \beta^*)$ is obtained from the master equation for ρ using the translation rules (65).

We now decompose $\mathcal{L}_i$ into

$$\mathcal{L}_i = \mathcal{L}_{I,A} + \mathcal{L}_{I,I}, \tag{93}$$

such that no derivatives ∂_β or ∂_{β^*} appear in $\mathcal{L}_{I,A}\sigma(\beta, \beta^*)$, i.e. only operators acting on system A multiplied by functions of β and β^* appear and hence $\mathcal{L}_{I,A}$ affects only system A but not system B. This decomposition is used to regroup the original operators into

$$\tilde{\mathcal{L}}_I = \mathcal{L}_i - \mathcal{L}_{I,A} = \mathcal{L}_{I,I}, \tag{94}$$

$$\tilde{\mathcal{L}}_A = \mathcal{L}_A + \mathcal{L}_{I,A}, \tag{95}$$

$$\tilde{\mathcal{L}}_B = \mathcal{L}_B. \tag{96}$$

Only if a decomposition can be found where $\tilde{G} = \max_\rho \|\tilde{\mathcal{L}}_I\rho\|$ is small on the timescale of κ, the adiabatic elimination procedure gives a good approximation. As the terms from $\mathcal{L}_I$ of leading order in $|\beta|$, i.e. the largest terms, can be put into $\mathcal{L}_{I,A}$, this is often possible. Other standard manipulations such as rotating or shifted reference frames may of course also be employed to reach the goal $\tilde{G} \ll \kappa$. Once this is achieved the remaining procedure is analogous to Section 2.B.1, but with the following differences:

- The steady state $\sigma_{\mathrm{SS}}(\beta, \beta^*)$ of $\tilde{\mathcal{L}}_A$ in system A may now depend on β. The new projector on the relevant subspace is again defined via

$$\tilde{\mathcal{P}}\rho = \lim_{t\to\infty} e^{\tilde{\mathcal{L}}_A t}\rho, \tag{97}$$

which now has the property

$$\tilde{\mathcal{P}}\sigma(\beta,\beta^*) = \sigma_{\text{ss}}(\beta,\beta^*)\text{Tr}_A\left(\sigma(\beta,\beta^*)\right), \qquad (98)$$

the β-dependent analogue to Equation (80).

- A redefinition of the operators analogous to (89), now with $\mathcal{L}_{I,B}P(\beta,\beta^*) = Tr_A\left(\tilde{\mathcal{L}}_I P(\beta,\beta^*)\sigma_{SS}(\beta,\beta^*)\right)$ may further decrease $\tilde{g}$.
- Note that, in contrast to Section 2.B.1, $\tilde{\mathcal{L}}_B$ does not necessarily commute with $\tilde{\mathcal{L}}_A$, $\tilde{\mathcal{P}}$ and $\tilde{\mathcal{Q}}$. Thus one must in general take the commutators into account.

Under some circumstances, e.g. if $\gamma \ll \kappa$, one can however neglect the commutators and derive

$$\begin{aligned}\partial_t P(\beta,\beta^*,t) &\approx \tilde{\mathcal{L}}_B P(\beta,\beta^*,t)\\ &+ \text{Tr}_A\left(\tilde{\mathcal{L}}_I(t)\int\limits_{t_0}^{t} dt' e^{\tilde{\mathcal{L}}_A\cdot(t-t')}\tilde{\mathcal{L}}_I(t')\sigma_{SS}(\beta,\beta^*)(t)\right)P(\beta,\beta^*,t), \qquad (99)\end{aligned}$$

which is the analogon of Equation (90).

The adiabatic elimination method presented in this section allows for very flexible transformations of the system's equation of motion. We fully develop this formalism in the optomechanical context in Chapter 3. It is then used to analyze self-induced oscillations in the standard optomechanical setup in Chapter 4. For the description of a trapped ion system in Chapter 6, a very similar transformation allows for the treatment of a systematic Doppler shift in the context of a high precision spectroscopy experiment [3].

2.C NUMERICAL ANALYSIS

In this section we give a brief overview on the most common numerical methods for the study open quantum systems. For small to moderate system size it is possible to use standard methods on the level of density matrices, e.g. for the time evolution one can numerically integrate the master equation with a standard Runge-Kutta scheme; to find steady state solutions, standard linear algebra solvers such as the biconjugate gradient method can be used.

For increasingly large Hilbert space dimensions it can be more efficient to operate on the level of wave functions, scaling linearly with the number of states, instead of density matrices, which scale quadratically. This is possible using the quantum trajectories method for the time evolution, where pure quantum states follow a stochastic equation of motion. The price to pay for the improved scaling with dimensionality is that many independent trajectories have to be run and finally averaged to compose the density matrix out of the wave functions. The method is described in the following Section 2.C.1.

An even more efficient method is to describe the system dynamics in terms of Langevin equations in phase space. The Langevin method is however only applicable to a more narrow set of problems as we describe in Section 2.C.2.

Both stochastic methods allow for parallelization of the computation e.g. on a computer cluster or graphic cards. Most numerical calculations in this thesis were performed using QuTiP, a Toolbox for Quantum Mechanics based mostly on the Python libraries SciPy and NumPy, which provides many useful tools such as a quantum trajectories solver. If parallelizable, we made use of the RRZN Cluster from the Leibniz University Hannover.

2.C.1 *Quantum trajectories*

Consider the time evolution of a pure state $\rho(t) = |\psi\rangle\langle\psi|$ for a master equation of the general form

$$\dot{\rho} = -i[H,\rho] + \gamma_k \sum_{k=1}^{N} a_k \rho a_k^\dagger - \frac{1}{2} a_k^\dagger a_k \rho - \frac{1}{2} \rho a_k^\dagger a_k. \tag{100}$$

With the definitions

$$|\tilde{\psi}_0\rangle = \left(1 - iH\mathrm{d}t - \sum_{k=1}^{N} a_k^\dagger a_k \mathrm{d}t\right) |\psi\rangle \tag{101}$$

$$|\tilde{\psi}_k\rangle = \sqrt{\gamma_k \mathrm{d}t} a_k |\psi\rangle, \qquad \text{for } k > 0 \tag{102}$$

the state after a short time $\mathrm{d}t$ is given by

$$\rho(t + \mathrm{d}t) \approx \sum_{k=0}^{N} |\tilde{\psi}_k\rangle\langle\tilde{\psi}_k|, \tag{103}$$

with an error on the order of $\mathcal{O}\left(\mathrm{d}t^2\right)$. On the level of wave functions Equation (103) is obviously equivalent to jump from the state $|\psi\rangle$ at time t into the (normalized) state $|\psi_k\rangle / ||\psi_k||$ at time $t + \mathrm{d}t$ with a probability of $||\psi_k||^2$. Averaging over m such probabilistic trajectories one can reconstruct the density matrix in the limit $m \to \infty$. When calculating a steady state density matrix it is helpful to note that this ensemble average over many trajectories is equivalent to a time average of a single trajectory.

In a numerical implementation one could calculate all probabilities $||\psi_k||^2$ in each time step and generate a random number between 0 and 1 with uniform distribution to select the state $|\psi_k\rangle$. It is however numerically more efficient to make use of the fact that $1 - ||\psi_0||^2 \propto \mathrm{d}t$ and thus in each time step it is most likely that $|\psi_0\rangle$ is selected. Such an algorithm would loop the following three steps:

- generate a random number p from a uniform distribution in the interval $[0, 1]$.
- propagate the state $|\phi\rangle$ with the efficient, non-Hermitian Hamiltonian $H - i\sum_k a_k^\dagger a_k$ with some efficient method (e.g. Runge Kutta) until $\|\phi\|^2 < p$.
- Probabilistically jump into one of the states $a_k|\phi\rangle / \|a_k|\phi\rangle\|$ with $k \geq 1$. The remaining probabilities p_k must be weighed according to $p_k \propto \gamma_k \|a_k|\phi\rangle\|^2$.

2.C.2 *Langevin equations*

A master equation can be translated to an equation of motion describing the system dynamics on the level of phase space distributions, see Section 2.A. If this equation contains derivatives only up to second order, it is of the general form

$$\partial_t P(\vec{x}) = -\sum_{j=1}^{N} \partial_{x_j} \mu_j(\vec{x}, t) P(\vec{x}, t) + \frac{1}{2} \sum_{j=1}^{N} \sum_{k=1}^{N} \partial_{x_j} \partial_{x_k} D_{jk}(\vec{x}, t) P(\vec{x}, t), \tag{104}$$

where P denotes one of the phase space distributions. Equation (104) is a Fokker-Planck equation, if the diffusion is everywhere positive, i.e. D is a positive matrix for all $\vec{x}$ and t. Such a Fokker-Planck equation can always be translated to the Itō-Langevin equation

$$\mathrm{d}x_j = \mu_j(\vec{x}, t)\, \mathrm{d}t + \sum_k \sigma_{jk}(\vec{x}, t)\, \mathrm{d}W_k, \tag{105}$$

where the matrix σ must fulfill $D_{lm}(\vec{x}, t) = \sum_k \sigma_{lk}(\vec{x}, t) \sigma_{mk}(\vec{x}, t)$ and the W_k are independent Wiener processes. Averaging many trajectories obeying Equation (105) the phase space distribution P is retrieved. The dimensionality is limited by the number of phase space variables N. E.g. for n 1-dimensional harmonic oscillator $N = 2n$, as each oscillator is described by x and p. Note that N scales only linearly with the number of systems, while for both numerical solutions of the master equation and the quantum jump method the scaling is exponential. Thus, if applicable, the Langevin simulation is usually by far the most efficient method. Therefore it is often also applied as an approximation for phase space equations that do contain higher derivatives, which have to be truncated to fit the Fokker-Planck template. The validity of this approximation has to be carefully verified from case to case.

Part II

OPTOMECHANICAL SELF-SUSTAINED OSCILLATIONS

3

LASER THEORY FOR OPTOMECHANICS

3.1 INTRODUCTION

In this chapter we study the most elementary optomechanical setup, where a single cavity mode couples to a single mechanical oscillator through, e.g., radiation pressure or dipole gradient forces. The dynamics of the system depends crucially on the frequency of the external driving field applied to the cavity: For the purpose of position or force sensing as in [20, 21] the driving field is chosen resonant. For back action cooling (as discussed in Section 2.1.5) or state transfer the field is tuned below the cavity frequency on the red side band [15, 16, 18]. For blue detuning the system exhibits a rather complex nonlinear behavior. When the driving field is swept from the red to the blue side the nonlinear dynamics sets in as a parametric amplification process where phonons and photons are created correlated in pairs [55]. This lies at the heart of the recently reported generation of optomechanical entanglement [19]. While this onset of mechanical oscillations may still be described by the linearized Hamiltonian from Section 2.1.5, the amplification will finally go over into a regime of self-sustained limit cycles due to the nonlinearity inherent to the optomechanical coupling, which requires a nonlinear description. The classical dynamics in this regime has been observed experimentally [56, 22, 57, 58, 25, 28] and is well studied theoretically [59, 60, 61, 62]. Motivated by the impressive progress towards quantum effects in optomechanical systems also the quantum regime of optomechanical limit cycles received significant attention in theoretical studies [63, 64, 65, 66, 67, 68, 69].

In particular, a recent numerical study of the full optomechanical master equation in the limit cycle regime showed that the Wigner function of the mechanical oscillator can become strongly negative [68]: Negativities of the Wigner function occur for driving fields at the blue sidebands and – more pronounced – also for resonant drive. Limit cycle states with negative Wigner density even exist in regions of red detuning where a (simple) classical model would not predict limit cycles at all. The numerical findings were independently confirmed in [69]. This reference predicts negative Wigner density even on higher sidebands and compares the extent of negativity found for different detunings in more detail. In view of these findings we develop in this chapter an appropriate analytical model to strive for a deeper understanding of these effects and the underlying mechanisms on its basis in the next Chapter 4.

The transition from parametric amplification to optomechanical limit cycles can be understood in analogy [1] to the threshold behaviour of a laser (or maser) cavity [70, 31, 53] where the roles of the laser cavity and the laser medium are played by, respectively, the mechanical oscillator and the optomechanical cavity [71]. Along this line a semiclassical rate equation model was derived in [71, 61] for optomechanical systems. Rodrigues and Armour [66, 67] developed a quantum mechanical treatment employing a truncated Wigner function approach to derive a Fokker-Planck equation (FPE) for the mechanical oscillator. The FPE predicted in particular a sub-Poissonian, or number-squeezed, phonon statistics in the limit cycle when the driving field is blue detuned from the cavity resonance by the mechanical oscillation frequency.

In this chapter we apply the laser theory due to Haake and Lewenstein [31, 53] introduced in Section 2.B.2 to describe optomechanical limit cycles in the quantum regime. Starting from the standard optomechanical master equation [14, 72] an effective FPE is derived for the quasi-probability distribution (such as e.g. the Wigner–, *P*– or *Q*–function) of the mechanical oscillator under adiabatic elimination of the cavity mode. The nonlinearity of the optomechanical interaction gives rise to nonlinear drift and diffusion coefficients in the FPE which describe, respectively, the (classical) nonlinear physics of limit cycles [59, 60] and the impact of quantum noise of the cavity. The approach taken here permits to work in a picture which interpolates between the dressed state picture introduced in [73, 74] through a polaron transformation and the bare state picture of the standard master equation [75, 14, 72, 66, 69]. Remarkably, in analogy to the polaron picture, this intermediate picture explicitly separates the optical Kerr-nonlinearity inherent to the radiation pressure from the optomechanical interaction. In contrast to the polaron picture, the interaction term is not removed from the master equation. Furthermore, both the mechanical oscillator and the cavity remain separate systems as in the standard master equation picture. In contrast, the polaron picture entangles cavity and oscillator. This entanglement complicates the description of the systems individually, which is desirable in the context of limit cycles. As we will show, the novel treatment of the optomechanical Kerr nonlinearity presented in this chapter can become essential to understand the physics of limit cycles.

The effective FPE derived here exactly reproduces the one of Rodriguez and Armour [66, 67] when neglecting the different description of the Kerr nonlinearity of the cavity, which is treated in the standard master equation picture there. In comparison to [66, 67] our approach does not require truncation of higher order derivatives, and gives a consistent and natural account of the Kerr nonlinearity.

---

[1] See Section 3.A for a more detailed comparison.

3.2 LASER THEORY FOR OPTOMECHANICS

3.2.1 *Haake-Lewenstein Laser Theory Ansatz in Optomechanics*

MASTER EQUATION — As our starting point we repeat here the standard [2] master equation of an optomechanical system [14, 72] introduced in Chapter 2

$$\frac{\mathrm{d}}{\mathrm{d}t}\rho = \left(\mathcal{L}_{\mathrm{m}} + \mathcal{L}_{\mathrm{c}} + \mathcal{L}_{\mathrm{int}}\right)\rho \tag{106}$$

where

$$\mathcal{L}_{\mathrm{m}}\rho = -i\left[\omega_{\mathrm{m}} b^{\dagger} b, \rho\right] + \gamma(\bar{n}+1)D[b]\rho + \gamma\bar{n}D[b^{\dagger}]\rho, \tag{107}$$

$$\mathcal{L}_{\mathrm{c}}\rho = -i\left[-\Delta a^{\dagger} a - iE\left(a - a^{\dagger}\right), \rho\right] + \kappa D[a]\rho \tag{108}$$

$$\mathcal{L}_{\mathrm{int}}\rho = -i\left[-g_0 a^{\dagger} a\left(b + b^{\dagger}\right), \rho\right]. \tag{109}$$

The three Liouvillians $\mathcal{L}_{\mathrm{m}}$, $\mathcal{L}_{\mathrm{c}}$, and $\mathcal{L}_{\mathrm{int}}$ refer to the mechanical oscillator, the cavity, and their interaction respectively. a and b denote the annihilation operators of the cavity and the mechanical oscillator. The frequency of the mechanical oscillator is ω_m, its amplitude damping rate is $\gamma = \omega_{\mathrm{m}}/Q_{\mathrm{m}}$, and its mean phonon number in thermal equilibrium $\bar{n}$. We use the notation $D[A]\rho = 2A\rho A^{\dagger} - A^{\dagger}A\rho - \rho A^{\dagger}A$ for Lindblad operators. κ is the cavity amplitude decay rate, $\Delta = \omega_{\mathrm{L}} - \omega_{\mathrm{c}}$ is the detuning from cavity resonance at ω_{c} of the driving field $E = \sqrt{2\kappa P_L/\hbar\omega_L}$ with power P_L and frequency ω_{L}. The master equation is written in a frame rotating at the frequency ω_{L} of the driving field. The optomechanical coupling per single photon is denoted by g_0, and essentially determines the dispersive shift of the cavity frequency with the displacement of the oscillator in units of the mechanical zero-point amplitude [3].

Our primary aim is to derive an effective equation of motion for the mirror based on the assumption that the dynamics of the cavity adiabatically follows the mechanical oscillator. This will be strictly the case when the cavity decay rate κ is larger than the characteristic coupling strength of the oscillator and the cavity mode (*i.e.* g_0 or the linear coupling $g = g_0\alpha$ enhanced by the mean cavity field α at the position of the limit cycle). As we will see, the resulting effective equation of motion for the mechanical oscillator gives good results for the stationary state also when this condition is fulfilled barely, and even when it is mildly violated.

---

[2] Note that in contrast to the more standard definition from Chapter 2 and e.g. [68, 59, 64] the definitions of γ and κ used here refer to the decay rate of the *amplitude* and will be used for all analytical results, in order to make the equations more readable. The corresponding decay rates for the energy $\kappa_E = 2\kappa$ and $\gamma_E = 2\gamma$ are the standard convention from [14]. For comparison to most experimental and numerical studies, we provide also the energy decay rates in the numerical results.

[3] The zero point amplitude is $\sqrt{\hbar/m\omega_{\mathrm{m}}}$ for an oscillator of mass m.

QUASIPROBABILITY DISTRIBUTION — Most importantly, we will not assume the usual linearization of the optomechanical coupling when we perform the adiabatic elimination. This is achieved by means of an Ansatz inspired by laser theory [31, 53], which allows us to use a *different* adiabatic reference state of the cavity field for *each* point in phase space of the mechanical oscillator. The idea is to switch to a phase-space representation for the mechanical degree of freedom, as introduced for the more general case in Section 2.B.2. In principle any quasi-probability distribution (*e.g.* P-distribution, Wigner function; compare Section 2.A) can be used, but we will in the following mostly focus on the (Husimi) Q function which yields the simplest formulas for the calculation presented below. In this formalism the density operator ρ is replaced by

$$\sigma(\beta, \beta^*) = \frac{1}{\pi}\langle\beta|\rho|\beta\rangle$$

where $|\beta\rangle$ is a coherent state of the mechanical oscillator. In Appendix 3.C we provide an extension and comparison of the present approach based on the Q function to a general (s-parameterized) quasi-probability distribution including the P-distribution and Wigner function as special cases. $\sigma(\beta, \beta^*)$ is a density operator for the cavity field and a quasi-probability distribution for the oscillator over the complex phase space variables (β, β^*). The reduced density operator for the cavity is obtained by integrating over phase space,

$$\rho_\mathrm{c} = \mathrm{tr}_\mathrm{m}\{\rho\} = \int \mathrm{d}^2\beta\, \sigma(\beta, \beta^*),$$

and the quasi-probability distribution (Q function) for the oscillator follows on taking the trace over the cavity,

$$Q(\beta, \beta^*) = \mathrm{tr}_\mathrm{c}\{\sigma(\beta, \beta^*)\}. \tag{110}$$

$\sigma(\beta, \beta^*)$ itself still contains all information about the state of both systems, and is fully equivalent to the density operator ρ. For the Q function the replacement rules [53]

$$b^\dagger\rho \to \beta^*\sigma(\beta, \beta^*), \qquad b\rho \to \left(\beta + \partial_{\beta^*}\right)\sigma(\beta, \beta^*), \tag{111}$$

and their adjoints can be applied to the master equation (106) in order to arrive at an equivalent description in phase space of the oscillator. We use the notation ∂_β to denote the partial derivative with respect to a variable β. The translated equation of motion is

$$\partial_t\, \sigma(\beta, \beta^*, t) = (\mathcal{L}_\mathrm{m} + \mathcal{L}_\mathrm{c} + \mathcal{L}_\mathrm{int})\, \sigma(\beta, \beta^*, t) \tag{112}$$

with

$$\begin{aligned}
\mathcal{L}_\mathrm{m}\sigma &= \left(\partial_\beta(\gamma - i\omega_\mathrm{m})\beta + \text{c.c.}\right)\sigma + 2\gamma(\bar{n}+1)\partial^2_{\beta\beta^*}\sigma && (113)\\
\mathcal{L}_\mathrm{c}\sigma &= L_c\sigma - i\left[-g_0\left(\beta+\beta^*\right)a^\dagger a, \sigma\right] \\
&= -i\left[-\left(\Delta + 2g_0\mathrm{Re}(\beta)\right)a^\dagger a - iE\left(a - a^\dagger\right), \sigma\right] + \kappa D[a]\sigma \\
\mathcal{L}_\mathrm{int}\sigma &= -ig_0\left(\partial_\beta\sigma a^\dagger a - \partial_{\beta^*}a^\dagger a\sigma\right). && (114)
\end{aligned}$$

The Liouvillian $\mathcal{L}_\mathrm{m}$ affects only the mechanical oscillator, and is just the Fokker-Planck version of Eq. (107). A crucial point in this formalism is that the nonlinear optomechanical interaction $\mathcal{L}_\mathrm{int}$ from Eq. (109) makes a contribution to both, the new Liouvillian for the cavity $\mathcal{L}_\mathrm{c}$ and the new interaction $\mathcal{L}_\mathrm{int}$. Parts of the interaction can thus formally be treated as a shift of the detuning by $2g_0\mathrm{Re}(\beta)$ which depends on the phase space variables (β, β^*). Note that Eq. (112) is still exactly equivalent to (106).

A SEMI-POLARON-TRANSFORMATION — The parametric dependence of the cavity detuning on the phase space variables can be transformed into one of the driving field E by means of a transformation

$$\begin{aligned}
\tilde{\sigma}(\beta, \beta^*, t) &= e^{\eta(\beta-\beta^*)a^\dagger a/2}\sigma(\beta, \beta^*, t)e^{-\eta(\beta-\beta^*)a^\dagger a/2} && (115)\\
&= e^{i\theta(\beta,\beta^*)a^\dagger a}\sigma(\beta, \beta^*, t)e^{-i\theta(\beta,\beta^*)a^\dagger a},
\end{aligned}$$

with

$$\theta(\beta, \beta^*) = \eta\,\mathrm{Im}(\beta), \qquad \eta = \frac{2g_0}{\omega_m}.$$

When transforming the equation of motion (112) care has to be taken on commuting the unitary operators in (115) with derivatives with respect to (β, β^*) in $\mathcal{L}_\mathrm{m}$ and $\mathcal{L}_\mathrm{int}$ due to the β-dependence of θ. Details are given in App. 3.B. The resulting equation of motion for $\tilde{\sigma}(\beta, \beta^*, t)$ can be written again in the form of Eq. (112),

$$\partial_t\,\tilde{\sigma}(\beta, \beta^*, t) = \left(\mathcal{L}_\mathrm{m} + \tilde{\mathcal{L}}_\mathrm{c} + \mathcal{L}_\mathrm{int}\right)\tilde{\sigma}(\beta, \beta^*, t), \qquad (116)$$

where $\mathcal{L}_\mathrm{m}$ and $\mathcal{L}_\mathrm{int}$ remain unchanged as in (113) and (114), and the Liouvillian operator for the cavity becomes

$$\begin{aligned}
\tilde{\mathcal{L}}_c\tilde{\sigma} = -i\left[-\Delta a^\dagger a - K(a^\dagger a)^2 - iE\left(e^{-i\theta(\beta,\beta^*)}a - \text{h.c.}\right), \tilde{\sigma}\right] \\
+ \kappa D[a]\tilde{\sigma}. \quad (117)
\end{aligned}$$

In this picture the phase of the driving field is different for each point in phase space (via $\theta(\beta, \beta^*)$), and the cavity acquires an effective Kerr nonlinearity of strength

$$K = \frac{g_0^2}{\omega_\mathrm{m}}.$$

We point out that the effective Kerr nonlinearity of the optomechanical interaction gives rise to ponderomotive squeezing of light, as was recently observed in [76, 77].

The equation of motion for $\tilde{\sigma}(\beta, \beta^*, t)$, Eq. (116), is an approximation. In principle it contains further terms which are of order Q_{m}^{-1} and whose explicit form is given in App. 3.C. For high quality oscillators these terms provide only small corrections and, therefore, will be dropped in the following. Apart from this approximation Eq. (116) still contains the full nonlinear dynamics of the system, while the aspect of the optical Kerr nonlinearity is explicitly separated from the nonlinearity in the optomechanical interaction. It is also important to note that the quasiprobability distribution for the reduced state of the oscillator still follows from the transformed state $\tilde{\sigma}(\beta, \beta^*, t)$ in Eq. (115) by taking the partical trace over the cavity

$$Q(\beta, \beta^*) = \mathrm{tr_c}\{\tilde{\sigma}(\beta, \beta^*)\}. \tag{118}$$

semi-polaron- versus polaron-transformation — The transformation in Eq. (115) has many parallels with the polaron transformation [78] which has been applied fruitfully to optomechanical systems in order to describe single-photon strong coupling effects [73, 74]. The polaron transformation is effected by a unitary transformation of the density operator

$$\tilde{\rho}_{\mathrm{pol}} = e^{\eta(b-b^\dagger)a^\dagger a/2} \rho e^{-\eta(b-b^\dagger)a^\dagger a/2} \tag{119}$$

which should be compared to the transformation in Eq. (115). Instead of (106) the transformed state $\tilde{\rho}$ fulfills a transformed master equation

$$\begin{aligned} \dot{\tilde{\rho}}_{\mathrm{pol}} &= (\mathcal{L}_{\mathrm{m}} + \tilde{\mathcal{L}}_{\mathrm{c}})\tilde{\rho}_{\mathrm{pol}}, & (120) \\ \tilde{\mathcal{L}}_{\mathrm{c}}\tilde{\rho}_{\mathrm{pol}} &= -i\left[-\Delta a^\dagger a - K(a^\dagger a)^2 - iE\left(e^{-\eta(b-b^\dagger)/2}a - \mathrm{h.c.}\right), \tilde{\rho}_{\mathrm{pol}}\right] \\ &\quad + \kappa D\left[e^{-\eta(b-b^\dagger)/2}a\right]\tilde{\rho}_{\mathrm{pol}}, & (121) \end{aligned}$$

where L_{m} is given in Eq. (107). This equation is again correct up to terms of order Q_{m}^{-1}. It is instructive to compare the master equation in the polaron picture (120) to the equation of motion (116) attained in our "semi-polaron transformation". In both equations of motion the Liouvillians for the cavity, Eqs. (117) and (121) respectively, exhibit a Kerr nonlinearity and contain a driving field whose phase depends on the momentum of the oscillator. Crucially, the polaron transformation changes the jump operator describing cavity decay from a to $e^{i\eta(b-b^\dagger)/2}a$, and entirely removes the interaction term (109). Moreover, since the polaron picture corresponds to a transformation into dressed states of the optomechanical system the partial trace of $\tilde{\rho}_{\mathrm{pol}}$ over the (dressed) cavity mode does not give the reduced state of the mechanical oscillator, cf. Eq. (119). In contrast, the semi-polaron transformation introduced here retains a nonlinear interaction $\mathcal{L}_{\mathrm{int}}$, Eq. (114), leaves the jump operator for cavity decay unchanged, and conserves the important relation (118). These properties are crucial in order to perform second order perturbation theory in $\mathcal{L}_{\mathrm{int}}$, and to derive an effective equation of motion for the mechanical oscillator as a separate system. For further comments on the semi-polaron transformation we refer to Appendix 3.B.

3.2.2 *Fokker-Planck Equation for the Mechanical Oscillator*

INTERACTION PICTURE — Our goal is now to adiabatically eliminate the cavity field from the dynamics, similar to the analysis of sideband cooling [75]. This requires that the cavity dynamics, governed by $\tilde{\mathcal{L}}_c$ in (117) with dominant characteristic time scale κ, is fast as compared to all other time scales in $\mathcal{L}_{\mathrm{m}}$ and $\mathcal{L}_{\mathrm{int}}$. Since we aim to cover in particular also the resolved sideband regime, $\omega_{\mathrm{m}} > \kappa$, we move to an interaction picture with respect to the free harmonic motion of the mirror. The equation of motion is still given by Eq. (116) where $\mathcal{L}_{\mathrm{m}}$ describes thermal decay only,

$$\mathcal{L}_{\mathrm{m}}\sigma = \gamma\left(\partial_\beta\beta + \partial_{\beta^*}\beta^* + 2(\bar{n}+1)\partial^2_{\beta\beta^*}\right)\sigma, \tag{122}$$

and $\tilde{\mathcal{L}}_{\mathrm{c}}$ and $\mathcal{L}_{\mathrm{int}}$ become explicitly time-dependent,

$$\tilde{\mathcal{L}}_c\sigma = -i\left[-\Delta a^\dagger a - K(a^\dagger a)^2 - iE\left(e^{-i\theta(\beta,\beta^*,t)}a - \mathrm{h.c.}\right), \sigma\right] + \kappa D[a]\sigma, \tag{123}$$

$$\mathcal{L}_{\mathrm{int}}\sigma = -ig_0\left(e^{i\omega_{\mathrm{m}}t}\partial_\beta\sigma a^\dagger a - \mathrm{h.c.}\right). \tag{124}$$

The phase of the driving field is $\theta(\beta,\beta^*,t) = \eta\,\mathrm{Im}\left(\beta\, e^{-i\omega_{\mathrm{m}}t}\right)$.

In the adiabatic elimination it is assumed that the cavity essentially remains in the (quasi) stationary state of its undisturbed (by $\mathcal{L}_{\mathrm{int}}$) dynamics,

$$\dot{\rho}_{\mathrm{c}} = \tilde{\mathcal{L}}_{\mathrm{c}}\rho_{\mathrm{c}} \tag{125}$$

with $\tilde{\mathcal{L}}_{\mathrm{c}}$ given by (123). This Liouvillian describes the dynamics of a Kerr nonlinear cavity driven by an amplitude- and phase-modulated field,

$$Ee^{i\theta(\beta,\beta^*,t)} = E\sum_{n=-\infty}^{\infty} J_n\left(-\eta|\beta|\right)e^{in(\omega_{\mathrm{m}}t-\phi)}, \tag{126}$$

where J_n are Bessel functions. Note that the partial amplitudes depend on the mechanical phase space variable $\beta = |\beta|e^{i\phi}$. We do not attempt to solve Eq. (125) exactly. While in fact an exact solution for the stationary state of a Kerr nonlinear cavity exists [79] for the case of a constant driving field (*i.e.* $\theta \equiv$ const.), no such state can be expected for the present situation. Due to the periodic modulation of the driving field the cavity will not settle into a strictly stationary state, but rather to quasi-stationary state with a periodic time-dependence. If the Kerr nonlinearity is neglected an exact solution for this quasi-stationary state can be constructed by means of a Floquet series Ansatz [80]. However, in the present case both aspects, modulated drive and Kerr nonlinearity, are important and shall be taken into account.

In order to arrive at an approximate solution of Eq. (125) which can serve as a (β-dependent) reference state for the adiabatic elimination of the cavity we will follow two complementary approaches in the paragraphs below: In the first one we assume the cavity is driven to a state of large mean amplitude, which we determine self-consistently from an essentially classical nonlinear dynamics. The fluctuations around this mean field will be treated in a linearized model as Gaussian noise. The second approach concerns the case of a weak driving fields for which the cavity essentially stays close to its ground (vacuum) state, which corresponds to the regime considered in [66, 67]. In this case the master equation Eq. (125) can be expanded and directly solved on the low lying Fock states.

In both cases we aim to retain a nonlinear dynamics for the mean cavity amplitude, and use a linearized description for fluctuations. Formally this is done by switching to a displaced frame, defining $\tilde{\tilde{\sigma}} = D(\alpha(t))\tilde{\sigma}D^\dagger(\alpha(t))$ where $D(\alpha) = \exp(\alpha a^\dagger - \alpha a)$. We choose $\alpha(t) \in \mathbb{C}$ such that the terms of dominant order in α are canceled from the transformed master equation for $\tilde{\tilde{\sigma}}$. In the case of $|\alpha(t)| \gg 1$ ($|\alpha(t)| \ll 1$) we cancel the terms of third (up to first) order in α and then neglect the terms up to first (of third) order in α. The full equation of this transformation may be found in Eq. (155) of this chapter's appendix, we proceed here with its most important features:

DISPLACED FRAME FOR THE LIMIT $|\alpha(t)| \gg 1$ — In the limit $|\alpha(t)| \gg 1$ we identify $\alpha(t)$ with the long time solution of

$$\dot{\alpha}(t) = -\left[\kappa - i\left(\Delta + 2K|\alpha(t)|^2\right)\right]\alpha(t) + Ee^{i\theta(\beta,\beta^*,t)}, \tag{127}$$

which formally follows from the requirement that terms of third order in α cancel in the resulting master equation for the displaced state $\tilde{\tilde{\sigma}}$ are canceled. Due to the Kerr nonlinearity the dynamics described by this equation of motion can be bistable. On assuming a single stable solution we preclude bistable regimes from our description. For a constant phase θ bistability occurs only for driving fields which are red detuned with respect to the cavity resonance for detunings $\Delta < -\sqrt{3}\kappa$, cf. Section 2.1.6. For the present case of a modulated drive no such simple condition can be given. However, it is reasonable to expect that bistability will become an issue only when the driving field has sufficient spectral weight for frequencies with a detuning below $-\sqrt{3}\kappa$. In the following we are mainly concerned with the cases of resonant or blue detuned drive, for which it turns out that bistability is not an issue [81, 82, 83].

From Eq. (127) and (126) we can expect that in the long time limit the cavity amplitude will be of the form

$$\alpha(\beta,\beta^*,t)=\sum_{n=-\infty}^{\infty}\alpha_n(\beta,\beta^*)e^{in\omega_m t}. \tag{128}$$

Inserting this expression into (127) one sees that the effective detuning experienced by the cavity will be dominantly given by the DC component of $|\alpha(t)|^2$, such that it is useful to define an effective detuning

$$\Delta_{\text{eff}}(\beta,\beta^*)=\Delta+2K\sum_n|\alpha_n(\beta,\beta^*)|^2. \tag{129}$$

Eq. (129) has to be read as a non-linear equation for Δ_{eff}. In regimes where more than one solution exists, the system will be bi- or multistable, and we have to expect large photon number fluctuations. The validity of our approach will thus be limited to regions where only a single stable solution for Δ_{eff} exists, as discussed above. We seek an approximate solution to (127) by assuming a fixed effective detuning Δ_{eff}, such that

$$\alpha_n=\frac{E}{h_n}J_n\left(-\eta|\beta|\right)e^{-in\phi}, \tag{130}$$

$$h_n=\kappa+i(n\omega_m-\Delta_{\text{eff}}), \tag{131}$$

where we follow the notation of [66, 67]. In total $\alpha(t)$ in (128) depends on the mechanical phase space variable β through both $\Delta_{\text{eff}}(\beta,\beta^*)$ and the β-dependent driving field $Ee^{i\theta(\beta,\beta^*,t)}$. We will see that the β-dependence in $\Delta_{\text{eff}}(\beta,\beta^*)$ is a crucial effect for the case of resonant cavity-drive (for which $\Delta_{\text{eff}}\lesssim\kappa$).

The Liouvillians after the transformation with $D(\alpha(t))$ are

$$\begin{aligned}\mathcal{L}_{\text{m}}\sigma &= \gamma\left(\partial_\beta\beta+\partial_{\beta^*}\beta^*+2(\bar{n}+1)\partial^2_{\beta\beta^*}\right)\sigma\\ &\quad -ig_0\left(\partial_\beta e^{i\omega_{\text{m}}t}|\alpha(t)|^2-\text{h.c.}\right)\sigma, \qquad (132)\\ \tilde{\mathcal{L}}_c\sigma &= -i\left[-\left(\Delta+4K|\alpha(t)|^2\right)a^\dagger a-K\left(\alpha(t)^2a^{\dagger 2}+h.c.\right),\sigma\right]\\ &\quad +\kappa D[a]\sigma, \qquad (133)\\ \mathcal{L}_{\text{int}}\sigma &= -ig_0\left(e^{i\omega_{\text{m}}t}\partial_\beta\sigma(\alpha^*(t)a+\alpha(t)a^\dagger)+\text{h.c.}\right) \qquad (134)\end{aligned}$$

The Liouvillian for the mechanical oscillator, $\mathcal{L}_{\text{m}}$, acquires an additional drift term (second line in (132)) with a nonlinear drift coefficient $\propto e^{i\omega_{\text{m}}t}|\alpha(\beta,\beta^*,t)|^2$ which contains in particular the nonlinear DC force and dynamic back action effects (*i.e.* optical damping and frequency shifts), as will be discussed below. In the Liouvillian for the cavity, $\tilde{\mathcal{L}}_{\text{c}}$, terms of order $\alpha(t)$ and lower have been dropped. The leading terms of order α^2 describe squeezing dynamics and an effective detuning. Finally, in $\mathcal{L}_{\text{int}}$ only the term of linear order in α has been kept. Note also that when moving to the displaced frame commutators of the (β-dependent) displacement operators and derivatives with respect to β have been neglected. They would add corrections to the Liouvillians of higher order in g_0. We have now removed the driving field from the dynamics of the cavity. The remaining Liouvillian (133) describe the Gaussian evolution of fluctuations:

The ponderomotive squeezing of the light field is naturally contained in the $\alpha^2 a^{\dagger 2}$-term and its hermitian conjugate. While in this thesis we will only study parameters for which this squeezing is negligible, the effect of ponderomotive squeezing back on the mirror after the adiabatic elimination of the cavity is an interesting perspective for future applications of our new formalism: In the adiabatic elimination of the cavity one would have to use a squeezed reference state, which can introduce possibly additional diffusion terms in the motion of the mirror. Applied to the situation of limit cycles, this may also alter the state of the mechanical oscillator.

Curiously, the Kerr nonlinearity induces a different effective detuning for the mean field α than for the fluctuations (compare Eqs. (127) and (133)). This is consistent with results for a Kerr nonlinear cavity [79]. We therefore define

$$\tilde{\Delta}_{\text{eff}} = \Delta + 4K \sum_n |\alpha_n|^2. \tag{135}$$

The fast decay rate to the vacuum is still given by κ from the original master Eq. (108).

This can be used in order to adiabatically eliminate the cavity taking into account second order effects in the optomechanical interaction $\propto g_0$, Eq. (134), very much in the spirit of laser cooling theory [75]. Details of the calculation can be found in Appendix 3.D. The result is an effective equation of motion for the mechanical oscillator in the form of a Fokker-Planck equation

$$\begin{aligned}
\dot{Q}(\beta,\beta^*) = g_0^2 \sum_n & \left(\partial_{\beta^*} \partial_\beta \frac{\alpha_n^* \alpha_n}{\tilde{h}_{n-1}} - \partial_{\beta^*} \partial_{\beta^*} \frac{\alpha_{n-2}^* \alpha_n}{\tilde{h}_{n-1}} \right) Q(\beta,\beta^*) + h.c. \\
& + i g_0 \sum_n \left(\partial_{\beta^*} \alpha_{n-1}^* \alpha_n \right) Q(\beta,\beta^*) + h.c. \\
& + \gamma \left(\partial_\beta \beta + \partial_{\beta^*} \beta^* + 2(\bar{n}+1) \partial^2_{\beta\beta^*} \right) Q(\beta,\beta^*)
\end{aligned} \tag{136}$$

for the Q-function of the mechanical oscillator. In analogy to h_n we define $\tilde{h}_n = \kappa + i(n\omega_m - \tilde{\Delta}_{\text{eff}})$ with $\tilde{\Delta}_{\text{eff}}$ given in (135).

The drift and diffusion coefficients in the Fokker-Planck equation (136) do not depend on the phase of β as a consequence of the rotating wave approximation involved in its derivation. We therefore transform the Fokker-Planck equation to polar coordinates $\beta = re^{i\phi}$, and focus on the time evolution of the oscillator amplitude r by integrating out the phase variable ϕ. The time evolution for r is then a one dimensional Fokker-Planck equation (on a half space),

$$\dot{Q}(r) = -\partial_r \mu(r) Q(r) + \partial_r^2 D(r) Q(r) \tag{137}$$

with drift $\mu(r)$ and diffusion coefficient $D(r)$

$$\mu(r) = -\gamma r + \sum_n g_0 E^2 \mathrm{Im}\left[\frac{J_{n-1}(\eta r) J_n(\eta r)}{h_{n-1} h_n^*}\right] \tag{138}$$

$$D(r) = \frac{\gamma(\bar{n}+1)}{2} + \sum_n \frac{g_0^2 E^2}{2}\left(\frac{\kappa J_n(\eta r)^2}{|h_n|^2 |\tilde{h}_{n-1}|^2} - \mathrm{Re}\left[\frac{J_{n-2}(\eta r) J_n(\eta r)}{\tilde{h}_{n-1} h_{n-2}^* h_n}\right]\right). \tag{139}$$

The details of the transformation may again be found in Appendix 3.D. Equation (137) admits a potential solution in steady state which is given by (up to normalization)

$$Q(r) \propto \frac{e^{I(r)}}{D(r)}, \qquad I(r) := \int_0^r \frac{\mu(r')}{D(r')} \mathrm{d}r'. \tag{140}$$

This solution is valid for any value of Δ, such that it covers both the regime of optomechanical cooling and the regime of self-induced oscillations. In [75] an effective equation of motion for the oscillator was derived in order to study the limits of sideband cooling under linearization (cf. Section 2.1.4) of the dynamics and adiabatic elimination of the cavity using a coherent state as a reference state. The present approach generalizes this calculation to the nonlinear regime by using a different reference state for each phase space point of the oscillator. The non-linear quantum dynamics has been described analytically using a method based on the classical theory for limit cycles [84] and by means of Langevin equations [66], and has been applied in great detail to limit cycles, but also to the cooling regime [67]. The results of our calculation reproduce these results in the regime of a negligible Kerr-Term and provide suitable extensions in those cases where the Kerr nonlinearity of the cavity becomes a dominant effect. In the next section we will compare the analytical expression for the steady state of the mechanical to numerical solutions of the exact master equation (106) to study the limit cycle regime. We conclude this section by briefly stating the corresponding results for the limit of small intracavity field amplitude, followed by a comparison of limit cycles studied in different laser setups.

DISPLACED FRAME AND ADIABATIC ELIMINATION FOR THE LIMIT $|\alpha(t)| \ll 1$ — In the case of $|\alpha(t)| \ll 1$ all steps can be performed in analogy. The difference is that we need to cancel the terms up to first order in α and then neglect the terms of third order in α. The effective detuning now is given by

$$\Delta_{\mathrm{eff}} = \Delta + K, \tag{141}$$

i.e. the bare detuning is just shifted by the constant Kerr term in this extreme regime. No distinction between Δ_{eff} and $\tilde{\Delta}_{\text{eff}}$ needs to be made. The adequate choice for the displacement amplitude is the long term solution of

$$\dot{\alpha}(t) = -\left[\kappa - i\Delta_{\text{eff}}\right]\alpha(t) + Ee^{i\theta(\beta,\beta^*,t)}. \tag{142}$$

The result of the adiabatic elimination is structurally the same, α_n and h_n are given as in equations (130) and (131), but with the effective detuning now given as in (141). In Eq. (139) the $\tilde{h}_n$ are simply replaced by h_n.

3.3 CONCLUSION

In this chapter we studied the quantum regime of optomechanical limit cycles. Based on the Laser theory of Haake and Lewenstein [31] we derived an effective Fokker-Planck equation for an optomechanical system. The analytical prediction for the oscillator's steady state is in agreement with the work of Rodrigues and Armour [66, 67].

Our treatment naturally includes also the Kerr effect, which becomes important for large g_0^2/ω_m. One consequence important for the quantum theory of limit cycles is the shift of the detuning of equation (141), which occurs even without photons in the cavity, and had to be introduced phenomenologically in [67]. This shift explains the possibility of limit cycles on the blue sideband in [68].

We believe that the present approach provides a suitable starting point for further studies of optomechanical systems in the limit of strong couplings. We point out once more that in the "semi-polaron picture" introduced here the Kerr nonlinearity and the optomechanical interaction occur as independent terms. This enables in principle to take into account the squeezed noise of the cavity when deriving effective equations of motion of the mechanical oscillator. While for the parameters considered in this thesis we could neglect this effect, additional diffusion for the mechanical oscillator is to be expected for very strong laser drive. This would apply to the case of limit cycles, but could also become important in the cooling regime.

APPENDIX TO CHAPTER 3

3.A QUANTUM LIMIT CYCLES IN LASERS

It seems natural to base a model of optomechanical limit cycles on theory used in the context of lasers [70, 31, 53], where quantum limit cycles have been extensively studied most prominently. The standard laser system consists of a reservoir of many atoms which forms a bath for the cavity mode. The pumped atoms will drive the laser mode to a high amplitude limit cycle, where it settles into a coherent state with random phase.

A setup that can be driven to highly sub-Poissonian states is the regularly pumped laser [85, 86], where excited atoms fly through a cavity. The mechanism works in the situation, where at each time approximately only one atom interacts with the light mode and the interaction is a swapping of excitations. In the case of more regular than Poissonian statistics of the pump, the fluctuation of the transmitted energy decreases and the light mode will have sub-Poissonian phonon statistics. This setup is sometimes also referred to as one atom laser/maser or micro maser, because the events when more than one atom interacts with the field can be neglected.

The one atom laser is different from the 'one-and-the-same' atom laser [87], where a single atom is trapped inside a cavity and drives the laser mode. Also in this setup a sub-Poissonian steady can be reached and the explanation again relies on counting the number of interactions exchanged between the atom and the cavity [88].

In our optomechanical system a single laser mode is the bath driving the mechanical oscillator. The bath consisting of only a single mode is in analogy to some extent to the micro maser, as stressed in [69], and even more similar to the 'one-and-the-same' atom laser. Even though we also describe sub-Poissonian boson statistics, the analytical techniques developed e.g. in [88] cannot be readily applied to our situation, because they crucially rely one the preservation of total excitations by the interaction, which is not given in the optomechanical setup. Our analytical model 3.2 is based on [31], which was first developed for the standard setup without sub-Poissonian statistics.

For the creation of non-Gaussian states a nonlinearity is required. In the optomechanical setup the nonlinearity stems from the interaction, while in the 'one-and-the-same' atom laser it stems from the two level nature of the bath, which is equivalent to a highly nonlinear cavity.

3.B SEMI-POLARON TRANSFORMATION

The semi-polaron transformation, Eq. (115) in Sec. 3.2, is introduced in terms of the formalism of quasiprobability distributions. In view of the similarities of this transformation with the polaron transformation in Eq. (119) the question arises how the semi-polaron transformation in Eq. (115) can be expressed in terms of an ordinary operator representation. The transformed state $\tilde{\sigma}$ in (115) fulfills

$$\partial_\eta \tilde{\sigma} = \left[\frac{1}{2}\left(\beta - \beta^*\right) a^\dagger a, \tilde{\sigma}\right] = \frac{1}{2}\left[a^\dagger a, \tilde{\sigma}\beta - \beta^* \tilde{\sigma}\right]. \tag{143}$$

When written in the second form we can apply the replacement rules (111) to write the last equation in operator representation

$$\begin{aligned}
\partial_\eta \tilde{\rho} &= \frac{1}{2}\left[a^\dagger a, \tilde{\rho} b - b^\dagger \tilde{\rho}\right] \\
&= \frac{1}{4}\left[(b - b^\dagger) a^\dagger a, \tilde{\rho}\right] + \frac{1}{4}\left(D[b^\dagger + a^\dagger a] - D[b^\dagger] - D[a^\dagger a]\right)\tilde{\rho} \\
&\equiv L_{\mathrm{s-pol}} \tilde{\rho}
\end{aligned} \tag{144}$$

In the second line we expressed the generator for the semi polaron transformation in terms of a commutator with a Hamiltonian and three Lindblad terms. The semi polaron transformation in operator representation is thus

$$\tilde{\rho} = \exp\left(\eta L_{\mathrm{s-pol}}\right)\rho.$$

It becomes equivalent to the polaron transformation if the Lindblad terms in the generator $L_{\mathrm{s-pol}}$ are dropped. Thus, the semi polaron transformation is non-unitary. In the context of adiabatic elimination of a cavity mode in the bad cavity limit a similar transformation to a "dissipation picture" was employed in [89, 90].

3.C TRANSFORMATIONS FOR GENERAL PHASE SPACE DISTRIBUTION

SEMI-POLARON TRANSFORMATION In the main text we introduced the semi-polaron transformation only for the special case of the Q-function, to make the equations more readable. Here we drop this restriction and assume the more general case of an s-parameterized phase space distribution P_s with $s \in [-1, 1]$. For the convenience of the calculation we define $p = \frac{s+1}{2} \in [0, 1]$ and $q = 1 - p$. Note that for $q = 0$ this corresponds to the Glauber-Sudarshan P-representation, for $q = \frac{1}{2}$ to the Wigner representation, and for $q = 1$ to the Husimi Q-representation.

Starting from the standard optomechanical Hamiltonian and Lindblad operators we first switch to a displaced and rotating frame with frequency ω_m for the mechanical oscillator so that $b \to \beta_0 + b e^{-i\omega_m t}$

and introduce the shorthand notation $b_t = be^{-i\omega_m t}$. This transformation also leaves the Lindblad operators unchanged and the Hamiltonian transforms to

$$\begin{aligned} H = &(\omega_m + i\gamma)\beta_0^* b_t + (\omega_m - i\gamma)\beta_0 b_t^\dagger \\ &- g_0(\beta_0 + \beta_0^*)a^\dagger a \\ &- \Delta a^\dagger a - g_0 a^\dagger a \left(b_t + b_t^\dagger\right) - iE\left(a - a^\dagger\right). \end{aligned} \tag{145}$$

Using the translation rules

$$b\rho \to (\beta + q\partial_{\beta^*})\sigma \qquad\qquad b^\dagger\rho \to (\beta^* - p\partial_\beta)\sigma \tag{146}$$

we obtain the translated equation of motion $\dot{\sigma}(\beta, \beta^*) = \mathcal{L}_c\sigma + \mathcal{L}_m\sigma + \mathcal{L}_{int}\sigma$. With the shorthands $\beta_t = \beta e^{-i\omega_m t}$ and $\partial_{\beta_t} = \partial_\beta e^{i\omega_m t}$ this gives

$$\begin{aligned} \mathcal{L}_c\sigma = &-i\left[-g_0(\beta_0 + \beta_0^*)a^\dagger a - \Delta a^\dagger a - g_0 a^\dagger a\left(\beta_t + \beta_t^*\right), \sigma\right] \\ &- i\left[-iE\left(a - a^\dagger\right), \sigma\right] + L_c\sigma \end{aligned} \tag{147}$$

$$\mathcal{L}_{int}\sigma = -ig_0\left((q\partial_{\beta_t} - p\partial_{\beta_t^*})\sigma a^\dagger a - (q\partial_{\beta_t^*} - p\partial_{\beta_t})a^\dagger a\sigma\right) \tag{148}$$

$$\mathcal{L}_m\sigma = -i(\omega_m + i\gamma)\beta_0^*\partial_{\beta_t^*}\sigma + i(\omega_m - i\gamma)\beta_0\partial_{\beta_t}\sigma + I_m\sigma. \tag{149}$$

with

$$I_m = \gamma\left(\partial_\beta\beta + \partial_{\beta^*}\beta^*\right) + 2\gamma(\bar{n} + q^2 + pq)\partial_{\beta^*}\partial_\beta \tag{150}$$

$$L_c = \kappa D[a]. \tag{151}$$

In analogy to transformation (115) we apply the more general

$$\tilde{\sigma}(t) = \exp\left[-i\theta(t)a^\dagger a\right]\sigma(t)\exp\left[i\theta(t)a^\dagger a\right],$$

with $\lambda = \lambda_r + i\lambda_i = \frac{g_0}{\omega_m + i\gamma}$ and $\theta(t) = i\left(\lambda\beta e^{-i\omega_m t} - \lambda^*\beta^* e^{i\omega_m t}\right)$. Using the notation with $K = \frac{g_0^2}{\omega_m}$ this gives after dropping terms of order $\frac{1}{Q}$ as an approximation,

$$\mathcal{L}_c\sigma = -i\left[-\Delta a^\dagger a - K(a^\dagger a)^2 - iE\left(e^{i\theta(t)}a - e^{-i\theta(t)}a^\dagger\right), \sigma\right] + L_c\sigma \tag{152}$$

$$\mathcal{L}_{int}\sigma = -ig_0\left((q\partial_{\beta_t} - p\partial_{\beta_t^*})\sigma a^\dagger a - (q\partial_{\beta_t^*} - p\partial_{\beta_t})a^\dagger a\sigma\right) \tag{153}$$

$$\mathcal{L}_m\sigma = I_m\sigma - i(\omega_m + i\gamma)\beta_0^*\partial_{\beta_t^*}\sigma + i(\omega_m - i\gamma)\beta_0\partial_{\beta_t}\sigma. \tag{154}$$

We now transform to a displaced frame $\tilde{\sigma} = D^\dagger(\alpha)\sigma D(\alpha)$ with parameter $\alpha(\beta, t) \in \mathbb{C}$. For a master equation of the form

$$\dot{\rho} = -i\left[-\Delta a^\dagger a - K(a^\dagger a)^2 - i\left(E(t)a - E^*(t)a^\dagger\right), \rho\right] + L_c\rho$$

the transformation to a displaced frame $\tilde{\rho} = D^\dagger(\alpha(t))\rho D(\alpha(t))$ gives

$$\begin{aligned} \dot{\tilde{\rho}} = L\tilde{\rho} - i[&-(\Delta + 4K|\alpha|^2)a^\dagger a - K(a^\dagger a)^2 \\ &- K\left(\alpha^2(a^\dagger)^2 + (\alpha^* a + \alpha a^\dagger)a^\dagger a + h.c.\right) \\ &- i\left\{\left(\dot{\alpha} + (\kappa - i\Delta - i2K|\alpha|^2)\alpha - E\right)a^\dagger - \text{h.c.}\right\}, \tilde{\rho}] \end{aligned} \tag{155}$$

Depending on wether one wants to study the regime $|\alpha| \gg 1$ or $|\alpha| \ll 1$, either the terms with low or high order in α can be neglected at this point and a different choice of $\alpha(t)$ is required to cancel all displacement-like terms.

DISPLACED FRAME FOR $|\alpha| \gg 1$ We can cancel the displacement-like terms, which include the terms of order $K|\alpha|^3$, by imposing that $\alpha(t)$ solves

$$\dot{\alpha}(t) = \left(i(\Delta + 2K|\alpha(t)|^2) - \kappa\right) \alpha(t) + E(t)$$

such that in the displaced frame

$$\begin{aligned}\dot{\tilde{\rho}} = & -i[-(\Delta + 4K|\alpha|^2)a^\dagger a \\ & - K\left(\alpha^2(a^\dagger)^2 + (\alpha^* a + \alpha a^\dagger)a^\dagger a + h.c.\right) - K(a^\dagger a)^2, \tilde{\rho}] + L\tilde{\rho}.\end{aligned} \tag{156}$$

Neglecting the terms proportional to K up to first order in α, the Liouvillians are

$$\mathcal{L}_c\sigma = -i\left[-(\Delta + 4K|\alpha|^2)a^\dagger a - K\left(\alpha^2(a^\dagger)^2 + h.c.\right), \sigma\right] + L_c\sigma \tag{157}$$

$$\begin{aligned}\mathcal{L}_{int}\sigma = & -ig_0(q\partial_{\beta_t} - p\partial_{\beta_t^*})\sigma(\alpha^* a + \alpha a^\dagger) \\ & + ig_0(q\partial_{\beta_t^*} - p\partial_{\beta_t})(\alpha^* a + \alpha a^\dagger)\sigma\end{aligned} \tag{158}$$

$$\begin{aligned}\mathcal{L}_m\sigma = & -ig_0(\partial_{\beta_t} - \partial_{\beta_t^*})|\alpha|^2\sigma + I_m\sigma \\ & - i(\omega_m + i\gamma)\beta_0^*\partial_{\beta_t^*}\sigma + i(\omega_m - i\gamma)\beta_0\partial_{\beta_t}\sigma\end{aligned} \tag{159}$$

Note that now, in analogy to laser theory, $\mathcal{L}_m$ reproduces the classical drift. We have now $|\mathcal{L}_{int}| \propto g_0|\alpha| \ll g_0\langle a^\dagger a\rangle \approx g_0|\alpha|^2$, where $\langle a^\dagger a\rangle$ refers to the average before the transformation.

DISPLACED FRAME FOR $|\alpha| \ll 1$ If we restrict the analysis to only the lowest two Fock states, the operators consisting of three creation/annihlation-operators resulting from transformation (155) can be approximated with just one operator, e.g. $aa^\dagger a \approx a$. This time we neglect the terms proportional to K of third order in α. By imposing that $\alpha(t)$ solves this time

$$\dot{\alpha}(t) = (i(\Delta + K) - \kappa)\,\alpha(t) + E(t), \tag{160}$$

we can cancel the remaining displacement-like terms. The Liouvillians are now

$$\mathcal{L}_c\sigma = -i\left[-\Delta a^\dagger a - K\left(a^\dagger a\right)^2 - K\left(\alpha^2(a^\dagger)^2 + h.c.\right), \sigma\right] + L_c\sigma \tag{161}$$

$$\begin{aligned}\mathcal{L}_{int}\sigma =& -ig_0(q\partial_{\beta_t} - p\partial_{\beta_t^*})\sigma(\alpha^* a + \alpha a^\dagger + a^\dagger a)\\ &+ ig_0(q\partial_{\beta_t^*} - p\partial_{\beta_t})(\alpha^* a + \alpha a^\dagger + a^\dagger a)\sigma \end{aligned}\tag{162}$$

$$\begin{aligned}\mathcal{L}_m\sigma =& -ig_0(\partial_{\beta_t} - \partial_{\beta_t^*})|\alpha|^2\sigma + I_m\sigma\\ &- i(\omega_m + i\gamma)\beta_0^*\partial_{\beta_t^*}\sigma + i(\omega_m - i\gamma)\beta_0\partial_{\beta_t}\sigma \end{aligned}\tag{163}$$

3.D DERIVATION OF FOKKER-PLANCK EQUATION

In order to obtain the approximate Fokker-Planck equation for the mechanical oscillator, we now eliminate the cavity in second order perturbation theory. We show this in detail for $|\alpha| \gg 1$ and then briefly write down the results for $|\alpha| \ll 1$.

ADIABATIC ELIMINATION OF THE CAVITY IN THE $|\alpha| \gg 1$ REGIME

Let us for now ignore I_m and re-include it later. Defining $\sigma_{ij} := \langle i|\sigma|j\rangle$ and cutting off after index $(i,j) = (1,1)$ we get the EOM

$$\begin{aligned}\dot{\sigma}_{00} =& 2\kappa\sigma_{11}\\ &+ ig_0\left((q\partial_{\beta_t^*} - p\partial_{\beta_t})\alpha_t^*\sigma_{10} - (q\partial_{\beta_t} - p\partial_{\beta_t^*})\alpha_t\sigma_{01}\right)\\ &+ ig_0\left(\partial_{\beta_t^*}\alpha_t^*\alpha_t\sigma_{00} - \partial_{\beta_t}\alpha_t^*\alpha_t\sigma_{00}\right)\\ &- i(\omega_m + i\gamma)\beta_0^*\partial_{\beta_t^*}\sigma_{10} + i(\omega_m - i\gamma)\beta_0\partial_{\beta_t}\sigma_{10} \end{aligned}\tag{164}$$

$$\begin{aligned}\dot{\sigma}_{11} =& -2\kappa\sigma_{11}\\ &+ ig_0\left((q\partial_{\beta_t^*} - p\partial_{\beta_t})\alpha_t\sigma_{01} - (q\partial_{\beta_t} - p\partial_{\beta_t^*})\alpha_t^*\sigma_{10}\right)\\ &+ ig_0\left(\partial_{\beta_t^*}\sigma_{11} - \partial_{\beta_t}\sigma_{11}\right) + ig_0\left(\partial_{\beta_t^*}\alpha_t^*\alpha_t\sigma_{11} - \partial_{\beta_t}\alpha_t^*\alpha_t\sigma_{11}\right)\\ &- i(\omega_m + i\gamma)\beta_0^*\partial_{\beta_t^*}\sigma_{11} + i(\omega_m - i\gamma)\beta_0\partial_{\beta_t}\sigma_{11} \end{aligned}\tag{165}$$

$$\begin{aligned}\dot{\sigma}_{10} =& -\kappa\sigma_{10} + i\tilde{\Delta}_{\text{eff}}\sigma_{10} + ig_0\partial_{\beta_t^*}\sigma_{10}\\ &+ ig_0\left((q\partial_{\beta_t^*} - p\partial_{\beta_t})\alpha_t\sigma_{00} - (q\partial_{\beta_t} - p\partial_{\beta_t^*})\alpha_t\sigma_{11}\right)\\ &+ ig_0\left(\partial_{\beta_t^*}\alpha_t^*\alpha_t\sigma_{10} - \partial_{\beta_t}\alpha_t^*\alpha_t\sigma_{10}\right)\\ &- i(\omega_m + i\gamma)\beta_0^*\partial_{\beta_t^*}\sigma_{10} + i(\omega_m - i\gamma)\beta_0\partial_{\beta_t}\sigma_{10} \end{aligned}\tag{166}$$

We now adiabatically eliminate σ_{10} to first order in g_0 (note that σ_{11} is already of order g_0^2. Also note that the mean amplitude β_0 is chosen such that it cancels the zero frequency component of $|\alpha|^2$ acting on the mechanical drift.):

$$\sigma_{10}(t) = \int_0^\infty \mathrm{d}\tau e^{-\kappa\tau + i\tilde{\Delta}_{\text{eff}}\tau} ig_0(q\partial_{\beta_{t-\tau}^*} - p\partial_{\beta_{t-\tau}})\alpha_{t-\tau}\sigma_{00}(t) \tag{167}$$

$$= ig_0\sum_n(q\partial_{\beta^*}e^{i(n-1)\omega_M t}\frac{\alpha_n}{\tilde{h}_{n-1}} - p\partial_\beta e^{i(n+1)\omega_M t}\frac{\alpha_n}{\tilde{h}_{n+1}})\sigma_{00}(t) \tag{168}$$

where $h_n = \kappa + i(n\omega_M - \tilde{\Delta}_{\text{eff}})$ and $\alpha = \sum_{n=-\infty}^{\infty} \alpha_n e^{in\omega_m t}$ with $\alpha_n = \Xi_n e^{-in\phi}$. Now the derivative of the phase space distribution is approximately given by $\dot{P}_s(\beta, \beta^*) \approx \text{Tr}(\dot{\sigma}_{00}(\beta, \beta^*) + \dot{\sigma}_{11}(\beta, \beta^*))$, which gives to second order in g_0

$$\begin{aligned}\dot{P}_s = \sum_n q^2 g_0^2 &\left(\partial_{\beta^*}\partial_\beta \frac{\alpha_n^*\alpha_n}{\tilde{h}_{n-1}} - \partial_{\beta^*}\partial_{\beta^*} \frac{\alpha_{n-2}^*\alpha_n}{\tilde{h}_{n-1}}\right) P_s \\ &+ p^2 g_0^2 \left(\partial_{\beta^*}\partial_\beta \frac{\alpha_n^*\alpha_n}{\tilde{h}_{n+1}} - \partial_\beta\partial_\beta \frac{\alpha_{n+2}^*\alpha_n}{\tilde{h}_{n+1}}\right) P_s \\ &+ pq g_0^2 \left(\partial_{\beta^*}\partial_\beta \left(\frac{\alpha_n^*\alpha_n}{\tilde{h}_{n+1}} + \frac{\alpha_n^*\alpha_n}{\tilde{h}_{n-1}}\right) - \partial_\beta^2 \frac{\alpha_{n+2}^*\alpha_n}{\tilde{h}_{n+1}} - \partial_{\beta^*}^2 \frac{\alpha_{n-2}^*\alpha_n}{\tilde{h}_{n-1}}\right) P_s \\ &+ i g_0 \left(\partial_{\beta^*}\alpha_{n-1}^*\alpha_n\right) P_s + h.c., \end{aligned} \tag{169}$$

where we neglected terms $\propto \frac{1}{r}$ as they are negligible at the position of the limit cycle. Note that the drift term does not depend on the choice of phase-space distribution. For the Q-function the equation implies to

$$\begin{aligned}\dot{Q} = g_0^2 \sum_n &\left(\partial_{\beta^*}\partial_\beta \frac{2\kappa\alpha_n^*\alpha_n}{|\tilde{h}_{n-1}|^2} - \partial_{\beta^*}\partial_{\beta^*} \frac{\alpha_{n-2}^*\alpha_n}{\tilde{h}_{n-1}} - \partial_\beta\partial_\beta \frac{\alpha_{n-2}\alpha_n^*}{\tilde{h}_{n-1}^*}\right) Q \\ &+ i g_0 \sum_n \left(\partial_{\beta^*}\alpha_{n-1}^*\alpha_n - \partial_\beta \alpha_{n-1}\alpha_n^*\right) Q, \end{aligned} \tag{170}$$

and for the Wigner function to

$$\begin{aligned}\dot{W} = \sum_n \frac{g_0^2\kappa}{|\tilde{h}_{n+1}|^2} &\left(\partial_{\beta^*}\partial_\beta \left(|\alpha_n|^2 + |\alpha_{n+2}|^2\right) - \partial_\beta^2 \alpha_{n+2}^*\alpha_n - \partial_{\beta^*}^2 \alpha_n^*\alpha_{n+2}\right) W \\ &+ i g_0 \sum_n \left(\partial_{\beta^*}\alpha_{n-1}^*\alpha_n - \partial_\beta \alpha_{n-1}\alpha_n^*\right) W \end{aligned} \tag{171}$$

TRANSFORMATION TO POLAR COORDINATES We are finally interested in the EOM for polar coordinates (r, ϕ). When previously $\int \mathrm{d}\alpha \mathrm{d}\alpha^* P_s(\alpha, \alpha^*) = 1$ the new normalization is $\int r \mathrm{d}r \mathrm{d}\phi P_s(r, \phi) = 1$. With

$$\partial_x = \cos(\phi)\partial_r - \frac{\sin(\phi)}{r}\partial_\phi \tag{172}$$

$$\partial_y = \sin(\phi)\partial_r + \frac{\cos(\phi)}{r}\partial_\phi \tag{173}$$

we get

$$\partial_\beta = \tfrac{1}{2} e^{-i\phi} \left(\partial_r - \frac{i}{r}\partial_\phi\right) \tag{174}$$

$$\partial_{\beta^*} = \tfrac{1}{2} e^{i\phi} \left(\partial_r + \frac{i}{r}\partial_\phi\right) \tag{175}$$

and

$$(2\partial_\beta)^2 = e^{-2i\phi} \left(\partial_r^2 - 2\frac{i}{r}\partial_{r\phi} + 2\frac{i}{r^2}\partial_\phi - \frac{1}{r}\partial_r - \frac{1}{r^2}\partial_\phi^2\right) \tag{176}$$

$$(2\partial_\beta)(2\partial_\beta^*) = \partial_r^2 + \frac{1}{r}\partial_r + \frac{1}{r^2}\partial_\phi^2 \tag{177}$$

Integrating out ϕ and again neglecting terms $\propto \frac{1}{r}$ we get e.g. for the Q-distribution

$$\dot{Q} = \sum_n g_0 \partial_r \left(\text{Im}\left[\Xi_{n-1}\Xi_n^*\right]\right) Q + \frac{g_0^2}{2}\partial_r^2 \left(\frac{\kappa \Xi_n^* \Xi_n}{|\tilde{h}_{n-1}|^2} - \text{Re}\left[\frac{\Xi_{n-2}^* \Xi_n}{\tilde{h}_{n-1}}\right]\right) Q \tag{178}$$

or, in compact form with $J_n := J_n\left(-\eta r\right)$ and re-including the effect of I_m, this gives the parameters

$$D_Q = \frac{\gamma(1+\bar{n})}{2} + \sum_n \frac{g_0^2 E^2}{2} \left(\frac{\kappa J_n J_n}{|h_n|^2 |\tilde{h}_{n-1}|^2} - \text{Re}\left[\frac{J_{n-2} J_n}{\tilde{h}_{n-1} h_{n-2}^* h_n}\right]\right) \tag{179}$$

$$\mu_Q = -\gamma r - \sum_n g_0 E^2 \left(\text{Im}\left[\frac{J_{n-1} J_n}{h_{n-1} h_n^*}\right]\right) \tag{180}$$

for the FPE:

$$\dot{P}_s = -\partial_r \mu_s P_s + \partial_r^2 D_s P_s \tag{181}$$

that can be solved (up to normalization) as

$$P_s(r) \propto \frac{e^{I_s(r)}}{D_s(r)}, \qquad I_s(r) := \int_0^r \frac{\mu_s(r')}{D_s(r')} \mathrm{d}r'. \tag{182}$$

The corresponding equation for the Wigner function has the same drift coefficient and a diffusion of

$$\begin{aligned} D_W(r) = {} & \frac{\gamma(2\bar{n}+1)}{4} \\ & + \sum_n \frac{\kappa g_0^2 E^2}{4|\tilde{h}_{n+1}|^2} \left(\left|\frac{J_{n+2}}{h_{n+2}}\right|^2 + \left|\frac{J_n}{h_n}\right|^2 - \frac{J_n J_{n+2}}{h_n h_{n+2}^*} - \frac{J_n J_{n+2}}{h_n^* h_{n+2}} \right). \end{aligned} \tag{183}$$

In both cases we assume in steady state that $P_s(r,\phi) = P_s(r)$, i.e. the distributions are independent of ϕ.

FOKKER-PLANCK EQUATION FOR $|\alpha|^2 \ll 1$ The procedure of the adiabatic elimination is in complete analogy to $|\alpha|^2 \gg 1$. One only has to replace Δ_{eff} and $\tilde{\Delta}_{\text{eff}}$ with $\Delta_K = \Delta + K$ and adjust the solution of α as in Eq. (160). With $h_n = \kappa + i(n\omega_m - \Delta_K)$ The final coefficients for the Fokker-Planck equation then have the same structure but without the distinction between h_n and $\tilde{h}_n$. E.g. for the Q-function one obtains

$$D_Q = \frac{\gamma(1+\bar{n})}{2} + \sum_n \frac{g_0^2 E^2}{2} \left(\frac{\kappa J_n J_n}{|h_n|^2 |h_{n-1}|^2} - \text{Re}\left[\frac{J_{n-2} J_n}{h_{n-1} h_{n-2}^* h_n}\right]\right) \tag{184}$$

$$\mu_Q = -\gamma r - \sum_n g E^2 \left(\text{Im}\left[\frac{J_{n-1} J_n}{h_{n-1} h_n^*}\right]\right) \tag{185}$$

4

QUANTUM SIGNATURES IN OPTOMECHANICAL LIMIT CYCLES

4.1 INTRODUCTION

In this chapter, which can be read as a continuation of chapter 3, we apply the model derived there to show that it correctly reproduces the characteristics of limit cycles in the standard optomechanical setup. It identifies general requirements on system parameters (such as coupling strength, driving power, sideband resolution, temperature etc.) for the occurrence of sub-Poissonian phonon statistics and negative Wigner functions, and establishes a tight connection between the two phenomena. We find that negative Wigner functions can be achieved also in rather classical parameter regimes where the coupling per single photon g_0 is smaller than the cavity line width, and where the cavity is driven strongly and limit cycle amplitudes are large. The associated small Fano factors are lower bounded by, and can reach, the sideband parameter κ/ω_m (ratio of cavity line width to mechanical resonance frequency) for sufficiently strong optomechanical cooperativity. We confirm the analytical results with numerical simulations using Quantum Jump Trajectories.

As an introduction to our study, we sum up some known results on limit cycles that the rest of this chapter refers to. First, we introduce the theory for the amplitude of classical limit cycles as developed in [59, 64], and then we recapitulate the numerical results on nonclassical states of quantum limit cycles as reported in [68]. When comparing these findings to our analytical treatment developed in the previous chapter we will be mainly concerned with the special case of close to resonant driving field, $\Delta_\mathrm{eff} \simeq \kappa \ll \omega_m$. Therefore, we start out by stating some approximate expressions for this case.

CLOSE TO RESONANT DRIVE — In the sideband-resolved regime and with a detuning close to the resonance, i.e. $\Delta_\mathrm{eff}, \kappa \ll \omega_m$ (but not necessarily $\Delta_\mathrm{eff} \ll \kappa$) we keep only the terms with $n = 0, 1$ in the expression for the drift coefficient, Eq. (138), and approximate

$$\mu(r) \simeq -\gamma r + \frac{g_0 E^2}{\omega_m^2} \frac{2\kappa\Delta_\mathrm{eff}(r)}{\Delta_\mathrm{eff}^2(r) + \kappa^2} J_0(\eta r) J_1(\eta r). \tag{186}$$

In the sideband-resolved regime, the equation for the effective detuning, Eq. (129), becomes a third order polynomial in Δ_eff and in the limit $\Delta_\mathrm{eff} \ll \kappa$ it even simplifies to a simple and explicit expression

$$\Delta_\mathrm{eff}(r) \simeq \Delta + 2\frac{KE^2}{\kappa^2} J_0^2(\eta r). \tag{187}$$

CLASSICAL LIMIT CYCLES — The theory for classical optomechanical limit cycles from [59] is reproduced by the drift-part of the Fokker-Planck equation, Eq. (138), when neglecting the diffusion and using a constant effective detuning, $\Delta_{\text{eff}}(r) = \Delta_{\text{eff}} \equiv \text{const}$. Disregarding the diffusion the oscillator amplitude $r(t)$ evolves fully deterministically and obeys

$$\dot{r} = \mu(r) = -\gamma_{\text{eff}}(r)r, \qquad \gamma_{\text{eff}}(r) = \gamma + \gamma_{\text{opt}}(r).$$

Following Eq. (186) the combined intrinsic and optically induced damping of the oscillator $\gamma_{\text{eff}}(r)$ close to resonance is then given as the sum of the intrinsic mechanical damping γ and the amplitude-dependent optical damping

$$\gamma_{\text{opt}}(r) = -\frac{g_0 E^2}{\omega_m^2} \frac{2\kappa\Delta_{\text{eff}}}{\Delta_{\text{eff}}^2 + \kappa^2} \frac{J_0(\eta r) J_1(\eta r)}{r}. \tag{188}$$

Note that the sign of the optically induced damping at $r = 0$ coincides with the sign of Δ_{eff}. For negligible intrinsic damping, $\gamma \ll |\gamma_{\text{opt}}|$, one can then expect limit cycles to always start for $\Delta_{\text{eff}} > 0$ (whereas the dynamics will be stable for $\Delta_{\text{eff}} < 0$). The possible amplitudes r_0 for limit cycles are given by the conditions $\gamma_{\text{eff}}(r_0) = 0$ and $\gamma'_{\text{eff}}(r_0) > 0$. The first condition is equivalent to

$$\frac{J_0(\eta r) J_1(\eta r)}{r} = \gamma \frac{\omega_m^2}{g_0 E^2} \frac{\Delta_{\text{eff}}^2 + \kappa^2}{2\kappa\Delta_{\text{eff}}}. \tag{189}$$

The left hand side of this equation has infinitely many roots as the Bessel functions oscillate at a constant amplitude, cf. Fig. 7 a). The envelope is given by the r^{-1} decay. As illustrated in Fig. 7 a) the exact position of the limit cycle and the number of possible amplitudes is then determined by the right hand side of Eq. (189).

4.2 OUTLINE

In the following sections we will explain two features of limit cycles on resonance that can be heavily influenced by the Kerr term:

First, in Sec. 4.3 we show that in the strong driving limit $|\alpha|^2 \gg 1$ the phase transition between optomechanical cooling and self-induced oscillations is crucially determined by the dynamical dependence of the effective detuning on the intracavity amplitude and its corresponding nonlinear dependence on the cycle amplitude, cf. Eq. (187). This behavior can also be explained in a classical picture.

We then develop an explanation of the interesting numerical result for limit cycles in the quantum regime reported in [68, 69]: For approximately resonant driving fields, $\Delta \simeq 0$, and at the blue detuned sideband resonance, $\Delta \simeq \omega_m$, the steady state of the mechanical oscillator can have a Wigner function with a negative area. The requirement on the strength of the optomechanical coupling g_0 is more

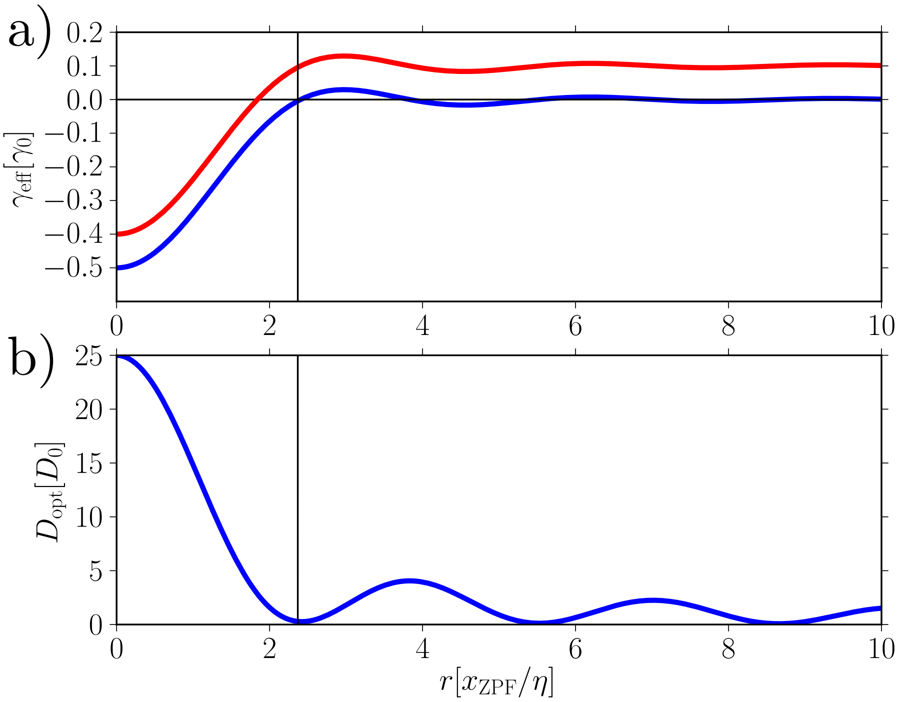

Figure 7: Plot a) shows the effective damping $\gamma_{\mathrm{eff}}(r) = \gamma + \gamma_{\mathrm{opt}}(r)$ from Eq. (188) in units of $\gamma_0 = \frac{g_0 E^2}{\omega_m^2} \frac{2\kappa\Delta_{\mathrm{eff}}}{\Delta_{\mathrm{eff}}^2+\kappa^2}$ versus cycle amplitude r in units of the mechanical zero point fluctuation and $\eta = 2g_0/\omega_m$. The blue and red line are two examples for different intrinsic damping γ. Limit cycles are stable at roots of the total damping with a positive slope. This happens only once for the red dashed line with $\gamma = 0.1\gamma_0$, corresponding to only one possible amplitude for the oscillation. For the blue solid line with $\gamma = 0$ many such intersections occur and the oscillator amplitude will in general jump between those different meta-stable points.
Plot b) shows the optical part of the diffusion from approximation (194) for $\kappa/\omega_m = 0.1$ and $\Delta_{\mathrm{eff}} = \kappa$ in units of $D_0 = \kappa g_0^2 E^2/\omega_m^4$. Note that the dominant part of the diffusion from Eq. (194) is exactly canceled at the position of the limit cycle for $\gamma = 0$, as indictated by the vertical line. This cancellation explains the strongly sub-Poissonian phonon statistics for such parameters.
Note that both drift and diffusion are a function of r, in contrast to the linearized theory presented in Section 2.1.5.

stringent at the sideband than on resonance where non-classical limit cycles appear already for weaker coupling. Curiously, on resonance the numerical solution to the master equation predicts (non-classical) limit cycles also for parameters where classically the effective detuning $\Delta_{\mathrm{eff}} < 0$, and one would expect a stable cooling dynamics. Fig. 8 shows the steady-state Wigner function of the mechanical oscillator for such parameters.

We will use the analytical description of limit cycles with the Fokker-Planck equation to explain the features displayed in Fig. 8, and to predict general requirements on system parameters to achieve a non-

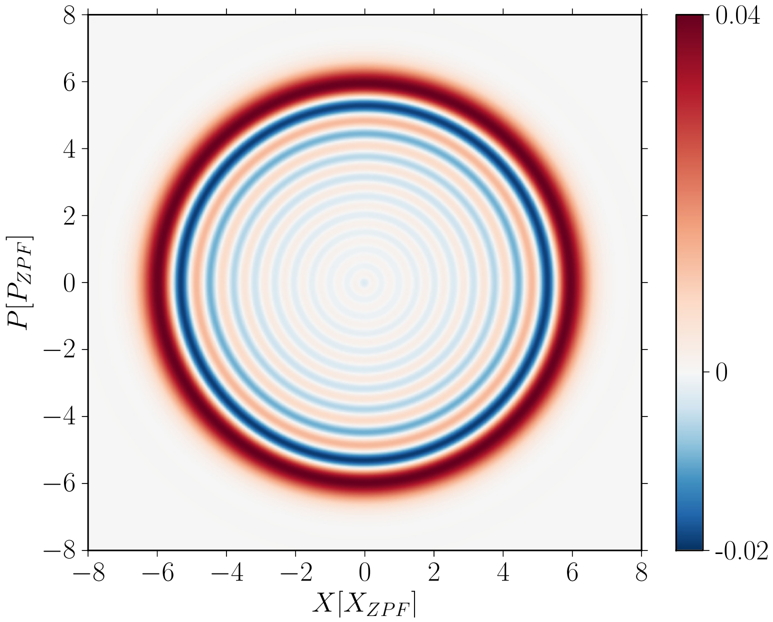

Figure 8: Wigner function W of the lowest metastable limit cycle of the mechanical oscillator for parameters $(g_0, \kappa_E = 2\kappa, \gamma, E, \Delta, K) = (0.275, 0.1, 0, 0.15 - 0.026, 0.076) \times \omega_m$. As there are less than 0.03 photons in the cavity we are in the regime of $|\alpha|^2 \ll 1$, where $\Delta_{\text{eff}} = \Delta + K$, cf. equation (141). Choosing the bare detuning to minimize the Fano factor (F=0.1 at the attractor with lowest amplitude, which is depicted in this plot) implies according to equation (196) $\Delta = \kappa - K$, which for the strong optomechanical coupling of this example gives the negative numerical value $\Delta = -0.026$. Note that classically, or excluding the Kerr effect, a limit cycle would not even start for these parameters. The minimal value of W in this plot is -0.02.

positive Wigner function. In Section 4.5 we show that the occurrence of negative Wigner functions in turn is intimately linked to achieving a small variance of the phonon statistics, as characterized by a small Fano factor $F = \langle \Delta n \rangle^2 / \langle n \rangle$, along with a small cycle amplitude r_0. We analyze the variance of the phonon number in Section 4.4 and find that the conditions for small Fano factor are favorable at the $\Delta = 0$-resonance.

In Section 4.6 we describe the numerical method used to check the analytical predictions. It allows for the first time to numerically study quantum features of optomechanical limit cycles in the regime of large mechanical amplitudes and strong laser drive, populating many states of the cavity. We find that the analytical model can still be applied and even for $g_0 < \kappa$ negativity of the Wigner function can be observed.

4.3 DRIFT AND DYNAMICAL DETUNING

In this section we study in detail the time evolution of the mean amplitude $\bar{r}$, which is determined by the drift $\mu(r)$ in (186). In particular we show how the dynamical dependence of $\Delta_{\text{eff}}(r)$ on r gives new results which are not observed in any model based on a static detuning (like the one we used above). We focus on the regime where $\bar{r}$ is larger than its standard deviation Δr, such that we can derive the time evolution of $\bar{r}$ via $\dot{\bar{r}} = \mu(\bar{r})$ directly from (186) as

$$\dot{\bar{r}} = -\gamma\bar{r} + \frac{2\kappa g E^2}{\omega_m^2}\frac{\Delta_{\text{eff}}(\bar{r})}{\Delta_{\text{eff}}(\bar{r})^2 + \kappa^2} J_0(\eta\bar{r}) J_1(\eta\bar{r}). \tag{190}$$

These assumptions are fulfilled for small $\eta = \frac{2g_0}{\omega_m}$, because $\eta\bar{r}$ is the argument of the Bessel functions and hence $\bar{r} \propto \frac{1}{\eta}$.

With the oscillator initially in the ground state, it is the sign of $\Delta_{\text{eff}}(0)$ that determines if the limit cycle starts at all: For $\Delta_{\text{eff}}(0) < 0$ the optical damping is initially positive and no oscillation starts, but for $\Delta_{\text{eff}}(0) > 0$ it is negative and may be larger than the intrinsic damping γ, so that a self-induced oscillations can start. The oscillator arrives at its steady state, when $\dot{\bar{r}} = 0$. Neglecting the small corrections due to γ, this is equivalent to the condition $\Delta_{\text{eff}}(\bar{r}) J_0(\eta\bar{r}) J_1(\eta\bar{r}) = 0$. If the effective detuning Δ_{eff} is independent of r, the smallest root of this product is always the first root of J_0. This corresponds to the standard situation (as discussed above) valid for a negligible Kerr parameter or in the weak driving limit, cf. Eq. (141).

In the converse case, for large amplitudes $|\alpha|^2 \gg 1$ and non-negligible Kerr parameter, the dynamic nature of the effective detuning can become important: The smallest root of the product $\Delta_{\text{eff}}(\bar{r}) J_0(\eta\bar{r}) J_1(\eta\bar{r})$ is then determined either by J_0 or Δ_{eff}, depending on the sign of Δ. If the bare detuning is on the blue (heating) side, $\Delta \gtrsim 0$, the condition for the limit cycle is still $J_0(\eta r_0) = 0$ as in the case of a static detuning. However, if the bare detuning is on the red (cooling) side $\Delta < 0$ the effective detuning for a small cycle amplitude can still be positive as $\Delta_{\text{eff}}(0) = \Delta + 2KE^2/\kappa^2$, cf. Eq. (187). This is the case in particular for a driving field E larger than a critical value of $E_{\text{crit}} = \frac{\kappa}{\sqrt{2}g_0}\sqrt{|\Delta|\omega_M}$. The sign of $\Delta_{\text{eff}}(r)$ will then depend on, and ultimately change with, the increasing amplitude r of the oscillation since $\Delta_{\text{eff}} = \Delta < 0$ at the roots of $J_0^2(\eta r)$. With increasing oscillator amplitude r the DC-component of the cavity occupation and hence (via the Kerr nonlinearity) also the shift of the detuning drops. The steady state amplitude r_0 of the limit cycle is reached when $\Delta_{\text{eff}}(r_0) = 0$. Using again approximation (187) the condition $\Delta_{\text{eff}}(r_0) = 0$ is equivalent to $J_0(\eta r_0) = \frac{\kappa}{\sqrt{2}g_0 E}\sqrt{|\Delta|\omega_M}$. Thus, the Kerr nonlinearity smoothes the transition from cooling to amplification. This is in contrast to models with a static detuning where a sharp transitions occurs at $\Delta_{\text{eff}} = 0$.

We numerically check the dynamical nature of the detuning by integrating the equations of motion

$$\dot{\alpha} = i(\Delta + g_0(\beta + \beta^*)\alpha - \kappa\alpha + E, \quad \dot{\beta} = ig_0|\alpha|^2 - i\omega_m\beta - \gamma\beta, \tag{191}$$

which are the classical analogue to the master equation (106). Fig. 9 illustrates the time dependence of the detuning with an example of a time evolution where the bare detuning $\Delta < 0$, so that the limit cycle amplitude r_0 in steady state is determined by the condition $\Delta_{\text{eff}}(r) = 0$. Fig. 10 shows that this condition gives a good prediction for r_0 as a function of Δ.

An approximation similar to equation (190) for the case of a laser drive close to the first blue sideband, $\Delta \approx \omega_m$, shows that there the position of the limit cycle does not depend on the exact value of Δ. It is approximately given by the first root of $J_1(\eta r)$. Thus the limit cycle amplitude is generally smaller on resonance than on the sideband. We use this observation in Section 4.5, where we will see that a small limit cycle amplitude is favorable for the occurrence of a negative area in the Wigner function.

4.4 DIFFUSION AND FANO FACTOR

Having discussed the conditions for a limit cycle to start and having derived the mean amplitude in steady state for the $\Delta \simeq 0$ resonance, we now consider the fluctuations caused by the diffusion D around this mean value to derive a prediction for the Fano factor

$$F = (\langle n^2 \rangle - \langle n \rangle^2)/\langle n \rangle = \langle \Delta n \rangle^2 / \langle n \rangle, \tag{192}$$

which is a measure for number squeezing: For a coherent state the phonon distribution is Poissonian so that $\langle \Delta n \rangle^2 = \langle n \rangle$ and $F = 1$. A state with sub-Poissonian phonon variance can hence be characterized by $F < 1$.

We will use the term Fano factor in the context of limit cycles as follows: For generic parameters an optomechanical system can exhibit several limit cycles, such that the Fano factor of the full density matrix typically is larger than one. The oscillations at each of these attractors are metastable, such that it is possible to consider the phonon statistics at a particular limit cycle. Especially in the relatively classical regime where g_0/ω_m is not too large the cycles will be well separated. When we refer to Fano factor, we will implicitly always mean the Fano factor of one particular attractor.

We obtain the mean and variance of the phonon number n via [53]

$$\langle \left\{ a^r (a^\dagger)^s \right\}_{sym} \rangle = \int d^2\alpha W(\alpha, \alpha^*) \alpha^r (\alpha^*)^s, \tag{193}$$

where $W(\alpha, \alpha^*)$ is the Wigner function. We use here the Wigner function because it gives better agreement with the numerical analysis

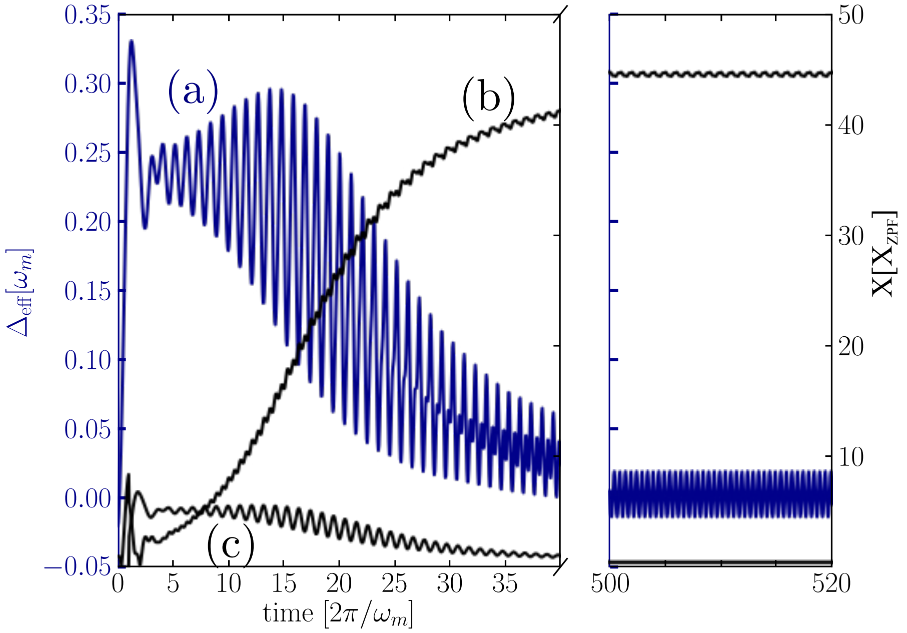

Figure 9: Example of the oscillator time-evolution for the classical equations of motion, see equation (191), with initial condition $r = 0$ for $\Delta \lesssim 0$ but $\Delta_{\text{eff}}(r = 0) > 0$. Effective detuning $\Delta_{\text{eff}}(t)$ (a) with scale on the left (blue) axis, oscillator amplitude $r(t)$ (b) and DC-shift in position (c) with scale on the right (black) axis. A positive effective detuning at $r \approx 0$ ensures that the limit cycle starts. With increasing oscillator amplitude the intra-cavity photon number $\sum_n |\alpha_n|^2$ from Eq. (129) drops and hence also Δ_{eff}. As $\mu \propto \Delta_{\text{eff}}$, see Eq. (186), the oscillator settles in steady state as soon as this drop reaches $\Delta_{\text{eff}} = 0$. The parameters in this plot are $(E, g_0, \kappa_E = 2\kappa, \gamma_E = 2\gamma) = (4.0, 0.05, 0.3, 2 \cdot 10^{-5}) \times \omega_m$.

for the statistics of the phonon number than other quasi-probability distributions. Drift and diffusion coefficients for the Wigner function are calculated in App. 3.C along the same lines as shown above for the Q-function. In particular, close to resonance the radial diffusion coefficient as relevant to the Wigner function is

$$D_W = \frac{\gamma(1+2\bar{n})}{4} + \frac{\kappa g_0^2 E^2}{\omega_m^4} \left(J_1^2(\eta r) + \frac{1}{2} \frac{\omega_m^2}{\kappa^2 + \Delta_{\text{eff}}^2} J_0^2(\eta r) \right), \tag{194}$$

where we applied to equation (183) the same approximations as in Sec. 4.1 for the drift coefficient.

For most amplitudes the J_0^2-term is dominant, as it is enhanced by at least $(\omega_m/\kappa)^2$ over the J_1^2-term. For parameters where the optical anti-damping is much stronger than the intrinsic mechanical decay, a curious cancellation of the diffusion occurs in steady state: The limit cycle will then settle exactly at the first root of J_0 as discussed in Section 4.3. There the term proportional to J_1^2, which is suppresed by $(\kappa/\omega_m)^2$, becomes the only relevant term in the diffusion. This suppression is illustrated in Figure 7 b) and can be intuitively explained:

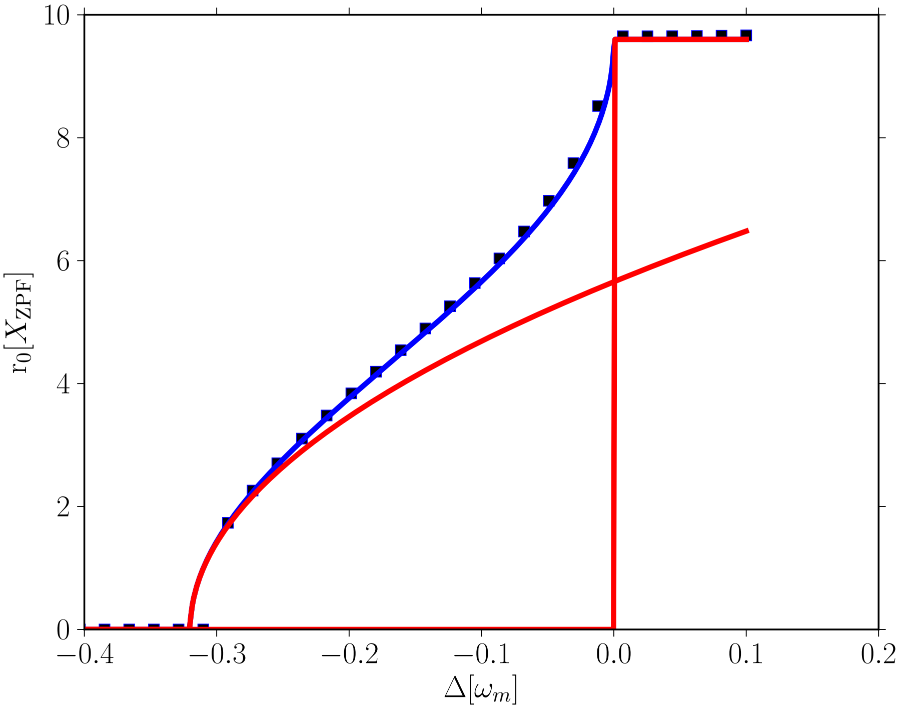

Figure 10: Amplitude r_0 for the first stable limit cycle versus bare detuning Δ. In the limit of an amplitude-independent effective detuning (red) the values for large amplitudes are predicted correctly. It is known from [59] that for small amplitudes at the onset of limit cycles, the amplitude follows a square root (red). With inclusion of the dynamical effective detuning $\Delta_{\mathrm{eff}}(r)$ (blue) the limit cycle amplitude r_0 follows $J_0(\eta r_0) = \frac{\kappa}{\sqrt{2}g_0 E}\sqrt{|\Delta|\omega_M}$, both limiting cases are reproduced, and the whole transition between the regimes of damping and antidamping can be described. In this figure we compare the predictions with the numerical solution (dots) of the classical equation. The parameters of this plot are $(E, g_0, \kappa_E = 2\kappa, \gamma) = (0.5, 0.25, 0.3, 0.0) \times \omega_m$.

The last two terms in equation (171) (or equivalently (183)) are the (coherent) squeezing terms. For $n = 1$ they exactly cancel the corresponding (incoherent) diffusion terms $\propto \partial_{\beta^*}\partial_{\beta^*}$ in leading order and only the higher order terms in $\kappa^2/\omega_{\mathrm{m}}^2$ remain. Because of this suppression of diffusion in the sideband-resolved regime one can obtain a very small Fano factor of the mechanical oscillator, as we show below.

The phase space distribution in steady state is given by Eq. (140). In the limit of small g_0/ω_m, where $\Delta n \ll \langle n \rangle$, and for the case of only a single stable limit cycle centered around a position r_0 with $\mu(r_0) = 0$, we linearize $\mu(r) \approx \mu(r_0) + \mu'(r_0)(r - r_0)$ around this r_0 and set $D(r) \simeq D(r_0)$ so that the corresponding solution for W is approximately

$$W(r) \propto \exp\left(-\frac{(r - r_0)^2}{2\sigma^2}\right). \tag{195}$$

with $\sigma^2 = -D(r_0)/\mu'(r_0)$. One can then derive the approximate expression $F \simeq 4\sigma^2$ for the limit $\omega_m/g_0 > \sigma$. In the sideband-resolved regime and with the limit cycle position at the first root of J_0 this gives

$$F \simeq \left(\frac{\gamma(1+2\bar{n})}{4} + \zeta\frac{\kappa g_0^2 E^2}{\omega_m^4}\right) \bigg/ \left(\frac{\gamma}{4} + \frac{2\kappa\Delta_{\text{eff}}(r_0)}{\Delta_{\text{eff}}(r_0)^2 + \kappa^2}\zeta\frac{g_0^2 E^2}{\omega_m^3}\right), \quad (196)$$

where $\zeta \simeq 0.27$ is the numerical value of J_1^2 at the position of the limit cycle. The Fano factor is minimal at an effective detuning $\Delta_{\text{eff}}(r_0) = \kappa$ where it takes on the value

$$F \simeq \left(\frac{\gamma(1+2\bar{n})}{4} + \zeta\frac{\kappa g_0^2 E^2}{\omega_m^4}\right) \bigg/ \left(\frac{\gamma}{4} + \zeta\frac{g_0^2 E^2}{\omega_m^3}\right). \quad (197)$$

Note first that Eq. (197) implies that the Fano factor is lower bounded by the sideband resolution

$$F > \frac{\kappa}{\omega_m}, \quad (198)$$

and that this bound is achieved for sufficiently large driving field $E = \sqrt{2\kappa P_L/\hbar\omega_L}$ (laser power P_L). Furthermore Eq. (197) implies that the condition for sub-Poissonian statistics $1 > F$ is *exactly* equivalent to $\frac{g_0^2 E^2}{\omega_m^3}\left(1 - \frac{\kappa}{\omega_m}\right) > \frac{\gamma\bar{n}}{2\zeta}$. This can be interpreted as a condition for the driving power which for small κ/ω_m becomes

$$\frac{P_L}{\hbar\omega_L} > \frac{\omega_m^3}{4\zeta\kappa g_0^2}\gamma\bar{n}. \quad (199)$$

It is instructive to express this also in terms of the (thermal, linearized) cooperativity parameter

$$\mathcal{C} = \frac{4 g_0^2 \alpha^2}{\kappa\gamma(2\bar{n}+1)} = \frac{8 g_0^2}{\omega_m^2\gamma(2\bar{n}+1)}\frac{P_L}{\hbar\omega_L}, \quad (200)$$

where we used that the relevant average intracavity amplitude at the optomechanical limit cycles is $\alpha = \alpha_1 \simeq E/\omega_\text{m}$, cf. Eq. (130). Condition (199) then takes the form (in the limit $\bar{n} \gg 1$)

$$\mathcal{C} > \frac{1}{\zeta}\frac{\omega_m}{\kappa}. \quad (201)$$

Note that this is essentially a requirement on the *linearized* optomechanical coupling ($g \propto g_0 E$), and not on the coupling per single photon g_0. The condition in Eqs. (199) and (201), and the lower bound in Eq. (198) are the main result regarding sub-Poissonian phonon statistics.

The possibility of a sub-Poissonian number distribution was discussed in [66, 67] for the resonance at the first (and higher) blue sidebands. The prediction of the analytical model is especially good for the regime with small g_0 that results in larger limit cycle amplitudes. In Figure 11, which compares the Fano factors as derived from our analytical model and from solving the master equation, the good agreement can be seen. For larger g_0 (not depicted in Figure 11) the condition necessary for adiabatic elimination is less satisfied and also the linear approximation (195) gets worse, because $\Delta n \approx \langle n \rangle$. Thus the quantitative agreement gets worse. Still the resonances for F at $\Delta \approx 0, \omega_m$ are qualitatively reproduced.

In [66, 67] the Fano Factor has been calculated with a derivation using the truncated Wigner function approximation and solving the resulting Langevin equation. If we use the Wigner function as the phase space distribution, our calculation, which does not rely on this truncation, gives the same result in the regime where the Kerr parameter K is negligible.

For limit cycles with the cavity close to its ground state, different approaches to treat the Kerr effect have been taken in the literature: [69] uses the classical part of the Kerr effect, as derived with the standard master equation approach, to introduce a renormalized detuning with a shift proportional to the cavity occupation. An additional constant (independent of the cavity occupation) shift of the detuning by $K = g_0^2/\omega_m$, was numerically observed in [67] and then introduced by hand, to match the numerical data. It is one of the main results of the semi-polaron approach, that the separate Kerr term for the cavity is naturally derived for limit cycles. It causes exactly the additional quantum shift of Δ observed in [67], which is most striking in the $|\alpha| \ll 1$ limit, cf. Eq. (141).

4.5 NONPOSITIVE WIGNER FUNCTION

Finally we use the Fano factor to predict the occurrence of a negative area in the Wigner function. For a Fock state the Fano factor $F = \Delta n^2/\langle n \rangle$ is of course zero and, except for the vacuum, all Fock states have a pronounced negativity of the Wigner function. Both F and the Wigner function are continuous functions of the state ρ. Hence, for a given mean phonon number n_0 there is a critical value F_c, such that for a state with $F < F_c$ the Wigner function has a negative area. For a simple set of Ansatz states given by a density matrix diagonal in Fock basis with Gaussian probability distribution

$$P(n) \propto \exp\left(-\frac{(n-n_0)^2}{V}\right), \tag{202}$$

we numerically determined the corresponding critical Fano factor F_c. The result is illustrated in Fig. 12. We use this particular Ansatz, because the typical steady state density matrix of our problem is approximately of this form when g_0/ω_m is not too large. In [67] the steady state as a Gaussian distribution in Fock states is derived in more detail.

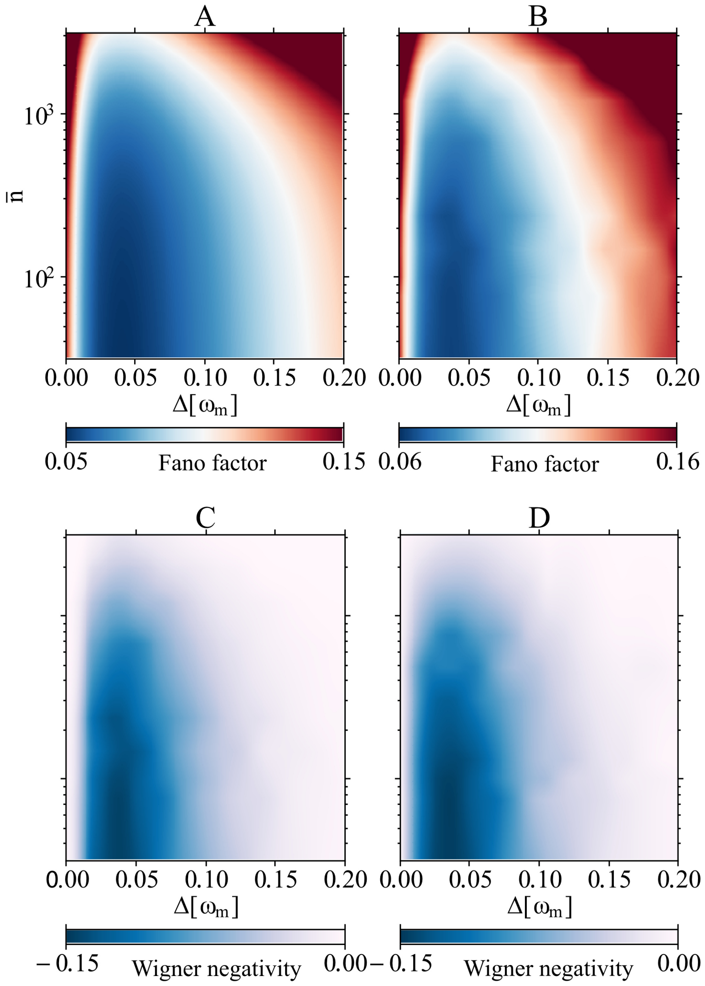

Figure 11: Plots A) and B) show the Fano factor F versus (bare) detuning Δ and bath occupation number $\bar{n}$. Note that by varying $\bar{n}$, we automatically vary the crucial quantity $\gamma\bar{n}$ appearing in equations (196) and (197). Plot A) is a plot of the simple analytical expression (196). Plot B) shows the numerical result obtained with Monte-Carlo trajectories for 30000 mechanical oscillations. A) and B) are in good agreement despite the fact that in the parameter regime considered here some of the approximations are barely fulfilled. Note that the color scale in the numerical prediction for the Fano factor is slightly shifted up by 0.01, hinting possibly at some additional diffusion process not considered in the analytical model. Plot C) shows the prediction for Wigner function negativity (defined as the quotient of the most negative and the most positive value of W) obtained by extrapolating the results for F from plot B) using the function from Fig. 12. Plot D) shows the Wigner function negativity as directly extracted from the numerical result of the Wigner function. The fixed parameters in all plots are $(g_0, \kappa_E = 2\kappa, \gamma_E = 2\gamma, E) = (0.05, 0.1, 10^{-7}, 1.56) \times \omega_m$. The approximate average number of photons in the cavity is 1.5 in these plots.

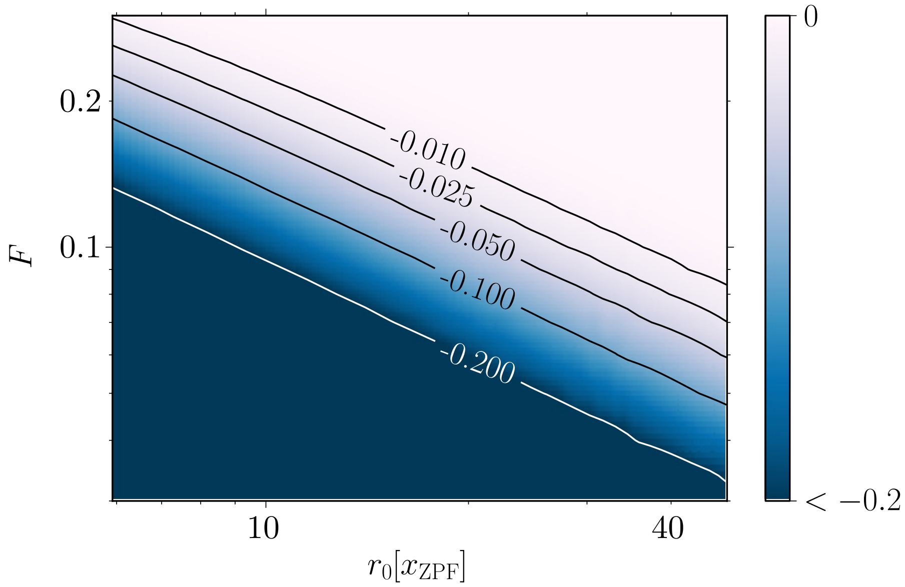

Figure 12: Maximal negativity of the Wigner function (defined as the quotient of the most negative and the most positive value of W) as a function of the Fano factor F and the mean amplitude r_0 for a phonon distribution as in equation (202). From this plot one can read of, how small the Fano factor needs to be for a given r_0, to see a negative value in the Wigner function. Implicitly this is also a requirement on g_0 because $r_0 \propto \frac{\omega_m}{g_0}$, see Section 4.3.

Figure 12 shows that this threshold F_c is smaller for larger amplitude r_0. We infer that in order to see negativity of the Wigner function in steady state, small limit cycle amplitudes with small Fano factors are favorable. Applied to the results of [68, 69] this explains the more favorable condition for negativity at the $\Delta \simeq 0$-resonance as compared to the $\Delta \simeq \omega_m$-resonance, because the limit cycle there has a smaller amplitude (given by the first root of $J_0(\eta r)$ as compared to $J_1(\eta r)$, as discussed in Section 4.3). Independently of Δ, the amplitude scales with the inverse of g_0/ω_m, such that for a large ratio g_0/ω_m a non-positive Wigner function is achieved already for larger Fano factors. More precisely, we can conclude from Fig. 12 that

$$F_c \simeq \xi r_0^{-s}, \qquad s \simeq 0.6, \tag{203}$$

where the constant ξ depends on how negative the Wigner function should be. In order to achieve a ratio of minimal to maximal value of the Wigner function of e.g. -0.1 this constant is found to be $\xi \simeq 0.6$. As a comparison, this negativity ratio can reach (approximately) -2.5 for odd Fock states and -0.4 for even Fock states.

Since the amplitude of the first limit cycle is $r_0 \simeq \omega_\mathrm{m}/g_0$ the condition $F < F_c$, together with Eqs. (197) and (203), is equivalent to ($\zeta \simeq 0.27$)

$$\frac{g_0^2 E^2}{\omega_m^3}\left[\xi\left(\frac{g_0}{\omega_m}\right)^s - \frac{\kappa}{\omega_m}\right] > \frac{\gamma(2\bar{n}+1)}{4\zeta} - \frac{\xi\gamma}{4\zeta}\left(\frac{g_0}{\omega_m}\right)^s . \tag{204}$$

Thus, one necessary condition for negative Wigner function is that the square bracket on the left side is positive. This is a condition on the single photon optomechanical coupling g_0, that can be written equivalently as both

$$\frac{g_0}{\omega_m} > \left(\frac{\kappa}{\xi\omega_m}\right)^{1/s}, \qquad \frac{g_0}{\kappa} > \frac{1}{\xi^{1/s}}\left(\frac{\kappa}{\omega_m}\right)^{(1-s)/s} . \tag{205}$$

Note that this condition for the occurrence of a quantum state is *weaker* than the condition $g_0/\kappa > 1$ which had been expected before.

Assuming this condition to be well fulfilled we can drop the second terms on both left and right hand side of (204) and get the power requirement

$$\frac{P_L}{\hbar\omega_L} > \frac{\omega_\mathrm{m}^3}{4\xi\zeta\kappa g_0^2}\left(\frac{\omega_m}{g_0}\right)^s \gamma\left(\bar{n}+\tfrac{1}{2}\right) \tag{206}$$

Note that this is stronger than the requirement (199) for sub-Poissonian statistics, as one would expect. In terms of the cooperativity (for any $\bar{n}$) this becomes

$$\mathcal{C} > \frac{1}{\xi\zeta}\left(\frac{\omega_m}{g_0}\right)^s . \tag{207}$$

Note also that even for zero temperature, $\bar{n} \to 0$, there is now a threshold for the power (cooperativity) in contrast to the condition for sub-Poissonian statistics. Condition (205) on the strength of the optomechanical coupling per single photon, and condition (206) (or (207)) are the main results regarding negative Wigner functions. We again stress that negative mechanical Wigner density is possible even outside the single-photon strong-coupling regime, i.e. for paramters $g_0 < \kappa$.

4.6 NUMERICAL ANALYSIS

In this section we compare the predictions from the sections above with the numerical result for the master equation of Eq. (106). To do the calculation for large Hilbert space dimension, we applied the Monte-Carlo wave function method [91, 92, 93] described in Section 2.C.1 as implemented in QuTiP [32, 33], the quantum toolbox for python. The advantage is that one needs to simulate only wave functions and not density matrices, so that the Hilbert space dimension required for the simulation scales only with the number of possible pure states N instead of N^2. In this method the individual trajectory of an initially pure state is calculated, conditioned on the history of fictive photon and phonon counters measuring the particles leaking out of the system. With this knowledge of the environment an initially pure state stays pure. The density matrix is then retrieved by averaging over a large ensemble of such conditional states. The ensemble average can be replaced by the time average for calculating a steady state density matrix.

Our implementation was done with an adaptive Hilbert space, where the Fock states are not only limited from above, but also from below and after each mechanical oscillation the Hilbert space is updated so that it is centered around the current state. To make sure that not too much of the Hilbert space is truncated, the number of states to be used is scaled with the standard deviation in energy of the state in the previous step. This flexibility of the Hilbert space during the calculation allows to run the simulation without much a priori knowledge of the steady state and even fewer basis states are required.

The solution is obtained in the following steps: For speed up of the calculation, the initial state is chosen to be a coherent state with an amplitude close to the expected steady state. It is then evolved for some period until at a time t_0 the conditional state's amplitude and Fano factor stop to drift and only fluctuate. We then make use of the fact, that in steady state the time average corresponds to the ensemble average, and calculate the steady state of the oscillator as

$$\rho_M = \int_{t_0}^{t_0+T} \mathrm{tr}_c \left(|\psi_t\rangle\langle\psi_t| \right) \mathrm{d}t, \tag{208}$$

where $|\psi_t\rangle$ is the conditional state at time t, and T spans many mechanical oscillations.

This procedure is performed many times in parallel on a cluster and the resulting matrices ρ_M are averaged. The deviation of the individual ρ_M provides an error estimate for the method. As a further benchmark and control, we also calculated the steady state with the biconjugate gradient steady-state solver from scipy [94], which is however limited to a comparably small Hilbert space dimension.

The algorithm described above allows for the first time to numerically study optomechanical limit cycles in the experimentally relevant regime of large amplitudes of the mechanical oscillator (as caused by a relatively small g_0/ω_m) and with more than only a few photons in the cavity. In previous studies the question was posed whether the analytical theory can be applied to this regime [67] and if the nonclassical features survive [69] for more than one photon in the cavity. We answer this question affirmative: Fig. 13 shows an example of a Wigner function in this regime with small Fano factor and some negative density.

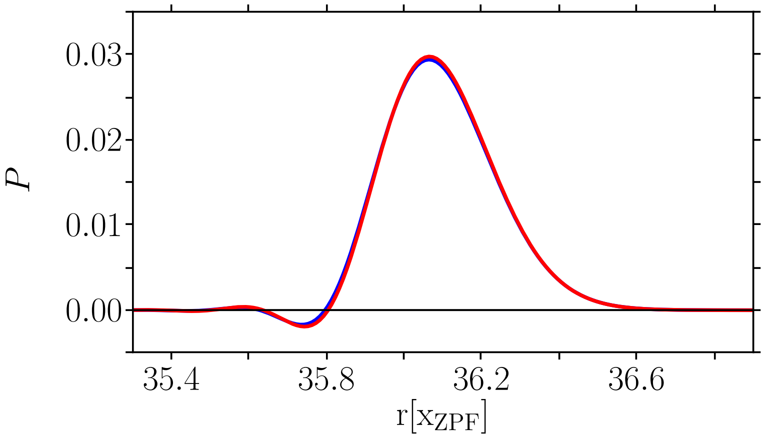

Figure 13: Radial part of a Wigner function for parameters with high amplitude and many photons ($\langle a^\dagger a \rangle \approx 8$) in the cavity featuring a very small Fano factor ($F = 0.07$) and some negative density. The parameters are $(g_0, \kappa_E = 2\kappa, \gamma, E, \Delta) = (0.033, 0.1, 0., 3.5, 0.03) \times \omega_m$. The blue and red line are the result of two independent runs (each averaging 5000 mechanical oscillations) of the Monte-Carlo based steady state solver.

Strictly speaking the steady state calculated here is only metastable if γ is so small that there is more than one attractor for the limit cycle, cf. Fig. 7. The timescale for switching between different attractors is much longer than the time to relax in a given metastable steady state. Thus it is not considered in this thesis. In order to choose the metastable attractor for the numerical simulation, we choose an initial state in the vicinity of our preferred attractor, in this case the limit cycle with lowest possible amplitude. Also in the analytical expressions for the Fano factor, we always treat possibly metastable states as steady states. For very large g_0/ω_m different metastable attractors start to merge and the analysis becomes more involved. This merging of attractors and its effect on nonclassical features was studied in detail by [69].

4.7 CONCLUSIONS

In this chapter we studied quantum limit cycles of the standard optomechanical system tuned near resonance and found the simple analytical expression (196), that predicts the possibility of very small values for the Fano factor F of the mechanical oscillator. We found that in the sideband resolved regime a large value of $g_0^2 E^2 / \omega_m^3 \gamma \bar{n}$, i.e. a large *linearized* optomechanical coupling, is required to minimize F.

We found that it is possible to create a negative mechanical Wigner function in steady state even outside the single-photon strong-coupling regime. (i.e. for parameters $g_0 < \kappa$.) Particularly, we established a relation between sub-Poissonian phonon statistics and negativity of the Wigner density for typical parameters of limit cycles: The oscillator's steady state has an approximately Gaussian number distribution at each metastable limit cycle. For these states the requirement on F to see negativity of the Wigner function is given by the function plotted in Figure 12.

Using a Monte-Carlo method with an adaptive Hilbert space, we numerically checked this scaling even for limit cycles with very large amplitude and many photons in the cavity, where an ordinary steady state solver cannot be applied. The numerical simulation depicted in Figure 11 show that indeed the criterion of a small Fano factor can predict the negativity of the Wigner function. For currently more feasible experimental parameters with even smaller g_0/ω_m, the negativity disappears according to Fig. 12, but the very small Fano factors remain.

5

SUB-POISSONIAN PHONON LASING IN THREE-MODE OPTOMECHANICS

5.1 INTRODUCTION

As discussed in the previous chapter 4, theoretical work suggests that for optomechanical limit cycles in the standard optomechanical setup (with one mechanical and one optical mode) it is possible to prepare a state with quantum signatures in the phonon statistics such as phonon antibunching and even negative Wigner density [66, 67, 68, 69, 1, 95]. Notably, this is possible even for parameters outside the single-photon strong-coupling regime. In such setups the laser must be operated at a detuning from the cavity resonance on the order of the mechanical resonance frequency ω_m in order to excite limit cycles at all. Therefore all relevant processes are suppressed by a factor $1/\omega_m$, which is reflected in the scaling of the optomechanical nonlinearity with g_0/ω_m (cf. Figure 7 from chapter 4), as well as the unfavorably scaling of the requirements for sub-Poissonian statistics with ω_m (cf. equation (201) from chapter 4). On the other hand, a large value of ω_m is desireable to have a low occupation number of the phononic bath and to stay in the sideband resolved regime.

In this chapter we propose to make use of the enhanced optomechanical nonlinearity [96, 97, 98] of a setup with a second optical mode directly supporting the laser frequency to overcome the unfavorable $1/\omega_m$ scaling and prepare phonon laser states featuring antibunching in steady state with state of the art optomechanical crystals.

The enhanced nonlinearity has been discussed in the context of detectors for phonons or photons [97], quantum memories [99], and to improve [98] the parameters of mechanically induced photon antibunching [73, 74]. In the context of the phonon laser transition the enhanced optomechanical instability with two optical modes has been anticipated as a possible complication for gravitational wave detectors [100], and has been studied experimentally [23, 24, 25, 26, 27, 101] and theoretically [102, 103, 104, 105, 106, 107] in the classical regime. Here we show for the first time that one can detect quantum signatures in the phonon lasing of such a three-mode system. In particular antibunched statistics of the phonon number ($\hat{n} = c^\dagger c$), as commonly characterized by a Fano factor $F = \langle \Delta \hat{n}^2 \rangle / \langle \hat{n} \rangle < 1$, and a second order coherence function $g^{(2)}(t)$ at time $t = 0$,

$$g^{(2)}(0) = \langle c^\dagger c^\dagger c c \rangle / \langle \hat{n} \rangle^2 = 1 + (F - 1)/\langle \hat{n} \rangle < 1, \qquad (209)$$

can be prepared in steady state. With more demanding system requirements, even a negative mechanical Wigner density can be achieved.

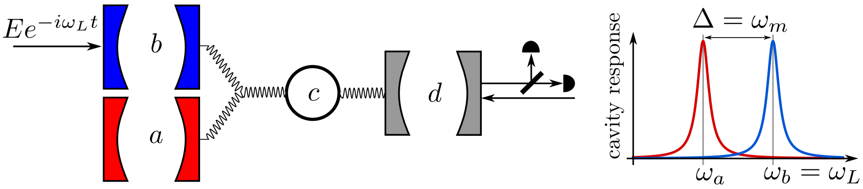

Figure 14: left: Two optical modes a and b are coupled to a mechanical mode c. The b-mode is resonantly driven by a laser of strength E and frequency $\omega_L = \omega_b$. The a-mode is detuned from b by $\Delta = \omega_m$, the mechanical resonance frequency, as depicted in the plot on the right. The nonlinear interaction of the three modes a, b, and c gives rise to optomechanical limit cycles with strongly sub-Poissonian phonon number statistics. A third optical mode d can be used to reduce the effective temperature of the mechanical oscillator's bath and to read out the phonon statistics in a Hanburry-Brown-Twiss measurement.

5.2 SYSTEM DESCRIPTION

We study the optomechanical setup depicted in Fig. 14. Two optical modes a and b couple to a mechanical mode c via the three-mode interaction Hamiltonian $V = g_0(ab^\dagger + a^\dagger b)(c + c^\dagger)$,where g_0 is the single photon optomechanical coupling strength and a, b, c are the lowering operators of the different modes. Such an interaction has been implemented in Refs. [23, 24, 25, 26, 27, 101]. The optical mode b is resonantly driven with a laser of power P , which we parametrize with $E = \sqrt{\kappa P/\hbar\omega_b}$ (κ is the cavity line width, and ω_b the resonance frequency of mode b). The other optical mode a is detuned with respect to cavity mode b and the driving laser by Δ, and the mechanical frequency is ω_m, so that the Hamiltonian in a rotating frame for both cavities with frequency ω_b is $H = H_0 + V + iE(b^\dagger - b)$ with $H_0 = \omega_m c^\dagger c - \Delta a^\dagger a$.

Depending on the sign of the laser detuning, the laser either cools the mechanical mode ($\Delta < 0$) , or gives rise to self-induced mechanical oscillations ($\Delta > 0$). In the latter regime the intrinsic nonlinearity of the three-mode optomechanical interaction V stabilizes the mechanical oscillation at a finite amplitude [101]. We choose a detuning $\Delta = \omega_m$ between the two cavities which corresponds to a resonant excitation of optomechanical limit cycles. In an interaction picture with respect to H_0 the Hamiltonian is

$$H_I = iE(b^\dagger - b) + g_0(ab^\dagger c + a^\dagger bc^\dagger). \tag{210}$$

We neglected here fast oscillating terms $e^{2i\omega_m t} g_0 ab^\dagger c^\dagger + h.c.$, assuming a cavity decay rate of $\kappa \ll \omega_m$ for both cavities (the corrections are of order κ^2/ω_m^2, i.e. negligible for typical optomechanical crystals.).

In the framework of Langevin equations the system dynamics is then described by

$$\dot{a} = -ig_0 bc^{\dagger} - \tfrac{\kappa}{2}a + \sqrt{\kappa}a_{in}, \quad \dot{b} = -ig_0 ac - \tfrac{\kappa}{2}b + E + \sqrt{\kappa}b_{in}, \tag{211}$$

$$\dot{c} = -ig_0 a^{\dagger}b - \tfrac{\gamma}{2}c + \sqrt{\gamma}c_{in}, \tag{212}$$

where $\langle a_{in}(t)a_{in}^{\dagger}(t')\rangle = \langle b_{in}(t)b_{in}^{\dagger}(t')\rangle = \delta(t-t')$ and $\langle c_{in}(t)c_{in}^{\dagger}(t')\rangle = (1+\bar{n})\delta(t-t')$ are the two-time correlation functions of the Langevin noise forces. We assumed energy decay of the mechanical oscillator at rate γ, due to coupling to a thermal thermal bath with mean occupation $\bar{n}$. We adopt the convention from the review [14] that κ and γ are energy decay rates. Correspondingly, amplitudes decay at $\kappa/2$ and $\gamma/2$.

5.3 CALCULATION OF CLASSICAL AMPLITUDES

We express each operator as a sum of a classical ($\mathbb{C}$-number) component and an operator describing fluctuations around it, such that $a = \alpha + \delta a$, $b = \beta + \delta b$ and $c = \zeta + \delta c$. Inserting this into the Langevin equations, and considering the $\mathbb{C}$-number components only, gives rise to a coupled set of nonlinear equations for the classical cavity amplitudes α and β, and the (complex) mechanical amplitude ζ. In particular one finds

$$\dot{\alpha} = -ig_0\beta\zeta^* - \tfrac{\kappa}{2}\alpha, \qquad \dot{\beta} = -ig_0\alpha\zeta - \tfrac{\kappa}{2}\beta + E. \tag{213}$$

We assume that the optical amplitudes adiabatically follow the motion of the mechanical oscillator which is equivalent to the conditions $(\bar{n}+1)\gamma, g_0|\alpha|, g_0|\beta| \ll \kappa$. Solving $\dot{\alpha} = \dot{\beta} = 0$ results in the adiabatic solution for the optical amplitudes

$$\beta(\zeta,\zeta^*) = \frac{E\kappa}{2h_\zeta}, \qquad \alpha(\zeta,\zeta^*) = -i\frac{Eg_0\zeta^*}{h_\zeta}, \tag{214}$$

where $h_\zeta = g_0^2|\zeta|^2 + \frac{1}{4}\kappa^2$. Inserting these optical amplitudes in the equation of motion for the classical mechanical amplitude results in $\dot{\zeta} = -\frac{1}{2}(\gamma + \gamma_{\text{opt}})\zeta$, where the optically mediated (anti)damping is

$$\gamma_{\text{opt}}(\zeta) = -\frac{g_0^2E^2\kappa}{h_\zeta^2}, \tag{215}$$

cf. Fig. 15a. γ_{opt} is negative for all mechanical amplitudes and its absolute value decreases with increasing amplitude ζ according to the Lorentzian given by h_ζ^2, approaching 0 for $\zeta \gg \kappa/g_0$. In agreement with [101] we define the dimensionless parameter $\mathcal{R} = |\gamma_{\text{opt}}(0)|/\gamma = 16g_0^2E^2/\kappa^3\gamma$, which corresponds to the gain of mechanical amplification at zero mechanical amplitude. For $\mathcal{R} < 1$ the total mechanical damping $\gamma + \gamma_{\text{opt}}(0) > 0$ is positive for all amplitudes, implying

$\zeta = 0$ in steady state. Above threshold, $\mathcal{R} > 1$, the steady state ($\dot{\zeta} = 0$) is achieved for a mechanical amplitude ζ_0 such that $\gamma_{\text{opt}}(\zeta_0) = -\gamma$, cf. Fig. 15a. The solution of this nonlinear equation is

$$|\zeta_0|^2 = \left(\frac{\kappa}{2g_0}\right)^2 \left(\sqrt{\mathcal{R}} - 1\right). \tag{216}$$

The solution is unique (up to the oscillator's phase, where we choose $\zeta_0 = |\zeta_0|$, without loss of generality) and fully determined by the gain parameter $\mathcal{R}$ and the single-photon strong-coupling parameter $2g_0/\kappa$. It is instructive to contrast this result with the equivalent one for a conventional two-mode (one mechanical and one optical mode) optomechanical system where the mean phonon number of self-induced limit cycles scales as the inverse of the much smaller ratio $(g_0/\omega_m)^2$ instead, cf. equation (190) and following from Chapter 4, as well as Figure 7 from the same chapter. In view of Eq. (209) it is clear that a small oscillation amplitude is advantageous in order to observe strong antibunching and that the three mode setup improves the signal approximately by a factor of $4(\omega_m/\kappa)^2$. This can be two orders of magnitude for typical system parameters of optomechanical crystals, e.g. $4(\omega_m/\kappa)^2 = 217$ with $\kappa/2\pi = 500\text{MHz}$ and $\omega_m/2\pi = 3.68\text{GHz}$ from [16].

5.4 CALCULATION OF QUANTUM AMPLITUDE NOISE

The fluctuations δa, δb, and δc with respect to these classical amplitudes fulfill the linearized Langevin equations

$$\delta\dot{a} = \left(-\tfrac{\kappa}{2}\delta a - ig_0\zeta_0\delta b\right) - ig_0\beta_0\delta c^\dagger + \sqrt{\kappa}a_{in}, \tag{217}$$

$$\delta\dot{b} = \left(-\tfrac{\kappa}{2}\delta b - ig_0\zeta_0\delta a\right) - ig_0\alpha_0\delta c + \sqrt{\kappa}b_{in}, \tag{218}$$

$$\delta\dot{c} = -\tfrac{\gamma}{2}\delta c - ig_0(\alpha_0^*\delta b + \beta_0\delta a^\dagger) + \sqrt{\gamma}c_{in}, \tag{219}$$

where we consistently dropped all terms of quadratic order in the fluctuations. This approximation is only valid for large enough amplitudes. We also introduce here the shorthand notation $(\alpha_0, \beta_0) = (\alpha(\zeta_0), \beta(\zeta_0))$ for the cavity amplitudes in the developed mechanical limit cycle. The quantum fluctuations of the cavity modes can now be treated in analogy to the classical amplitudes simply by setting $\delta\dot{a} = \delta\dot{b} = 0$ and solving the resulting algebraic equation. Inserting the solutions for δa and δb back into Eq. (219) gives the dynamics for the mechanical mode δc. For the canonical mechanical quadratures $X = \left(\delta c + \delta c^\dagger\right) / \sqrt{2}$ and $Y = \left(\delta c - \delta c^\dagger\right) / \sqrt{2}i$, cf. Fig. 15 c), we get effective Langevin equations

$$\dot{X} = -\tfrac{1}{2}\Gamma X + \sqrt{D}X_N, \qquad \dot{Y} = \sqrt{D}Y_N, \tag{220}$$

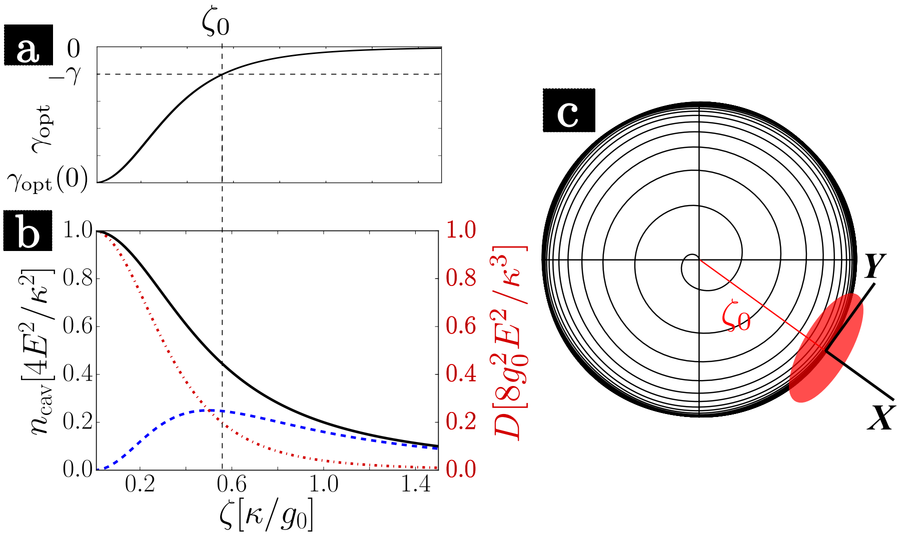

Figure 15: (a) Optically mediated (anti)damping $\gamma_{\mathrm{opt}}(\zeta)$ (bold line) as a function of mechanical amplitude ζ according to equation (215). The steady state ζ_0 is reached when $\gamma_{\mathrm{opt}}(\zeta_0) = -\gamma$ (dashed line). (b) Intra cavity photon number $|\alpha|^2$ in mode a (blue dashed line), $|\beta|^2$ in mode b (red dash-dotted line) and total photon number $n_{\mathrm{cav}} = |\alpha|^2 + |\beta|^2$ (black solid line) is plotted as a function of mechanical amplitude ζ according to equation (214). The optically induced diffusion $D_{\mathrm{opt}} = g_0^2 \frac{\kappa}{2}(|\alpha|^2 + |\beta|^2)/h_\zeta$ of the mechanical oscillator scales exactly like the red dash-dotted line with a scale as given on the right y-axis. (c) Schematic phase space trajectory of the mechanical oscillator approaching the limit cycle attractor with amplitude ζ_0. In the co-rotating frame of the oscillator the X quadrature relates to its amplitude and the Y quadrature to its phase.

with damping Γ, diffusion D and noise forces with two-time correlators $\langle X_N(t), X_N(t')\rangle = \delta(t-t')$ and $\langle Y_N(t), Y_N(t')\rangle = \delta(t-t')$. Both damping

$$\Gamma = \gamma + \Gamma_{\mathrm{opt}}(\zeta) \tag{221}$$

and diffusion

$$D = \gamma(\tfrac{1}{2} + \bar{n}) + D_{\mathrm{opt}}(\zeta) \tag{222}$$

have an intrinsic mechanical constant contribution and an optically mediated nonlinear (ζ-dependent) contribution. We find that $D_{\mathrm{opt}}(\zeta) = g_0^2 \frac{\kappa}{2}(|\alpha|^2 + |\beta|^2)/h_\zeta$ at the point of the limit cycle is exactly as large as the vacuum contribution of the mechanical bath, i.e. $D_{\mathrm{opt}}(\zeta_0) = \frac{\gamma}{2}$, but $\Gamma_{\mathrm{opt}}(\zeta_0) = \gamma(3 - 4/\sqrt{\mathcal{R}})$ can grow up to three times the mechanical damping for large $\mathcal{R}$. In total the damping and diffusion depicted in Fig. 15 a) and b) are at the limit cycle

$$\Gamma(\zeta_0) = 4\gamma(1 - 1/\sqrt{\mathcal{R}}), \qquad D(\zeta_0) = \gamma(\bar{n} + 1). \tag{223}$$

As schematically depicted in Fig. 15 c), in our convention the Y-quadrature relates to the phase of the mechanical oscillator, which is subjected to undamped diffusion, cf. Eq. (220). The X-quadrature relates to the mechanical amplitude, which is our focus of interest. In particular for the phonon occupation number $\hat{n} = c^\dagger c$ one finds $\langle \hat{n} \rangle = \zeta^2 + \mathcal{O}(\zeta^0)$ and $\langle \hat{n}^2 \rangle = \zeta^4 + 2\zeta^2 \langle X^2 \rangle + \mathcal{O}(\zeta^0)$, such that the Fano factor is $F \simeq 2\langle X^2 \rangle$. Eq. (220) gives $\langle X^2 \rangle = D/\Gamma$ in steady state, i.e. the amplitude variance is determined by the compromise of diffusion and effective damping, yielding for the Fano factor

$$F = \frac{1}{2} \frac{1+\bar{n}}{1 - 1/\sqrt{\mathcal{R}}}. \tag{224}$$

This is in excellent agreement with numerical results shown in Figure 17 a) that were obtained by Monte-Carlo simulation (see Appendix 5.A) of a master equation equivalent to the exact, nonlinear equations of motion in Eqs. (211) to (212).

From Eq. (224) we see that for $\mathcal{R} \gg 1$ the Fano factor approaches $(1+\bar{n})/2$. Therefore, we arrive at the condition $\bar{n} < 1$ necessary in order to observe sub-Poissonian phonon statistics. For a cryogenically cooled mechanical oscillator $\bar{n} = 1/(e^{\hbar\omega_m/k_B T} - 1) < 1$ can in principle be achieved for a sufficiently high resonance frequency and at low temperature T, see [108, 109]. However, in the present case it is possible to take advantage of laser cooling of the mechanical oscillator [75, 110] in order to observe sub-Poissonian statistics.

5.5 ADDITIONAL LASER COOLING

Consider a setup where the mechanical oscillator is coupled to a third optical cavity of line width κ_d which is driven below resonance such as to induce an additional damping γ_L of the oscillator. Eliminating this cooling cavity gives rise to a 'dressed' mechanical oscillator whose equation of motion is still given by (212) with an effective mechanical damping and occupation number

$$\gamma = \gamma_0 + \gamma_L, \qquad \bar{n} = \frac{\gamma_0 \bar{n}_0 + \gamma_L \bar{n}_L}{\gamma_0 + \gamma_L}, \tag{225}$$

cf. equation (36) and following from Section 2.1.5. Here γ_0 is the line width and $\bar{n}_0$ the occupation number of the bare mechanical resonance (without laser cooling), and $\bar{n}_L = (\kappa_d/4\omega_m)^2$ is the quantum limit of optomechanical laser cooling [75, 110].

In order to have $F < 1$ we assume laser cooling to an effective phonon occupation $\bar{n} < 1$. This comes at the cost of a decreased gain parameter $\mathcal{R} = 16 g_0^2 E^2/\kappa^3(\gamma_0 + \gamma_L)$, which can be compensated for by a somewhat more intense driving field. It is rather remarkable that laser cooling can help to observe a quantum feature such as sub-Poissonian phonon statistics: While laser cooling can provide a small

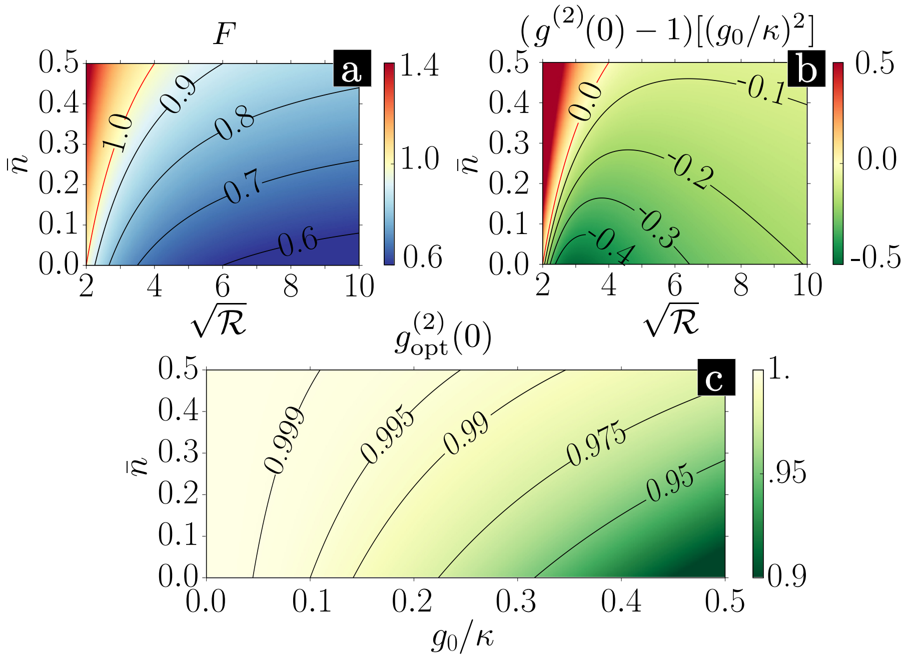

Figure 16: (a) Fano factor as a function of effective mechanical bath occupation number $\bar{n}$ and total number of photons in the cavity $n_{\rm ph}[\kappa\gamma/4g_0^2] = \sqrt{\mathcal{R}}$ according to Eq. (224). (b) Plot of $(g^{(2)}(0)-1)[(g_0/\kappa)^2]$ as a function of the same parameters in units of the squared single-photon strong-coupling parameter $(g_0/\kappa)^2$ according to Eqs. (226) and (227). The condition for both sub-Poissonian statistics ($F<1$) and antibunching ($g^{(2)}(0)<1$) is visualized by the red contour line $\bar{n} = 1-2/\sqrt{\mathcal{R}}$ in both plots. (c) Plot of $g^{(2)}_{\rm opt}(0)$ for optimal choice of $\mathcal{R}$ as a function of g_0/κ and $\bar{n}$ according to Eq. (228).

effective occupation number $\bar{n} \ll \bar{n}_0$ it does so by increasing the effective mechanical line width $\gamma \gg \gamma_0$ by the same factor. As a result, the decoherence rate relevant for quantum effects, $\gamma_0\bar{n}_0 = \gamma\bar{n}$, stays constant, such that laser cooling in most cases does not help in order to achieve quantum effects with mechanical oscillators.

5.6 EXPERIMENTAL FEASIBILITY

The requirements on the system parameters to have $g^{(2)}(0) < 1$ (and therefore $F < 1$) is found by inserting the mean amplitude (216) and the Fano factor (224) in the definition (209) of $g^{(2)}(0)$,

$$g^{(2)}(0) - 1 = 4\left(\frac{g_0}{\kappa}\right)^2 \frac{F-1}{\sqrt{\mathcal{R}}-1}. \tag{226}$$

For the discussion of experimental feasibility it is more instructive to express the gain parameter $\mathcal{R}$ in terms of the steady state total number of photons in the cavity $n_{\rm ph} = |\alpha_0|^2 + |\beta_0|^2 = \frac{\kappa\gamma}{4g_0^2}\sqrt{\mathcal{R}}$, where we used Eqs. (216) and (214). The circulating number of photons is important as it determines the heating of the mechanical structure, which was the limiting decoherence mechanism in recent experiments with optomechanical crystals [16]. In Fig. 16 (a) and (b) we show the Fano factor F and $g^{(2)}(0) - 1$ (in units of g_0^2/κ^2) as a function of the number of photons in the cavity $n_{\rm ph}$ and the effective mechanical bath occupation number $\bar{n}$. In view of the dependence of the Fano factor and the second order coherence function on $\mathcal{R}$, cf. Eqs. (224) and (226) respectively, it is clear that there is an optimal number of circulating photons minimizing $g^{(2)}(0)$ for given $\bar{n}$ and single photon strong coupling parameter g_0/κ. The minimum is reached at

$$n_{\rm ph}\left[\kappa\gamma/4g_0^2\right] = (3+\bar{n})/(1-\bar{n}) \tag{227}$$

and is given by

$$g^{(2)}_{\rm opt}(0) = 1 - \tfrac{1}{2}\left(\frac{g_0}{\kappa}\right)^2 \frac{(1-\bar{n})^2}{(1+\bar{n})}, \tag{228}$$

which is illustrated in Fig. 16c. Thus, a large single-photon coupling helps, but is not strictly required, to create a robust signal to verify antibunching. We conclude that a sub-Poissonian phonon laser state can be prepared and verified outside the single-photon strong-coupling regime and for small but finite effective (cf. Eq. (225)) bath occupation $\bar{n}$ by detecting photon antibunching in the reflected light. We emphasize that phonon antibunching can be observed already in a regime of few circulating photons $n_{\rm ph} \ll 1$.

5.7 READOUT OF PHONON STATISTICS

The readout of the – possibly antibunched – phonon statistics can be implemented in analogy to [30] using the cooling laser mode d. In the sideband resolved ($\kappa_d \ll \omega_m$) and linear ($g_d\zeta \ll \omega_m$) regime the dynamics of laser cooling can be understood as a continuous coherent state swap interaction $cd^\dagger + c^\dagger d$ [17, 18]. The phonon statistics of d can then be measured by counting the photons in the output of the cooling cavity d at the sideband frequency $+\omega_m$ [30]. Hence with this readout scheme phonon antibunching is detected via photon antibunching.

Note that detection losses of an experiment do not alter the measured second order coherence function, as both its numerator $\langle c^\dagger c^\dagger cc\rangle$ and denominator $\langle\hat{n}\rangle^2$ scale with the detection efficiency squared. Additional noise counts however, mostly caused by dark counts from the detector and carrier photons leaking through the frequency filter, will bring $g^{(2)}(0)$ closer to one. In [30] the noise equivalent-phonon number $n_{\rm NEP}$, defined as the ratio of noise counts and sideband counts per phonon, was limited by $n_{\rm NEP} = 0.89$. Using an additional filter to decrease the carrier bleed through, the authors of [30] even expect to improve this value by a few orders of magnitude. We conclude that

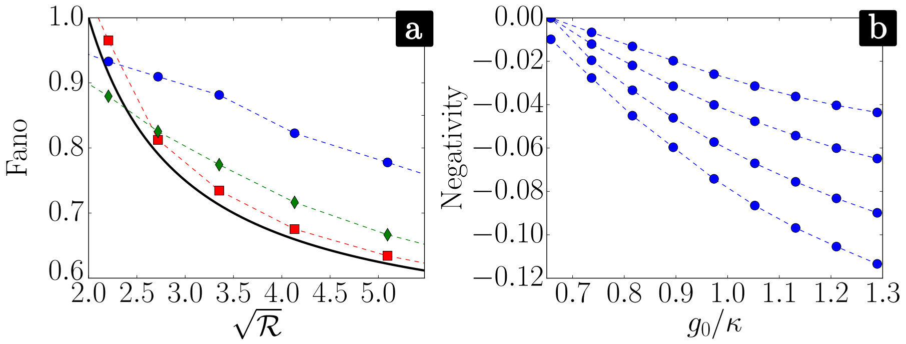

Figure 17: (a) Comparison of analytical results (black solid line) from Eq. (224) to numerical results for Fano factor F with increasing $g_0/\kappa = 0.25, 0.5, 1$. (square, diamond, circle). The parameter $g_0 E/\kappa^2 = 0.04$ is fixed to stay well inside the regime of validity of the adiabatic elimination. In this plot $\bar{n} = 0$ but for finite temperature the agreement of numerics with Eq. (224) is equally good. (b) Negativity (quotient of smallest largest value) of the mechanical oscillator's Wigner function in steady state calculated with QuTiP's steady state solver. The bath occupation is $\bar{n} = 0.25, 0.5, 1, 2$ for the increasing curves. The driving field $E = 0.07\kappa$ is constant in both plots, to stay well in the regime of $n_{\mathrm{ph}} \ll 1$ for numerical simplicity. Each point in (b) is optimized over $\mathcal{R}$ by varying γ.

a phonon statistics readout that does not significantly alter $g^{(2)}(0)$ is feasible.

Currently the highest reported value for the coupling in optomechanical crystals is $g_0/2\pi = 1.1$ MHz [111]. The lowest cavity decay rate in a photonic crystal is, to our knowledge, $\kappa = 20$MHz [112]. While the best ratio achieved in a single device is $g_0/\kappa = 0.007$ [16], combining the best values in one device would already reach $g_0/\kappa \approx 0.055$. The lowest reported effective bath occupation reached with optomechanical cooling is $\bar{n} = 0.85$ [16], using a dilution refrigerator mechanical oscillators have even been cooled down below $\bar{n} < 0.07$. Assuming a slightly more optimistic $g_0/\kappa = 0.1$, an effective environmental temperature of 200 mK and a mechanical frequency of 5GHz the deviation of $g^{(2)}_{\mathrm{opt}}(0)$ from 1 according to Eq. (228) will be 2.5 per mille. Further improvements on g_0 and κ are expected using new designs and fabrication methods, so that reaching a signal of $g^{(2)}_{\mathrm{opt}}(0) - 1$ on the order of a few per cent is a realistic prospect for the near future, cf. Fig. 16.

5.8 OUTLOOK AND CONCLUSION

Our linearized model is strictly valid only for $g_0/\kappa \ll 1$. We can however expect qualitative agreement to some extend even for larger g_0/κ. The deviation of F from equation (224) in this regime are plotted in Fig. 17a. Strongly sub-Poissonian states with small limit cycle amplitude $\langle\hat{n}\rangle$ feature a negative Wigner function [1]. As discussed above $\langle\hat{n}\rangle \sim (\kappa/g_0)^2$. It is therefore reasonable to expect negative mechanical Wigner density with g_0/κ approaching the single-photon strong-coupling regime. As depicted in Fig. 17b we confirm this numerically. All numerical calculations were done with QuTiP [32, 33], see Appendix 5.A.

Using an optomechanical setup with two optical modes brings experimental demonstration of both sub-Poissonian phonon statistics and optomechanically induced phonon and photon antibunching in reach of today's technology. For parameters approaching the single-photon strong-coupling regime the limit cycle states can even feature a negative mechanical Wigner function.

APPENDIX TO CHAPTER 5

5.A PHONON STATISTICS AND NUMERICAL ANALYSIS

The phonon statistics is commonly characterized by the Fano factor

$$F = \langle \Delta \hat{n}^2 \rangle / \langle \hat{n} \rangle, \tag{229}$$

and the second order coherence function $g^{(2)}(t)$ at time $t = 0$,

$$g^{(2)}(0) = \langle c^\dagger c^\dagger c c \rangle / \langle \hat{n} \rangle^2 = 1 + (F-1)/\langle \hat{n} \rangle, \tag{230}$$

which gives information on the temporal correlations of the phonons. ($g^{(2)}(0) > 1$ and $g^{(2)}(0) < 1$ corresponding to bunching and antibunching respectively [113].) The Fano factor F can be inferred from $g^{(2)}(0)$ through (209), and F smaller/greater than 1 also indicates sub/super-Poissonian statistics. In [30] $g^{(2)}(0) \approx 1$ was achieved, verifying the coherent nature of the mechanical oscillations in their setup. For comparison, the Poissonian statistics of a (classical) coherent state imply $F = 1$ and $g^{(2)}(0) = 1$, while a thermal state would have $g^{(2)}(0) = 2$.

Numerically we calculated the steady state of the system using QuTiP [32, 33], the Quantum Toolbox in Python. For Fig. 4b, where the mechanical amplitudes are small due to the large g_0/κ, the Hilbert space has moderate size and we used a direct steady state solver for density matrices. For Fig. 4a the Hilbert space is (in general) too large for this and we had to use Monte-Carlo trajectories [92, 91, 93] described in Section 2.C.1 for the wave function and average over many runs to obtain a density matrix. Each trajectory $|\psi_j(t)\rangle$ had a coherent state with random, independent and identically distributed Gaussian amplitudes, $\xi_j \sim \mathcal{N}(\zeta, 1)$ around the analytical steady state amplitude ζ_0 (fulfilling $|\zeta_0|^2 = \left(\frac{\kappa}{2g_0}\right)^2 \left(\sqrt{\mathcal{R}} - 1\right)$, cf. the main text) as initial state for the oscillator. Coherent states with amplitudes given by the best analytical result, $\beta_0 = \frac{E\kappa}{2h_{\zeta_0}}, \alpha_0 = -i\frac{E g_0 \zeta_0^*}{h_{\zeta_0}}$, were chosen as initial state for the optical modes. The system was then evolved according to the master equation

$$\dot{\rho} = -i[H, \rho] + L\rho \tag{231}$$

with the Hamiltonian

$$H_I = iE(b^\dagger - b) + g_0(ab^\dagger c + a^\dagger b c^\dagger) \tag{232}$$

and the Lindblad operator $L = L_a + L_b + L_m$, where

$$L_a\rho = \kappa a\rho a^\dagger - \tfrac{\kappa}{2}a^\dagger a\rho - \tfrac{\kappa}{2}\rho a^\dagger a \tag{233}$$

$$L_b\rho = \kappa b\rho b^\dagger - \tfrac{\kappa}{2}b^\dagger b\rho - \tfrac{\kappa}{2}\rho b^\dagger b \tag{234}$$

$$L_m = \gamma c\rho c^\dagger - \tfrac{\gamma}{2}c^\dagger c\rho - \tfrac{\gamma}{2}\rho c^\dagger c. \tag{235}$$

The calculation for each trajectory was done in a displaced frame around the (analytically expected) mean amplitude of the mechanical oscillator and cavity modes, in order to reduce the required numerical Hilbert space dimension. Finally we averaged after an evolution time τ over all trajectories to obtain a density matrix $\sigma = \sum_j |\psi_j(\tau)\rangle\langle\psi_j(\tau)|$. With this density matrix we calculated the mean values $\langle\hat{n}\rangle_\sigma$ and $\langle\hat{n}^2\rangle_\sigma$, which in turn give the Fano factor F and the second order coherence function $g^{(2)}(0)$ according to equations (229) and (209). The evolution time was chosen as $\tau = 5/\gamma$ so that both mean values $\langle\hat{n}\rangle_\sigma$ and $\langle\hat{n}^2\rangle_\sigma$ had already relaxed to steady state while the phase has still not diffused away too far from ζ_0. In this time frame a small Hilbert space around the mean mechanical amplitude was sufficient for the simulation.

Part III

ION SPECTROSCOPY AND CLOCKS

6

PHOTON RECOIL SPECTROSCOPY

6.1 INTRODUCTION

Ion traps are ideal systems for spectroscopy experiments, as they allow to efficiently cool the motion of many atomic species so that Doppler broadening is drastically reduced. The motional state of ions with closed transitions, allowing for resolved sideband cooling, can even be cooled down to its quantum ground state. While ions or molecules without closed transitions cannot be sideband cooled directly, as the internal state would soon decay to a state invisible to the cooling laser, they can be cooled indirectly via a co-trapped ion (logic ion) with a closed transition: The spectroscopy ion's energy is transferred via Coulomb interaction to the logic ion, where it is dissipated by laser cooling.

Quantum logic spectroscopy [47] is a technique that allows to read out the spectroscopy signal of such an indirectly cooled ion via the logic ion: The excitation of the spectroscopy ion is transferred via the motional coupling to the logic ion, where it can be read out via electron shelving. For a spectroscopy transition with a short lifetime this transfer can take too long to faithfully transfer the signal. For this situation a modification of the quantum logic spectroscopy protocol was recently demonstrated [3], allowing for high precision spectroscopy of broad transitions.

In this photon recoil spectroscopy experiment the open transition of the spectroscopy ion is driven by a short laser pulse. Due to the recoil of the photon on the spectroscopy ion, a small momentum is transferred to the center of mass motion of the ion crystal. In contrast to the fast decay rate of the spectroscopy transition, the motional damping is negligible so that this signal does not decay on the timescale of the experiment. A series of n such identical pulses is periodically applied after each ion crystal oscillation so that the recoil momenta resonantly add up to a measurable signal. Finally the motional ground state probability $P(n)$ is transferred to the logic ion, where it can be read out. The photon recoil spectroscopy sequence is illustrated in Figure 18.

Varying the spectroscopy laser frequency ω_L a resonance curve is obtained to determine the transition's resonance ω_r. It turns out that because of the transition's momentum-dependent Doppler shift, this curve is not perfectly symmetric around ω_r. Using the standard two point sampling method explained in Figure 19, which measures both on the left and the right slope of the curve, this asymmetry leads to

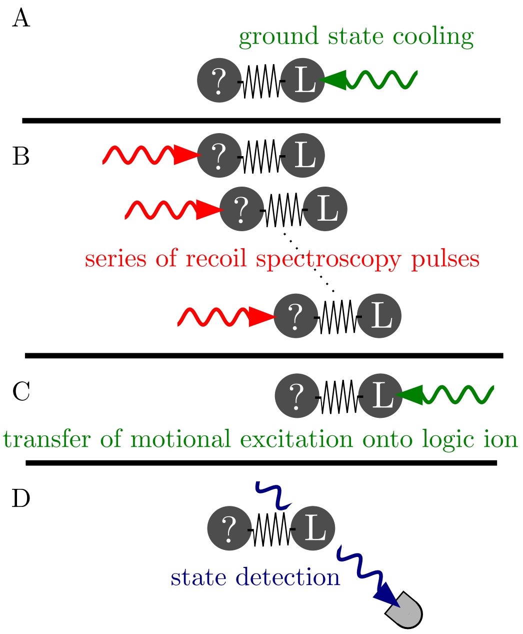
A
ground state cooling
?
L
B
?
L
series of recoil spectroscopy pulses
C
transfer of motional excitation onto logic ion
D
state detection

Figure 18: Illustration of Photon Recoil Spectroscopy sequence:
A) A motional mode of the ion crystal, consisting of the spectroscopy ion (left) and the logic ion (right), is cooled to its ground state using the logic ion's closed transition. B) A periodic sequence of spectroscopy pulses synchronized with the oscillation period of the normal mode is applied to the spectroscopy ion, exciting the ions' motion. The maximal signal is achieved with a laser frequency $\omega_l = \omega_r$ matching the resonance frequency. C) Using a red sideband pulse the ion crystal's motional excitation is transferred onto the logic ion. D) The spectroscopy signal is obtained via electron-shelving detection of the logic ion's internal state.

a systematic shift of the result. In this chapter we provide a careful theoretical analysis of the system dynamics to correctly determine ω_r from the resonance curve.

6.1.1 *Two point sampling method*

The experiment is performed for a fixed number of oscillations n_0 at varying laser frequency ω_l in order to determine the resonance frequency ω_r, where the excitation probability $P(\omega_l, n_0)$ has its maximum. As P does not change much [1] as a function of ω_l for $\omega_l - \omega_r \approx 0$, the signal from a direct maximization of P would be very weak. A better signal is obtained by finding the two frequencies $\omega_{l,+}(P_M) > \omega_{l,-}(P_M)$ as a function of the threshold value P_M, where $P(\omega_{l\pm}, n_0) = P_M$. As the signal $\partial_{\omega_l} P$ is usually maximal at $P_M = 0.5$, this is the most common choice. For a symmetric line shape, the resonance fre-

---

[1] Formally, the first derivative is zero at the maximum.

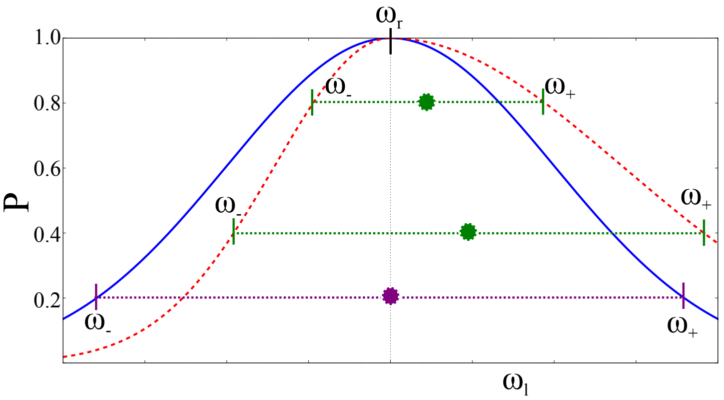

Figure 19: Illustration of the two point sampling method to determine the maximum of a resonance curve $P(\omega_l)$. The blue solid curve is symmetric around the resonance frequency ω_r. In the drawn example the purple marks indicate where the curve falls below a threshold of, in this example, $P_M = 0.2$ on the red side (ω_-) and on the blue side (ω_+) of the resonance, where the measurement data is taken. The average (indicated by a circle) at $(\omega_+ + \omega_-)/2$ is exactly at ω_r due to the symmetry of the curve for any value of P_M. Best results are achieved for P_M chosen such that the sensitivity of $\omega_\pm$ on P is maximized. This maximal slope of $\partial_{\omega_l} P$ is typically achieved around the half value $P_M \approx 0.5$.
The systematic shift arising for asymmetric line shapes is illustrated at the red dashed curve, which is resonant at the same frequency ω_r. The same two point sampling procedure then results in a shifted estimate for the resonance frequency, which even depends on the choice of the threshold value P_M, as shown by the green marks taken at $P_M = 0.8$ and $P_M = 0.4$.

quency can be determined by averaging, i.e. $\omega_r = (\omega_{l+} + \omega_{l-})/2$, as illustrated in Figure 19. In the photon recoil spectroscopy experiment this two point sampling method generates a systematic shift $\delta\omega_r = (\delta\omega_{l+} + \delta\omega_{l-})/2$, as the line shape is asymmetric due to the Doppler effect, which we explain in the following section.

6.2 THE THEORETICAL MODEL

In analogy to Section 2.2.3, we theoretically model the experiment in terms of a master equation $\dot{\rho} = \mathcal{L}\rho$ for the density matrix ρ of the system (consisting of the spectroscopy ion's internal energy levels and a mechanical mode of the ion crystal) with a Lindblad operator $\mathcal{L} = \mathcal{L}_m + \mathcal{L}_a + \mathcal{L}_l$, where $\mathcal{L}_m, \mathcal{L}_a, \mathcal{L}_l$ are detailed below. Restricting the model here to the selected normal mode, the ion crystal motion can be effectively described as one mechanical mode b with reference frequency ν and negligible coupling to the environment, thus the Lindblad operator for this degree of freedom is

$$\mathcal{L}_m\rho = -i\left[\nu b^\dagger b, \rho\right]. \tag{236}$$

We describe the spectroscopy ion as an effective two level system with ground state $|g\rangle$ and excited state $|e\rangle$ so that its Lindblad operator in a rotating frame for the transition at the laser frequency is

$$\mathcal{L}_a\rho = -i\left[-\frac{\Delta}{2}\sigma_z, \rho\right] + \Gamma D[\sigma_-]\rho, \tag{237}$$

where $\Delta = \omega_l - \omega_r$ is the detuning of the laser with respect to the resonance, Γ is the linewidth of the spectroscopy transition, the Pauli matrices are denoted with σ and $D[\sigma_-]\rho = \sigma_-\rho\sigma_+ - \frac{1}{2}\sigma_+\sigma_-\rho - \frac{1}{2}\rho\sigma_+\sigma_-$. The interaction between the internal and the motional degree of freedom can be turned on by the spectroscopy laser and is described by

$$\mathcal{L}_l\rho = -i\left[\frac{\Omega}{2}\sigma_- \exp\left(-i\eta(b+b^\dagger)\right) + h.c., \rho\right], \tag{238}$$

where Ω parameterizes the laser amplitude and η is the Lamb-Dicke parameter. Each of these short laser pulses of duration τ is followed by a period $T-\tau$ of free motion where $\mathcal{L}_l = 0$ so that the time evolution is synchronized to the mechanical oscillation period $T = 2\pi/\nu$.

6.3 EQUATION OF MOTION IN PHASE SPACE

It is convenient to switch for the mechanical mode to a phase space distribution along the lines of the framework introduced in Section 2.B.2 and Chapter 3 in order to derive a Fokker-Planck equation for its dynamics during the pulse. We choose here to work with the Wigner distribution $W(x,p)$ in the following, with the convention that $\hat{x} = \frac{1}{\sqrt{2}}(b+b^\dagger)$ is the position and $\hat{p} = -\frac{i}{\sqrt{2}}(b-b^\dagger)$ is the momentum of the normal mode. The object

$$w(x,p) = \frac{1}{\pi}\int \mathrm{d}y \langle x+y|\rho|x-y\rangle e^{-2iyp} \tag{239}$$

is a density matrix for the internal state, which depends on the mechanical oscillator's position in phase space. The states of both separate systems can be retrieved as

$$W(x,p) = \mathrm{Tr}_a\left(w(x,p)\right) \tag{240}$$

for the mechanical mode and

$$\rho_a = \mathrm{Tr}_b\left(\rho\right) = \int w(x,p)\mathrm{d}x\mathrm{d}p \tag{241}$$

for the internal state. To obtain the equation of motion for $w(x,p)$ we use the translation rules

$$\hat{b}\rho \to \left(\beta + \frac{1}{2}\frac{\partial}{\partial\beta^*}\right)w, \qquad \hat{b}^\dagger\rho \to \left(\beta^* - \frac{1}{2}\frac{\partial}{\partial\beta}\right)w. \tag{242}$$

from Section 2.A. Defining the scaled Lamb-Dicke parameter as $\bar{\eta} = \sqrt{2}\eta$, the terms $e^{\pm i\eta(b+b^\dagger)}\rho$ exactly translate to $e^{\pm i\bar{\eta}(x+\frac{i}{2}\partial_p)}w$, which we approximate by neglecting all terms of higher than first order in $\bar{\eta}\partial_p$. While this approximation is motivated because the higher order derivatives are very hard to treat analytically, it is ultimately justified by the fact that it reproduces the systematic shift. We note that the resulting approximate translation rules

$$\begin{aligned} e^{\pm i\eta(b+b^\dagger)}\rho &\rightarrow e^{\pm i\bar{\eta}x}\left(1 \mp \tfrac{\bar{\eta}}{2}\partial_p\right)w, \\ \rho e^{\pm i\eta(b+b^\dagger)} &\rightarrow e^{\pm i\bar{\eta}x}\left(1 \pm \tfrac{\bar{\eta}}{2}\partial_p\right)w \end{aligned} \tag{243}$$

provide a better approximation than the standard Lamb-Dicke approximation, where also the exponential functions in $\bar{\eta}x$ would be replaced by their first order approximation.

The equation of motion for $w(x,p)$ can now be written as $\dot{w} = (\mathcal{L}_m + \mathcal{L}_a + \mathcal{L}_i)\,w$ with (denoting the anticommutator of two operators with curly brackets)

$$\mathcal{L}_m w = \nu\left(\partial_x p - \partial_p x\right)w, \tag{244}$$

$$\mathcal{L}_a w = -i\left[-\frac{\Delta}{2}\sigma_z + \frac{\Omega}{2}\left(\sigma_+ e^{i\bar{\eta}x} + h.c.\right), w\right] + \Gamma D[\sigma_i]w, \tag{245}$$

$$\mathcal{L}_i w = \frac{\bar{\eta}\Omega}{4}\partial_p\left\{i\sigma_+ e^{i\bar{\eta}x} + h.c., w\right\}, \tag{246}$$

where we distributed the laser associated Lindblad operator $\mathcal{L}_l$ from equation (238) among the internal operator $\mathcal{L}_a$ (receiving all terms that leave the mechanical mode unchanged) and the interaction operator $\mathcal{L}_i$ (receiving the interaction terms).

The effect of the position-dependent phase $e^{i\bar{\eta}x}$ stemming from the driving field is easier to understand in the unitarily changed frame defined by

$$\tilde{w}(x,p) = e^{-i\bar{\eta}x\sigma_z/2}w(x,p)e^{i\bar{\eta}x\sigma_z/2}, \tag{247}$$

where it introduces a Doppler shift to the detuning $\Delta_{\text{dop}}(p) = \Delta - \bar{\eta}\nu p$ in $\mathcal{L}_a$. The Lindblad operators for $\tilde{w}$ take the form

$$\tilde{\mathcal{L}}_m \tilde{w} = \nu\left(\partial_x p - \partial_p x\right)\tilde{w}, \tag{248}$$

$$\tilde{\mathcal{L}}_a \tilde{w} = -i\left[-\frac{\Delta_{\text{dop}}(p)}{2}\sigma_z + \frac{\Omega}{2}\sigma_x, \tilde{w}\right] + \Gamma D[\sigma_i]\tilde{w}, \tag{249}$$

$$\tilde{\mathcal{L}}_i \tilde{w} = -\frac{\bar{\eta}\Omega}{4}\partial_p\left\{\sigma_y, \tilde{w}\right\}. \tag{250}$$

Conveniently, the Wigner distribution is still obtained as $W = \text{Tr}_a\left(\tilde{w}\right)$, in complete analogy to equation (240).

At this point a remark on the formalism is in order: We used here the framework introduced in Section 2.B.2, where the main system is a bosonic mode and described in a phase space picture. The ancilla system is described by means of a density matrix, which is finally adiabatically eliminated. In chapters 3 and 4 we develop and apply this framework to the standard optomechanical setup, where the ancilla is also a bosonic mode, while in the present ion trap case it is a two level system. We stress that the transformation (247), which reveals the Doppler induced shift in the ion case is very much analogous to the Semi-Polaron Transformation from equation (115), which allows for a correct treatment of the Kerr effect in self-sustained oscillations of the standard optomechanical system. Both transformation (115) and (247) cannot be efficiently performed in the standard density matrix picture, cf. Appendix 3.B. This shows the improved flexibility of the phase space formalism that allows to conveniently describe these subtle physical effects.

6.4 ADIABATIC ELIMINATION OF THE INTERNAL STATE

As the experiment is performed in the weak coupling limit $\bar{\eta}\Omega \ll \nu, \Gamma$, we solve the equation of motion iteratively in orders of $\tilde{\mathcal{L}}_i$, respectively $\bar{\eta}\Omega$. Formally we use an interaction picture with respect to $\tilde{\mathcal{L}}_a + \tilde{\mathcal{L}}_m$ and expand the Dyson series to second order in $\tilde{\mathcal{L}}_i$ to obtain the expression

$$\begin{aligned}\tilde{w}(\tau) =& e^{(\tilde{\mathcal{L}}_a+\tilde{\mathcal{L}}_m)\tau}\tilde{w}(0)\\ &+\int_0^\tau \mathrm{d}t e^{(\tilde{\mathcal{L}}_a+\tilde{\mathcal{L}}_m)(\tau-t)}\tilde{\mathcal{L}}_i e^{(\tilde{\mathcal{L}}_a+\tilde{\mathcal{L}}_m)t}\tilde{w}(0)\\ &+\int_0^\tau \mathrm{d}t\int_0^t \mathrm{d}t' e^{(\tilde{\mathcal{L}}_a+\tilde{\mathcal{L}}_m)(\tau-t)}\tilde{\mathcal{L}}_i e^{(\tilde{\mathcal{L}}_a+\tilde{\mathcal{L}}_m)(t-t')}\tilde{\mathcal{L}}_i e^{(\tilde{\mathcal{L}}_a+\tilde{\mathcal{L}}_m)t'}\tilde{w}(0)\end{aligned} \tag{251}$$

for the state after the pulse of duration τ. After this pulse the laser is turned off and the motional state evolves freely according to $\tilde{\mathcal{L}}_m$ for a period $T-\tau$. The internal state decays to its ground state as $T-\tau \gg 1/\Gamma$. Hence the state after a full mechanical oscillation is

$$\tilde{w}(T) = e^{\tilde{\mathcal{L}}_m(T-\tau)}\mathrm{Tr}_a\left(\tilde{w}(\tau)\right)\otimes|g\rangle\langle g| = e^{\tilde{\mathcal{L}}_m(T-\tau)}W(\tau)|g\rangle\langle g|. \tag{252}$$

As the internal state is prepared in the ground state also before the first pulse, we can write the state at times nT as $W^{(n)}(x,p)|g\rangle\langle g|$ for all $n \in \mathbb{N}_0$. Combining equations (251) and (252) and tracing out the internal state the motional state after n cycles is

$$\begin{aligned}W^{(n+1)} =& W^{(n)} + \int_0^\tau \mathrm{d}t\mathrm{Tr}_a\left\{e^{-\tilde{\mathcal{L}}_m t}\tilde{\mathcal{L}}_i e^{(\tilde{\mathcal{L}}_a+\tilde{\mathcal{L}}_m)t}|g\rangle\langle g|\right\}W^{(n)}\\ &+\int_0^\tau \mathrm{d}t\int_0^t \mathrm{d}t'\mathrm{Tr}_a\left\{e^{-\tilde{\mathcal{L}}_a t}\tilde{\mathcal{L}}_i e^{(\tilde{\mathcal{L}}_a+\tilde{\mathcal{L}}_m)(t-t')}\tilde{\mathcal{L}}_i e^{(\tilde{\mathcal{L}}_a+\tilde{\mathcal{L}}_m)t'}|g\rangle\langle g|\right\}W^{(n)}.\end{aligned} \tag{253}$$

Neglecting the commutator of $\tilde{\mathcal{L}}_a$ and $\tilde{\mathcal{L}}_m$ (justified because of the short pulse duration $\tau \ll 1/\nu$) this is evaluated as

$$\begin{aligned} W^{(n+1)} - W^{(n)} = &-\frac{\bar{\eta}\Omega}{2} \int_0^\tau \mathrm{d}t \partial_{p_t} \langle \sigma_y(t) \rangle W^{(n)} \\ &+ \frac{\bar{\eta}^2\Omega^2}{4} \int_0^\tau \mathrm{d}t \int_0^t \mathrm{d}t' \partial_{p_t} \partial_{p_{t'}} \mathrm{Re}\left[\langle \sigma_y(t) \sigma_y(t') \rangle \right] W^{(n)}, \end{aligned} \tag{254}$$

where we use the shorthand notation $\partial_{p_t} = \partial_p \cos(\nu t) - \partial_x \sin(\nu t)$ and $\sigma_y(t)$ is the solution of the optical Bloch equations corresponding to (249). The average is taken with respect to $|g\rangle\langle g|$. The time evolution of $\langle \sigma_y(t)\sigma_y(t') \rangle$ may be evaluated using the quantum regression theorem.

Due to the small shift per step ($\bar{\eta}\Omega\tau \ll 1$) it is a good approximation to turn equation (254) into Gaussian dynamics. As a step towards a Gaussian equation of motion, we can obtain a corresponding recursion relation making the Fokker-Planck ansatz $\partial_n(x, p, n)W = AW(x, p, n)$ with

$$A = \left[-\left(\partial_x d_x + \partial_p d_p \right) + \tfrac{1}{2} \left(\partial_{xx} D_{xx} + \partial_{pp} D_{pp} + 2\partial_{xp} D_{xp} \right) \right] \tag{255}$$

for the time evolution with dimensionless time $n = t/T$ implying $t = nT$. We demand that the resulting recursion relation $W(n+1) = e^{A\cdot 1} W(n)$ agrees with the corresponding relation (254) to second order in the derivatives, [2] to read off the coefficients

$$d_x = -\frac{\bar{\eta}\Omega}{2} \int_0^\tau \mathrm{d}t \sin(\nu t) \langle \sigma_y(t) \rangle, \quad d_p = -\frac{\bar{\eta}\Omega}{2} \int_0^\tau \mathrm{d}t \cos(\nu t) \langle \sigma_y(t) \rangle, \tag{256}$$

$$D_{xx} = \frac{\bar{\eta}^2\Omega^2}{2} \int_0^\tau \mathrm{d}t \int_0^t \mathrm{d}t' \sin(\nu t) \sin(\nu t') \mathrm{Re}\left[\langle \sigma_y(t) \sigma_y(t') \rangle \right] - d_x^2 \tag{257}$$

$$D_{pp} = \frac{\bar{\eta}^2\Omega^2}{2} \int_0^\tau \mathrm{d}t \int_0^t \mathrm{d}t' \cos(\nu t) \cos(\nu t') \mathrm{Re}\left[\langle \sigma_y(t) \sigma_y(t') \rangle \right] - d_p^2 \tag{258}$$

$$\begin{aligned} D_{xp} = &-\frac{\bar{\eta}^2\Omega^2}{4} \int_0^\tau \mathrm{d}t \int_0^t \mathrm{d}t' \left[\sin(\nu t) \cos(\nu t') - \sin(\nu t') \cos(\nu t) \right] \times \\ &\mathrm{Re}\left[\langle \sigma_y(t) \sigma_y(t') \rangle \right] - d_x d_p \end{aligned} \tag{259}$$

for the Fokker-Planck equation.

As the time evolution of σ_y in these integrals can be solved analytically along the lines of [114], this is in principle also possible for the drift and diffusion coefficients. We can however understand the essential physics of the systematic frequency shift even without this explicit solution as shown below.

---

[2] In effect the new relation is equally valid as (254), which was a second order approximation in the first place.

6.5 APPROXIMATE SOLUTION AS A GAUSSIAN TIME EVOLUTION

All drift and diffusion coefficients depend, possibly nonlinearly, on the momentum variable p through the Doppler shift in the detuning $\Delta_{\text{dop}}(p)$. In order to obtain an approximate Gaussian equation of motion, we therefore linearize as described below: In first order Lamb-Dicke expansion the drift in momentum d_p is Doppler shifted, and we expand it as

$$d_p(p) = d_p(0) + \frac{\partial d_p}{\partial \Delta_{\text{dop}}} \frac{\partial \Delta_{\text{dop}}}{\partial p} p = d_p(0) - g(\Delta_{\text{dop}}(p))p, \tag{260}$$

where g can be viewed as a Doppler shift induced (anti)damping for positive (negative) values of g. To obtain a linear dependence in p, we approximate g as

$$g(\Delta) = \bar{\eta}\nu \frac{\partial d_p}{\partial \Delta}(\Delta), \tag{261}$$

i.e. the derivative is evaluated at and with respect to Δ (which is fixed during each experimental run) instead of Δ_{dop}. We stress that $g(\Delta)$ is a function of the detuning and its sign depends on the side of the resonance: It is positive (negative) for red (blue) detuning. All other drift and diffusion coefficients show a weaker dependence on the momentum variable (of higher order in the Lamb-Dicke parameter), such that we neglect their dependence on p, set $\Delta_{\text{dop}} = \Delta$ in their evaluation and regard them as constants. Together with the approximation (261) the drift d_p is a linear function in p so that the approximate dynamics is Gaussian.

With the notation $\vec{R} = (\hat{x}, \hat{p})$, the first and second moments of the Wigner function can be compactly denoted with the displacement vector $\vec{r} = \langle \vec{R} \rangle$ and the matrix $\gamma_{ij} = \langle R_i R_j + R_j R_i \rangle - 2 r_i r_j$ with $i, j \in \{x, p\}$, which contains the covariances scaled by a factor of 2. $\vec{r}$ and γ follow the Gaussian dynamics

$$\dot{r}_x = d_x, \qquad \dot{r}_p = d_p(0) - g r_p \tag{262}$$

$$\dot{\gamma}_{xx} = 2D_{xx}, \qquad \dot{\gamma}_{pp} = 2D_{pp} - 2g\gamma_{pp}, \tag{263}$$

$$\dot{\gamma}_{xp} = 2D_{xp} - g\gamma_{xp}. \tag{264}$$

The experiment is initialized in the ground state, so that the initial conditions are $r_x = r_p = \gamma_{xp} = 0$ and $\gamma_{xx} = \gamma_{pp} = 1$ and the distribution is Gaussian. At dimensionless time n these moments evolve to

$$r_x = d_x n, \qquad r_p = \tfrac{1}{g}(1 - e^{-gn})d_p(0) \tag{265}$$

$$\gamma_{xx} = 1 + 2D_{xx}n, \qquad \gamma_{pp} = \tfrac{1}{g}(1 - e^{-2gn})2D_{pp} + e^{-2gn}, \tag{266}$$

$$\gamma_{xp} = \tfrac{1}{g}(1 - e^{-gn})2D_{xp}, \tag{267}$$

and the state remains Gaussian. As detailed in Section 2.A.4, the Husimi Q-function can be obtained from the Wigner function by convolution with a Gaussian. Using its definition as $Q(\alpha) = \frac{1}{\pi}\langle\alpha|\hat{\rho}|\alpha\rangle$ at $\alpha = 0$, we obtain for the excitation probability $P = \pi Q(0)$ of measuring the motion outside the ground state at time n and for a (bare) detuning Δ

$$P(n) = 1 - \left|\frac{1 + \gamma(n)}{2}\right|^{-\frac{1}{2}} \exp\left[\vec{r}(n)^T(1 + \gamma(n))^{-1}\vec{r}(n)\right], \tag{268}$$

where a dependence on Δ respectively $\omega_l = \omega_r + \Delta$ is implicitely given by the drift and diffusion parameters.

6.6 QUANTIFYING THE SYSTEMATIC SHIFT

In order to quantify (and thereby correct) the systematic shift $\delta\omega_r$, it is of course most reliable to numerically simulate the master equation. In order to understand its origin, we apply further approximations to derive a simple analytical equation for $\delta\omega_r$:

ONE DIMENSIONAL MODEL All x-related drift and diffusion coefficients are of higher order in τ/ν than the purely p-related coefficients due to the scaling with $\sin(\nu t)$ (as opposed to $\cos(\nu t)$) in the integration kernels (256)-(259) and are therefore neglected. Keeping only d_p and D_{pp} and expanding to first order in g, the approximate solution for the states displacement vector and covariance matrix is

$$r_x = 0, \qquad r_p = dn - \frac{gd}{2}n^2 \tag{269}$$

$$\gamma_{xx} = 1, \qquad \gamma_{pp} = 1 + 2(D_{pp} - g)n, \tag{270}$$

$$\gamma_{xp} = 0, \tag{271}$$

where $d = d_p(0)$. Inserting this solution into equation (268) yields

$$P(n) = 1 - \left[\frac{2}{1 + \gamma_{pp}}\right]^{1/2} \exp\left[-\frac{r_p(n)^2}{1 + \gamma_{pp}}\right]. \tag{272}$$

As for the parameter regime of the experiment $D_{pp} \ll |g|$, we approximate $D_{pp} \approx 0$ in the equation for $\gamma_p p$ and approximate the excitation probability as $P \approx P_0 + \delta P$, with

$$P_0 = 1 - \exp\left[d^2n^2/2\right], \qquad \delta P = \frac{gn}{2}\exp\left[d^2n^2/2\right]. \tag{273}$$

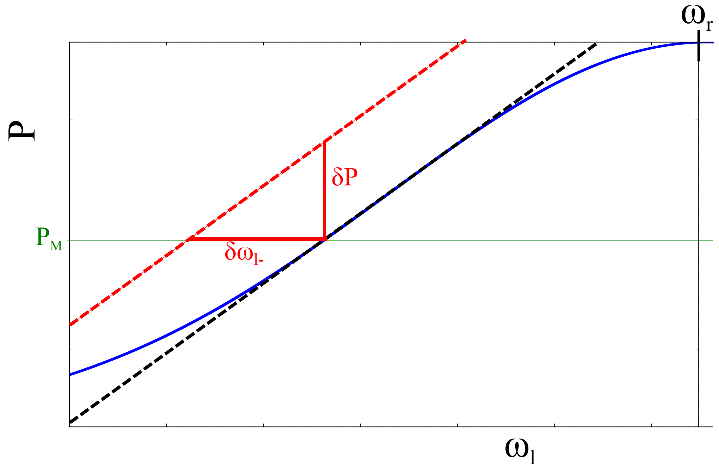

Figure 20: Illustration of the systematic frequency shift $\delta\omega_{l-}$ on the red side of the resonance ω_R according to equation (274). The blue line shows the symmetric part P_0 of the resonance curve, the green line indicates the chosen threshhold P_M. In zeroth order of the small asymmetric perturbation δP the value of ω_{l-} lies at the intersection. The lower dashed line linearizes the function around this intersection with a slope of $\partial_{\omega_l} P$. The shift of ω_{l-} may then be approximated by the red gradient triangle. The shift on the blue side is determined in complete analogy.

P_0 is the symmetric (with respect to Δ) excitation probability neglecting the Doppler shift and δP is the first order contribution in g of the antisymmetric shift. As $\frac{\delta P}{\delta\omega_{l-}} \approx \frac{\partial P}{\partial\Delta}$ in linear approximation, we obtain for the systematic shift on the left side of the resonance

$$\delta\omega_{l-} = \delta P \Bigg/ \frac{\partial P}{\partial\Delta} = \delta P \Bigg/ \left(n^2 d \partial_\Delta d\right), \qquad (274)$$

as illustrated in Figure 20. With relation (261) this yields $\delta\omega_{l-} = \bar{\eta}\nu/2dn$. For a given threshold value P_M and measurement time n the corresponding drift coefficient is, according to equation (273) (neglecting the damping g) given by $dn = \sqrt{-2\log(1-P_M)}$, so that $\delta\omega_{l-} = \frac{1}{2}\eta\nu/\sqrt{-\log(1-P_M)}$. In analogy, the same result is obtained for $\delta\omega_{l+}$ so that also the total systematic frequency shift of the resonance is

$$\delta\omega_r = \tfrac{1}{2}\eta\nu \Bigg/ \sqrt{-\log(1-P_M)}. \qquad (275)$$

Note that this simple function depends only on the (unscaled) Lamb-Dicke parameter η, the mechanical frequency ν and the measurement point P_M. Surprisingly, it is independent of the spectroscopy time per cycle, the number of cycles, the laser drive Ω and the width of the resonance Γ.

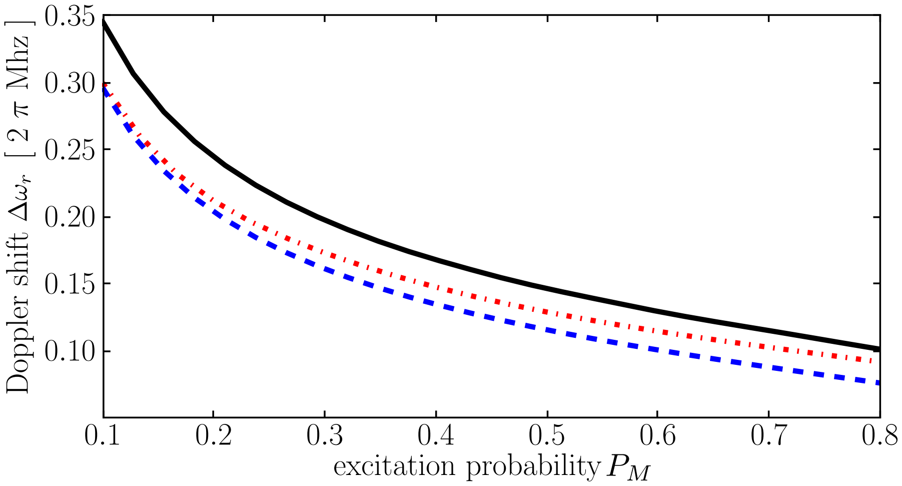

Figure 21: Systematic, Doppler effect induced shift of the measured resonance frequency ω_r as a function of the threshhold probability P_M used in the two point sampling method. The blue dashed curve follows the simple analytical equation (275) derived from model (a). The red dash-dotted line is obtained from the two dimensional, semi-analytical model (b). For comparison, the black continuous line represents the solution of a full numerical simulation of the master equation, model (c). The parameters used in this plot are Lamb-Dicke parameter $\eta = 0.1$, pulse duration $\tau = 50\text{ns}$, transition line width $\gamma = 140\text{MHz}$, laser strength $\Omega = 2\pi \times 7.88\text{MHz}$, mechanical frequency $\nu = 2\pi \times 1.92\text{MHz}$.

COMPARISON OF DIFFERENT MODELS For typical experimental parameters, we compare in Figure 21 the results for the shift from the following increasingly complex models:

(a) The simple-one dimensional model leading to the analytical equation (275).

(b) The coefficients for drift d and diffusion D, as well as the damping g are calculated numerically according to the approximate equations (256)-(259), from which the time evolution of the two dimensional model is obtained according to equations (265)-(267) to obtain the probability (268).

(c) The full master equation with two internal levels, given by the Lindblad operators (236)-(238) is simulated numerically using QuTiP.

We conclude that the analytical models are in good agreement with the numerical simulation and provide a good intuition to understand the experiment. In order to cancel the systematic shift in an actual high precision experiment, the optimal result is of course achieved by a numerical simulation tailored to the concrete system, taking into account as much structure from the internal energy levels as numerically possible. E.g. in [3] we simulated the 8 relevant internal levels of a $^{40}Ca^{+}$ ion, when measuring the $^{2}P_{1/2}$ to $^{2}S_{1/2}$ transition. The Zeeman broadening due to the external magnetic field as well as decay of the $^{2}P_{1/2}$ level to the $^{2}D_{3/2}$ level (which has to be repumped) is taken into account. This additional structure gives rise to minor deviations from the simple two-level model.

In future studies the analytical model may be used to optimize variations of the photon recoil spectroscopy method including e.g. initialization with a different initial state or a different shape of the excitation pulse.

7

QUANTUM ALGORITHMIC READOUT OF MULTI-ION CLOCKS

We note that the content of the following Sections 7.2 and 7.3 are based on the bachelor thesis [5] of Marius Schulte, where also a more detailed derivation can be found.

7.1 INTRODUCTION

Traditional atomic clocks are based on stabilizing an electronic signal to atomic transitions in the microwave regime. While the NIST-F1 Cs fountain, which defines today's time and frequency standard, operates in this regime, clocks based on optical transitions have been built with improved frequency accuracy and frequency stability by about two orders of magnitude.

Currently an optical lattice clock [115] holds the record in both categories. Optical clocks based on a single trapped ion [48, 49] have held the accuracy record before and are in competition for the definition of the next time standard. The optical lattice clock, consisting of thousands of neutral atoms, is very stable as the quantum noise can be averaged over many atoms. In contrast, the signal from a single-ion clock has to be averaged over many weeks to finally provide a result with a relative inaccuracy on the order of 10^{-18} for the frequency. In order to improve the stability and reduce the averaging time, the next step for ion based clocks is to increase the number of ions. In this chapter we introduce an efficient readout mechanism for multi-ion clocks.

Such a mechanism is necessary as most suitable clock ions cannot be read out directly. In reference [49] a quantum logic scheme was used to map the state of the single ion clock onto a logic ion of a different species where it can be measured. One could scale this up by sequentially reading out multiple clock ions onto a single logic ion. In order to speed up the process for a better clock stability, one could also provide a logic ion for each clock ion and thereby parallelize the process. In order to improve on these obvious extensions, we propose to make use of a quantum algorithm [116, 117] developed in the context of entanglement concentration that encodes the Hamming weight [1] of the N_C clock ions in a bitstring of $N_L = \log_2(N_C + 1)$ logic ions. The implementation can be done using a multi species Mølmer-Sørensen gate acting on all clock and logic ions.

---

[1] the number of excitations.

7.2 THE ABSTRACT AND IDEALIZED READOUT MECHANISM

Before discussing the readout, we briefly summarize the (idealized) clock mechanism: An external laser frequency ω is stabilized to the atomic transition frequency ω_0 of a two-level ion with levels $|0\rangle$ and $|1\rangle$. Using for example Ramsay interferometry [118], the probability of each ion j to populate the excited state $|1\rangle_j$ is $P(\omega)$ with a maximum at $P(\omega_0)$, which would be $P(\omega_0) = 1$ for a perfect sequence. In each clock cycle an estimate for ω_0 is obtained by means of the two point sampling method introduced in Section 6.1.1 and the laser frequency is updated accordingly. As mentioned in the introduction, the signal given by the number of excited clock ions

$$\hat{N} = \sum_{j=1}^{N_C} |1\rangle_j\langle 1| \otimes \mathbb{1} \tag{276}$$

has to be transferred to the logic ions, where it can be detected. We choose here a notation that decomposes the Hilbert space $\mathcal{H} = \mathcal{H}_C \otimes \mathcal{H}_L$ into clock ($\mathcal{H}_C$) and logic ($\mathcal{H}_L$) ions.

For simplicity we will assume that $N_L = \log_2(N_C + 1)$ perfectly matches, so that any possible number of excited clock ions can be encoded in the bitstring of logic ions $|j_1, j_2, ..., j_{N_L}\rangle_L$ with $j \in \{0, 1\}$. E.g. for $N_C = 3$ clock ions the possible number of excitations include $0, 1, 2, 3$ that can be encoded as $00, 01, 10, 11$ with $N_L = 2$ logic ions. Initializing the logic ions in the ground state for each ion $|0\rangle_L = |0, 0, ..., 0\rangle_L$, the operator U for the readout process must fulfill

$$U|n_j\rangle_C|0\rangle_L = |n_j\rangle_C|\mathrm{bin}(n)\rangle_L, \tag{277}$$

where $|n_j\rangle_C$ is any eigenstate of the operator $\hat{N}$ (measuring clock excitation number) with integer eigenvalue n and $|\mathrm{bin}(n)\rangle_L$ is the binary representation of n. Once the information is encoded in the logic ions, it can be read out with standard methods available on the logic species. The corresponding measurement operator acting on the logic ions takes the form

$$\hat{N}_{\mathrm{est}} = \mathbb{1} \otimes \sum_{j=1}^{N_L} 2^{j-1}|1\rangle_j\langle 1|. \tag{278}$$

For the idealized readout represented by U defined in equation (277), the logic ions' estimate $\hat{N}_{\mathrm{est}}$ of clock ion excitations perfectly reproduces the statistics of the original clock ion operator $\hat{N}$ from equation (276).

In constructing U, it is instructive to consider the quantum Fourier transformation of $|\mathrm{bin}(n)\rangle_L$, which is [119]

$$\mathcal{F}|\mathrm{bin}(n)\rangle_L = \frac{1}{\sqrt{2^{N_L}}} \bigotimes_{j=1}^{N_L} \left(|0\rangle + e^{i2\pi\cdot n2^{-j}}|1\rangle\right). \tag{279}$$

This representation, where the prefactor of $|0\rangle$ is constantly one and the prefactor of $|1\rangle$ obtains a phase given by the product of n (the number of excited clock ions) multiplied by a logic-ion-dependent value $\phi_j = 2\pi 2^{-j}$, suggests the following quantum algorithm [116, 117] for readout [2]:

1. Apply the quantum Fourier transformation on the logic ions, which are initially in the ground state, to bring each ion into the superposition of $|0\rangle$ and $|1\rangle$. Note that this transformation can be implemented using Hadamard gates on the single ions and no interaction is required. In summary the first step is
$$\left(\bigotimes_{j=1}^{N_L} |0\rangle \right) \rightarrow \left(\bigotimes_{j=1}^{N_L} |0\rangle + |1\rangle \right) \tag{280}$$
2. Perform a controlled rotation gate between each clock ion with each logic ion, so that logic ion j obtains a phase $\phi_j = 2\pi 2^{-j}$ conditioned on the excitation of the clock ion. Formally, with the definition $D_j = |0\rangle\langle 0| + e^{i\phi_j}|1\rangle\langle 1|$ the gate R_{kj} between clock ion k and logic ion j can be written as
$$R_{kj} = |0\rangle_k\langle 0| \otimes \mathbb{1}_j + |1\rangle_k\langle 1| \otimes D_j \tag{281}$$
and the R_{kj} have to be performed for each $k = 1, ..., N_C$ and $j = 1, ..., N_L$ to obtain
$$\left(\bigotimes_{j=1}^{N_L} |0\rangle + |1\rangle \right) \rightarrow \bigotimes_{j=1}^{N_L} \left(|0\rangle + e^{in\phi_j}|1\rangle \right), \tag{282}$$
the Fourier transformed encoding $\mathcal{F}|\text{bin}(n)\rangle_L$ of the bitstring, cf. equation 279. The order of execution is irrelevant as all R_{kj} commute.
3. Finally the inverse quantum Fourier transformation $\mathcal{F}^{-1}$ on the logic ions retrieves the desired bitstring $|\text{bin}(n)\rangle$,
$$\mathcal{F}|\text{bin}(n)\rangle_L \rightarrow \mathcal{F}^{-1}\mathcal{F}|\text{bin}(n)\rangle_L = |\text{bin}(n)\rangle_L. \tag{283}$$

7.3 PHYSICAL IMPLEMENTATION OF THE READOUT MECHANISM

The physical implementation of the algorithm steps 1 and 3 require operations on the logic ions only and can be solved with standard quantum information processing methods. Each of these steps requires $N_L - 1$ single species Mølmer-Sørensen gates, scaling thus logarithmically in the number of clock ions $N_C = 2^{N_L} - 1$. With a slight adjustment of the algorithm corresponding to the use of a different basis, the first step's Fourier transformation can even be skipped. This modification is presented in [4] to give the best possible solution for an experimental implementation, while we keep both Fourier transformations here for conceptual clarity.

---

[2] We drop in the following the state normalization for better readability.

We analyze in the following only the most costly step 2, which requires interaction between the clock and logic ions. For this purpose we write the controlled phase gate from equation (281) as $R_{kj} = e^{-iH_{kj}}$ with $H_{kj} = -\frac{1}{4}\phi_j \left(\mathbb{1} - \sigma_z\right)_k \otimes \left(\mathbb{1} - \sigma_z\right)_j$, which can be expanded into

$$H_{kj} = \tfrac{1}{4}\phi_j \left(-\mathbb{1} \otimes \mathbb{1} + \sigma_z(k) \otimes \mathbb{1} + \mathbb{1} \otimes \sigma_z(j) - \sigma_z(k) \otimes \sigma_z(j)\right). \quad (284)$$

The first and second term are irrelevant as they do not change the excitation number of the clock ions and do not act on the logic ions at all, but the second two terms have to be implemented: The term proportional to $\mathbb{1} \otimes \sigma_z(j)$ corresponds to a single qubit gate on logic ion j. The term proportional to $\sigma_z(k) \otimes \sigma_z(j)$ corresponds to a 2-qubit gate between different (logic and clock) species. Keeping thus only the relevant terms and using the fact that all operators commute, we write the full gate as $R = R_0 \cdot R_I$

$$R_0 = \exp\left(-i \sum_{k,j} \tfrac{1}{4}\phi_j \mathbb{1} \otimes \sigma_z(j)\right), \quad (285)$$

$$R_I = \exp\left(-i \sum_{k,j} -\tfrac{1}{4}\phi_j \sigma_z(k) \otimes \sigma_z(j)\right). \quad (286)$$

The non-interacting gate R_0 can be built with N_L single-qubit gates S_j, one for each logic ion, which is a routine operation with today's technology. The interaction gate R_I requires multi-species interaction and is the most demanding component of the experiment. We show in the following paragraph that it can be built with a single multi-ion interspecies Mølmer-Sørensen gate, which can be constructed as

$$T = \exp(-iS^2), \qquad S = \sum_{\alpha=L,C} \sum_{j=1}^{N_\alpha} d_{\alpha,j} \sigma_z^{\alpha,j}. \quad (287)$$

with appropriately chosen laser phases. The index α in Equation (287) refers to logic (L) or clock (C) ion. The coefficients of S are physically determined by

$$d_{\alpha,j} = \Omega_{\alpha j} \eta_{\alpha j} \sqrt{t/\delta}, \quad (288)$$

where $\Omega_{\alpha j}$ is the Rabi frequency given by the laser, $\eta_{\alpha j}$ is the Lamb-Dicke parameter, δ is the detuning from the respective sideband transition used in the gate and t is the gate duration.

For the Mølmer-Sørensen gate (287) to execute the gate operation (286) the coefficients $d_{\alpha,j}$ must fulfill

$$d_{C,k} d_{L,j} = -\pi 2^{-j+2} \quad (289)$$

$$d_{L,k} d_{L,j} = \pi n_{kj} \quad (k \neq j), \quad (290)$$

where n_{kj} must be integers in order to ensure that the gate effectively does not include gates between logic ions. [3] In order to fulfill condition (289), the sign of $\Omega_{\alpha j}$, which depends on the laser phase, must be chosen depending on the sign of the Lamb-Dicke parameter $\eta_{\alpha j}$. Minimizing the size of the largest coefficient in order to keep the gate duration as short as possible, the solution for the coefficients $d_{\alpha,j}$ is

$$\left|d_{Lj}\right| = \sqrt{\pi}2^{N_L-1-j}, \qquad \left|d_C\right| = \sqrt{\pi}2^{-N_L-1}. \tag{291}$$

Note that the d_C coefficient is identical for each clock ion.

7.4 CASE STUDY: Al^+-Ca^+ CLOCK

This section is a case study of a concrete experimental setup. We consider the minimal setup consisting of three clock ions and two logic ions. We choose Al^+ for the clock species, which has a narrow linewidth of 8 mHz in the transition ${}^1S_0 - {}^3P_0$ transition at 1.121 PHz [49], and Ca^+ as a suitable logic ion species. We must analyze the normal mode spectrum of such an ion crystal to find a mode that

A) has large enough Lamb-Dicke factors for all ions in order to establish an interaction.

B) and has a sufficiently large frequency gap $\Delta\nu$ from the next normal mode. This allows for an execution of the Mølmer-Sørensen gate of detuning $\delta \ll \Delta\nu$ undisturbed from the other modes. As the maximum applicable Rabi frequency must fulfill $|\eta\Omega| \ll \delta$, finding a large enough gap is important to minimize the gate execution time t.

7.4.1 *Normal modes for transversal oscillations*

We calculate the normal mode spectrum for the transversal oscillations of a two-species ion chain along the lines of [120]. In our example setup text two logic ions (Ca^+, mass $m_L = 40$amu, laser wavelength $\lambda_L = 729.1$nm) and three clock ions (Al^+, mass $m_C = 27$amu, laser wavelength $\lambda_C = 267.4$nm) are (softly) trapped along the crystal axis (z-axis). The trap frequency for the logic ions is $\nu_z^L = 2\pi 874$kHz. The asymmetry parameters are defined as $a = \nu_x^L/\nu_z^L$ and $a_{yx} = \nu_y^L/\nu_x^L$. We fix $a_{yx} = 5$ to suppress oscillations along the y-axis. The normal modes are calculated for different values of a for optimization, because we will use the oscillations in x-direction for the gate. As sketched in Figure 22 the clock ions (index $k = 2, 3, 4$) are placed in the middle and the logic ions (index $k = 1$ and $k = 5$) on the outside.

---

[3] A similar condition for the clock ions is not necessary again because the excitation statistics is not changed by the interaction.

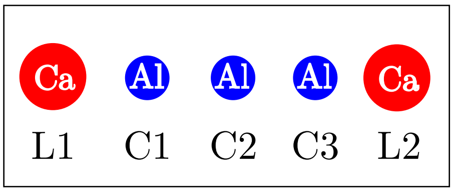

Figure 22: (a) Sketch of setup for a crystal of $N_C = 3Al^+$ clock ions between $N_L = 2Ca^+$ logic ions.

With masses $(m_1, m_2, m_3, m_4, m_5) = (m_L, m_C, m_C, m_C, m_L)$ the kinetic energy is given by

$$T(\vec{p}) = \sum_{k=1}^{5} \vec{p}_k^2 / 2m_k. \tag{292}$$

The potential energy due to the electrostatic component of the trap is the same for each ion, as all ions are singly charged (elementary charge q). Assuming a radially symmetric electrostatic trap we get a total electrostatic potential of [121]

$$V_S(\vec{x}) = \frac{1}{2} \sum_{k=1}^{5} \left(b_0 z_k^2 - \frac{1}{2} b_0 x_k^2 - \frac{1}{2} b_0 y_k^2 \right), \tag{293}$$

i.e.trapping in z-direction but repulsion in x- and y-direction of equal strength. The potential strength is parametrized by the parameter b_0, in units of energy divided by length squared. To keep the ions also radially trapped, an additional time-dependent radio frequency potential is used to create an effective potential in x and y direction

$$V_{RF}(\vec{x}) = \frac{1}{2} \sum_{k=1}^{5} \frac{m_L}{m_k} \left(b_x x_k^2 + b_y y_k^2 \right), \tag{294}$$

which unavoidably is mass-dependent. We parameterize the potential strength by b_x and b_y, in the same units as b_0. The parameters b_0, b_x and b_y are fully determined by the physical parameters of the setup: logic ion mass m_L, logic ion frequency ν_z^L and the asymmetry parameters a and a_{xy}. In addition to the trapping potential the ions interact via the Coulomb repulsion potential

$$V_I(\vec{x}) = \sum_{k>j} \frac{q^2}{4\pi\epsilon_0} \left| \vec{x}_k - \vec{x}_j \right|^{-1}. \tag{295}$$

With these definitions we can write the total energy of the system as $E(\vec{x}, \vec{p}) = T(\vec{p}) + V(\vec{x})$, where $V(\vec{x}) = V_S(\vec{x}) + V_{RF}(\vec{x}) + V_I(\vec{x})$.

We find the steady state position $\vec{x}_0$ of the ions by numerically minimizing [4] the potential energy V under the condition $z_1 < z_2 < ... < z_5$. In this study we choose large enough asymmetry parameters a so that the solution is always a linear chain without zigzag configuration [121, 120, 122]. As the oscillations around the steady state will be small, we use second order Taylor expansion to obtain an approximate harmonic potential. The different directions x, y and z decouple in this approximation. Denoting $p_k = m_k \dot{x}_k$ and $V_{kj} = \partial_{x_k x_j} V(\vec{x})\Big|_{\vec{x_0}}$ the energy for motion in x-direction only, is

---

[4] We use Powell's method as implemented in SciPy for the numerical minimization

$$E_x = \sum_{k=1}^{5} \tfrac{1}{2} p_k^2 / m_k + \sum_{k,j} \tfrac{1}{2} V_{kj} x_k x_j. \tag{296}$$

In coordinates with scaled position $\tilde{x}_k = \sqrt{m_k/m_0} x_k$ and momentum $\tilde{p}_k = \sqrt{m_0/m_k} p_k$, normalized to mass $m_0 = 1\text{amu}$, the kinetic term becomes diagonal and the potential transforms as $\tilde{V}_{kj} = \sqrt{m_0^2/m_k m_j} V_{kj}$. In these coordinates E_x reads

$$E_x = \sum_{k=1}^{5} \tfrac{1}{2} \tilde{p}_k^2 / m_0 + \sum_{k,j} \tfrac{1}{2} \tilde{V}_{kj} \tilde{x}_k \tilde{x}_j. \tag{297}$$

For the normal modes we numerically diagonalize $\tilde{V} = ODO^T$ with dimensionless orthogonal matrix O and diagonal matrix D of dimension frequency squared times mass. The eigenfrequencies are then given by

$$\nu_k = \sqrt{D_{kk}/m_0}. \tag{298}$$

In analogy to [120] the Lamb-Dicke factors of a mode k for an individual ion with index j are

$$\eta_j^k = \frac{2\pi}{\lambda_j} O_j^k \sqrt{\frac{\hbar}{2 m_j \nu_k}}, \tag{299}$$

with λ_j the wavelength of the laser addressing the j-th ion and O_{jk} the j-th entry of the eigenvector for the k-th normal mode.

7.4.2 *Results for our example configuration*

As mentioned, the asymmetry parameter a must not be chosen too small in order to avoid an unstable zig-zag configuration [121, 120, 122]. Choosing a too large results in a decoupling of the normal modes into modes involving either logic ions or clock ions only. In order to fulfill condition A) from the beginning of this section, we compromise at $a = 2.5$ and choose the normal mode with the highest frequency for optimal results. The corresponding Lamb-Dicke parameters are plotted in Figure 23 (b), assuming laser beam alignment with the x-axis. At $a = 2.5$ we read off $\eta_L = 0.007$ for for both logic, $\eta_{C1} = \eta_{C3} = 0.097$ for the outer clock ions and $\eta_{C2} = 0.113$ for the inner clock ion.

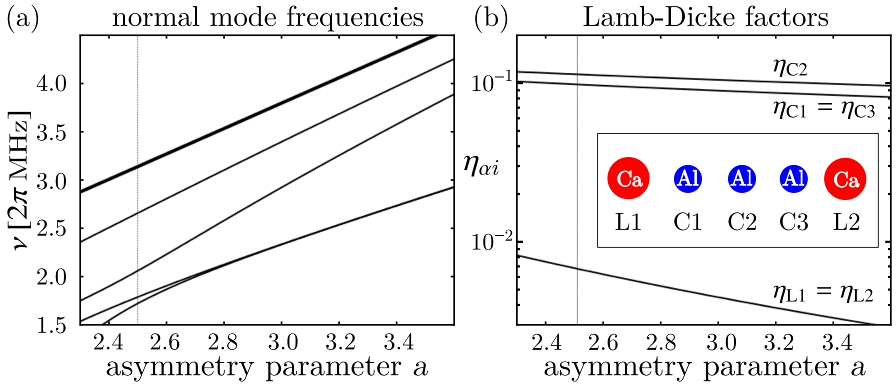

Figure 23: (a) Normal mode frequencies of transverse vibration for a crystal of $N_C = 3Al^+$ clock ions between $N_L = 2Ca^+$ logic ions (see inset of (b)) versus asymmetry parameter $a = \nu_x^L/\nu_z^L$ (ratio of transverse to axial trap frequencies for logic ions, $\nu_z^L = 2\pi 874\text{kHz}$).
(b) Lamb-Dicke factors η of the three clock (index C) and two logic ions (index L) for the normal mode of highest frequency (thick line in (a)). For large asymmetry parameter transverse motions of clock and logic ions decouple due to the mass-dependent transverse confinement. The dotted line in (a) and (b) marks the case studied in the text.

As depicted in Figure 23 (a), for $a = 2.5$ the highest frequency mode is at $\nu = 2\pi\, 3.14\text{MHz}$ and is gapped by $\Delta\nu = 2\pi\, 480\text{kHz}$ to the next mode. Choosing a Mølmer-Sørensen gate detuning $\delta = 2\pi\, 24\text{kHz}$, Rabi frequencies $\Omega_{L1} = 2\pi\, 500\text{kHz}$ and $\Omega_{L2} = 2\pi\, 250\,\text{kHz}$ for the logic ions and $\Omega_{C1} = \Omega_{C3} = 2\pi\, 4.51\text{kHz}$, $\Omega_{C2} = 2\pi\, 3.87\text{kHz}$ for the clock ions, the gate can be fully executed in 1ms. In this example the ratios set by condition B) from the beginning of this section are fulfilled as $\delta/\Delta\nu < 0.05$ and, citing the largest ratio, $|\eta\Omega|/\delta < 0.15$.

As the life time of the Ca^+ ions' $D_{5/2}$ state is 1.17 s and the gate execution time is 1ms, the readout errors due to spontaneous emission will be on the order of 0.001. We confirm this estimate with the numerical calculation in the next section.

7.5 NUMERICAL READOUT NOISE SIMULATION

Denoting the excitation probability of each ion after the Ramsay sequence with P, the quality of the clock is characterized (among other parameters such as the readout time) by the signal of the mean derivative $\partial_p \langle \hat{N}_{\text{est}} \rangle$ and the variance $\sigma^2_{\text{est}} = \langle \hat{N}^2_{\text{est}} \rangle - \langle \hat{N}_{\text{est}} \rangle^2$ of total readout excitations $\hat{N}_{\text{est}}$. The values are taken at a detuning where $P = 0.5$, as the clock is operated around that point for best results. For the ideal case of a perfectly noiseless ion gates, $\hat{N}_{\text{est}}$ follows the same statistics as $\hat{N}$ before readout with variance $\sigma^2 = \langle \hat{N}^2 \rangle - \langle \hat{N} \rangle^2$. Any indirect readout will add additional decoherence which decreases the signal and increases the variance. We define the readout quality $\zeta \leq 1$ as the ratio

$$\zeta = \left. \frac{\partial_p \langle \hat{N}_{\text{est}} \rangle / \sigma_{\text{est}}}{\partial_p \langle \hat{N} \rangle / \sigma} \right|_{P=0.5} \tag{300}$$

of the actual signal to noise ratio (SNR) including readout noise and the ideal SNR neglecting this noise.

Here we consider in particular noise sources due to spontaneous decay of the ions (mostly the logic ions) as well as additional phase noise of the logic ions, due to e.g. stray magnetic fields. The execution of the five-ion MS gate defined in equation (287) consumes by far the most time ($T = 1\text{ms}$ for our parameters) of the readout process, as its speed is limited by the restrictions on the Rabi frequency described in the main text. We thus simulate only these two noise sources and only while executing the five-ion MS gate.

The numerics is implemented using QuTiP [32, 33] for the master equation (302) below. The Hamiltonian for the gate operation is given by $H_{\text{MS}} = S^2/T$ with S from Eq. (287). Note that our numerical model operates on the qubit level and does not include possible decoherence due to excitations of other phonon modes. Defining for a given operator x a corresponding superoperator $D[x]\rho = x\rho x^\dagger - \frac{1}{2}x^\dagger x\rho - \frac{1}{2}\rho x^\dagger x$ acting on a density matrix ρ, the Lindblad operator for the spontaneous emission (index SE) of the j-th ion with lifetime τ_j is $L_{\text{SE}}^{(j)} = \tau_j^{-1} D[\sigma_-^{(j)}]$, where σ_- is the lowering operator. In total

$$L_{\text{SE}} = \sum_j L_{\text{SE}}^{(j)}. \tag{301}$$

The lifetime of the $D_{5/2}$ state in Ca+ is $\tau_L = 1.17s$ and lifetime of the ${}^3P_0$ clock state of Al+ is $\tau_C = 20.6s$. The dephasing due to other sources is characterized by a decay rate γ for all ions and the corresponding Lindblad operator is $L_B = \sum_j \gamma D[\sigma_z^{(j)}]$. The full master equation now reads

$$\dot{\rho} = -i[H, \rho] + L_{\text{SE}}\rho + L_B\rho. \tag{302}$$

While the T_1 coherence time of the logic ions is fixed, $T_1 = \tau_L$, the T_2 coherence time also depends on the experiment-dependent decay rate γ via $T_2 = 1/(0.5\tau_L^{-1} + 2\gamma)$. The numerical result for ζ as a function of T_2 is depicted in Figure 24. The best achievable value, reached at $T_2^* = 2T_1$, is $\zeta(T_2^*) = 0.999$ for a gate time of 1ms.

7.6 CONCLUSION

The resources for the readout mechanism presented in this chapter scale, in both number of gates and time, linearly with the number of

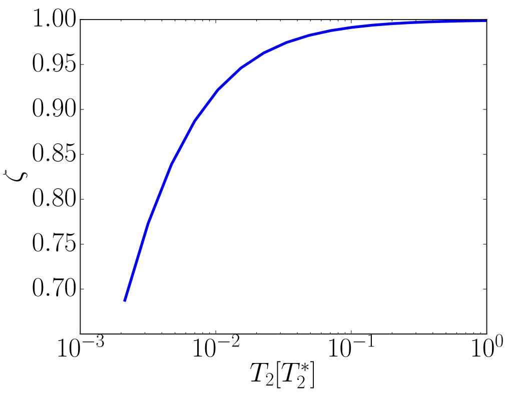

Figure 24: Plot of ζ from equation (300) for a gate time of 1ms. $T_2^* = 2T_1 = 2.34s$ is the maximal possible value of T_2 for the logic ions considering their finite lifetime due to spontaneous emission.

logic ions corresponding to a logarithmic scaling in the number of clock ions. In contrast, reading out each clock ion separately would scale linearly in the number of clock ions and would require cooling of the ion crystals motion after each readout bit. We expect that experimental implementation is feasible for more than 15 clock and 4 logic ions. With even more ions however, the spacing between mechanical modes becomes so small that active noise correction will be needed to cancel the effects from spectator modes.

8

CONCLUSION AND OUTLOOK

In the first part of this thesis we studied systems where an optical cavity degree of freedom excites a mechanical oscillator so that the system exhibits self-sustained limit cycles, similar to the state of a laser cavity excited by atoms. Accordingly, we modeled the process based on laser theory methods due to Haake and Lewenstein. Our description employs a new semi-polaron transformation, which allows for an explicit treatment of the Kerr effect in the context of limit cycles. One of the most interesting predictions for the standard optomechanical setup is that quantum signatures such as negative density of the Wigner distribution are observable even for surprisingly classical parameters, i.e. outside the single-photon strong-coupling regime, for strong cavity drive and rather large limit-cycle amplitudes.

Simulation of this parameter regime at the border of quantum and classical is numerically most challenging: For truly classical parameters it is possible to efficiently simulate the system with a stochastic equation in classical phase space. For truly quantum parameters the system can be simulated on a small Hilbert space. For the border regime of large oscillations on the scale of the harmonic oscillator's zero point fluctuation we developed an algorithm based on Quantum Jump Trajectories as implemented in QuTiP. It dynamically adapts the numerical Hilbert space following the present state of the system, allowing for the verification of our analytical results for previously unaccessed parameters with high mechanical amplitude and many photons in the cavity.

We concluded the first part of the thesis on optomechanical limit cycles with the proposition to use a setup where a second cavity enhances the nonlinearity in order to significantly ease the requirements on detection of phonon antibunching.

We hope that the perspective for quantum signatures in phonon lasing outside the single-photon strong-coupling regime may help to develop future experiments aiming for the demonstration of these effects for example with optomechanical crystals. The laser theory based analytical model developed in the first part can be applied in future projects e.g. for the study of the synchronization of limit cycles in the quantum regime, to describe the Kerr effect's influence on laser cooling dynamics but also for the investigation of similar physical systems such as trapped ions.

In the second part of the thesis, where we turned to trapped ion systems, one such project is realized for the analytical description of the photon recoil spectroscopy experiment: Exciting an ion crystal's motion via the recoil on absorption of a photon, the resonance of a broad ion (or molecule) transition is measured with unprecedented precision. To realize this high precision a systematic shift must be corrected. We adapted the analytical model from part one to trapped ions and derived a Fokker-Planck equation modeling the ion motion. This allows to understand the systematic shift as a result of the Doppler effect, where both drift and diffusion must be taken into account. A future perspective is to use the model for improving the photon recoil experiment, optimizing e.g. over different pulse shapes or possibly nonclassical initial states of motion.

Finally we analyzed the proposition for a quantum algorithmic readout mechanism for multi-ion optical clocks. The most important operation of the mechanism can be realized with a single multi-species Mølmer-Sørensen gate. In a case study with an Al-Ca clock we show that such a readout can be efficiently experimentally realized. Multi ion clocks will soon be built and it will be interesting to further improve the readout mechanism especially when scaling up the number of ions.

In conclusion, the rapid experimental progress in optomechanical experiments offers the exciting perspective to see realizations of both quantum signatures on macroscopic scales and quantum record accuracy metrology applications as studied in this thesis in near future experiments.

BIBLIOGRAPHY

[1] N. Lörch, J. Qian, A. Clerk, F. Marquardt, and K. Hammerer, Physical Review X **4**, 011015 (2014).

[2] N. Lörch and K. Hammerer, accepted at Physical Review A (2015), arXiv:1502.04112 .

[3] Y. Wan, F. Gebert, J. B. Wübbena, N. Scharnhorst, S. Amairi, I. D. Leroux, B. Hemmerling, N. Lörch, K. Hammerer, and P. O. Schmidt, Nature communications **5**, 3096 (2014).

[4] M. Schulte, N. Lörch, I. D. Leroux, P. O. Schmidt, and K. Hammerer, arXiv:1501.06453 (2015).

[5] M. Schulte, *Abfragestrategien in Multi-Ionen Uhren*, Bachelor thesis, University of Hannover, Germany (2014).

[6] H. D. Zeh, Foundations of Physics **1**, 69 (1970).

[7] W. H. Zurek, Physics Today Progress in Mathematical Physics, **44**, 36 (1991).

[8] M. Arndt and K. Hornberger, Nature Physics **10**, 271 (2014).

[9] A. D. O'Connell, M. Hofheinz, M. Ansmann, R. C. Bialczak, M. Lenander, E. Lucero, M. Neeley, D. Sank, H. Wang, M. Weides, J. Wenner, J. M. Martinis, and A. N. Cleland, Nature **464**, 697 (2010).

[10] G. C. Ghirardi, A. Rimini, and T. Weber, Physical Review D **34**, 470 (1986).

[11] R. Penrose, Philosophical Transactions of the Royal Society A: Mathematical, Physical and Engineering Sciences **356**, 1927 (1998).

[12] H. Everett, Reviews of Modern Physics **29**, 454 (1957).

[13] M. Aspelmeyer, T. J. Kippenberg, and F. Marquardt, Reviews of Modern Physics **86** (2014).

[14] M. Aspelmeyer, T. J. Kippenberg, and F. Marquardt, *Cavity Optomechanics*, edited by M. Aspelmeyer, T. J. Kippenberg, and F. Marquardt (Springer Berlin Heidelberg, 2014).

[15] J. D. Teufel, T. Donner, D. Li, J. W. Harlow, M. S. Allman, K. Cicak, A. J. Sirois, J. D. Whittaker, K. W. Lehnert, and R. W. Simmonds, Nature **475**, 359 (2011).

[16] J. Chan, T. P. M. Alegre, A. H. Safavi-Naeini, J. T. Hill, A. Krause, S. Gröblacher, M. Aspelmeyer, and O. Painter, Nature **478**, 89 (2011).

[17] E. Verhagen, S. Deléglise, S. Weis, a. Schliesser, and T. J. Kippenberg, Nature **482**, 63 (2012).

[18] T. A. Palomaki, J. W. Harlow, J. D. Teufel, R. W. Simmonds, and K. W. Lehnert, Nature **495**, 210 (2013).

[19] T. A. Palomaki, J. D. Teufel, R. W. Simmonds, and K. W. Lehnert, Science **342**, 710 (2013).

[20] K. W. Murch, K. L. Moore, S. Gupta, and D. M. Stamper-Kurn, Nature Physics **4**, 561 (2008).

[21] T. P. Purdy, R. W. Peterson, and C. A. Regal, Science **339**, 801 (2013).

[22] T. Carmon, H. Rokhsari, L. Yang, T. Kippenberg, and K. J. Vahala, Physical Review Letters **94**, 223902 (2005).

[23] M. Tomes and T. Carmon, Physical Review Letters **102**, 113601 (2009).

[24] I. S. Grudinin, A. B. Matsko, and L. Maleki, Physical Review Letters **102**, 043902 (2009).

[25] I. S. Grudinin, H. Lee, O. Painter, and K. J. Vahala, Physical Review Letters **104**, 083901 (2010).

[26] G. Bahl, J. Zehnpfennig, M. Tomes, and T. Carmon, Nature communications **2**, 403 (2011).

[27] G. Anetsberger, E. M. Weig, J. P. Kotthaus, and T. J. Kippenberg, Comptes Rendus Physique **12**, 800 (2011).

[28] S. Zaitsev, A. K. Pandey, O. Shtempluck, and E. Buks, Physical Review E **84**, 046605 (2011).

[29] O. Suchoi, K. Shlomi, L. Ella, and E. Buks, Physical Review A **91**, 1 (2015).

[30] J. D. Cohen, S. M. Meenehan, G. S. MacCabe, S. Groblacher, A. H. Safavi-Naeini, F. Marsili, M. D. Shaw, and O. Painter, Nature **520**, 522 (2015).

[31] F. Haake and M. Lewenstein, Physical Review A **27**, 1013 (1983).

[32] J. R. Johansson, P. D. Nation, and F. Nori, Computer Physics Communications **183**, 16 (2011).

[33] J. Johansson, P. Nation, and F. Nori, Computer Physics Communications **184**, 1234 (2013).

[34] M. Metcalfe, Applied Physics Reviews **1**, 31105 (2014).

[35] D. Leibfried, R. Blatt, C. Monroe, and D. J. Wineland, Rev. Mod. Phys. **75**, 281 (2003).

[36] R. Blatt and C. F. Roos, Nat Phys **8**, 277 (2012).

[37] A. D. Ludlow, M. M. Boyd, J. Ye, E. Peik, and P. O. Schmidt, , 86 (2014).

[38] J. Laane, *Frontiers of Molecular Spectroscopy* (Elsevier, 2011).

[39] V. B. Braginsky and F. Y. A. Khalili, *Quantum Measurements* (Cambridge University Press, 1995).

[40] M. Pitkin, S. Reid, S. Rowan, and J. Hough, "Gravitational wave detection by Interferometry (Ground and Space)," (2011).

[41] K. J. Vahala, Nature **424**, 839 (2003).

[42] M. Eichenfield, J. Chan, R. M. Camacho, K. J. Vahala, and O. Painter, Nature **462**, 78 (2009).

[43] D. E. Chang, C. A. Regal, S. B. Papp, D. J. Wilson, J. Ye, O. Painter, H. J. Kimble, and P. Zoller, Proceedings of the National Academy of Sciences of the United States of America **107**, 1005 (2010).

[44] D. M. Stamper-Kurn, in *Cavity Optomechanics* (Springer, 2014) pp. 283–325.

[45] C. A. Regal, J. D. Teufel, and K. W. Lehnert, Nat Phys **4**, 555 (2008).

[46] S. Kolkowitz, A. C. Bleszynski Jayich, Q. P. Unterreithmeier, S. D. Bennett, P. Rabl, J. G. E. Harris, and M. D. Lukin, Science **335**, 1603 (2012).

[47] P. O. Schmidt, T. Rosenband, C. Langer, W. M. Itano, J. C. Bergquist, and D. J. Wineland, Science **309**, 749 (2005).

[48] W. H. Oskay, S. A. Diddams, E. A. Donley, T. M. Fortier, T. P. Heavner, L. Hollberg, W. M. Itano, S. R. Jefferts, M. J. Delaney, K. Kim, F. Levi, T. E. Parker, and J. C. Bergquist, Physical Review Letters **97** (2006).

[49] C. W. Chou, D. B. Hume, J. C. J. Koelemeij, D. J. Wineland, and T. Rosenband, Physical Review Letters **104** (2010).

[50] R. Hudson, Reports on Mathematical Physics **6**, 249 (1974).

[51] A. Mandilara, E. Karpov, and N. J. Cerf, Physical Review A - Atomic, Molecular, and Optical Physics **79** (2009).

[52] A. Mari and J. Eisert, Physical Review Letters **109** (2012).

[53] C. Gardiner and P. Zoller, *Quantum Noise: A Handbook of Markovian and Non-Markovian Quantum Stochastic Methods with Applications to Quantum Optics (Springer Series in Synergetics)* (Springer, 2004).

[54] F. Petruccione and H.-P. Breuer, *The Theory of Open Quantum Systems* (Oxford University Press, 2007).

[55] S. G. Hofer, W. Wieczorek, M. Aspelmeyer, and K. Hammerer, Physical Review A **84**, 052327 (2011).

[56] T. Kippenberg, H. Rokhsari, T. Carmon, A. Scherer, and K. Vahala, Physical Review Letters **95**, 033901 (2005).

[57] C. Metzger, M. Ludwig, C. Neuenhahn, A. Ortlieb, I. Favero, K. Karrai, and F. Marquardt, Physical Review Letters **101**, 133903 (2008).

[58] G. Anetsberger, O. Arcizet, Q. P. Unterreithmeier, R. Rivière, A. Schliesser, E. M. Weig, J. P. Kotthaus, and T. J. Kippenberg, Nature Physics **5**, 909 (2009).

[59] F. Marquardt, J. Harris, and S. Girvin, Physical Review Letters **96**, 103901 (2006).

[60] S. Zaitsev, O. Gottlieb, and E. Buks, Nonlinear Dynamics **69**, 1589 (2012).

[61] J. B. Khurgin, M. W. Pruessner, T. H. Stievater, and W. S. Rabinovich, Physical Review Letters **108**, 223904 (2012).

[62] J. B. Khurgin, M. W. Pruessner, T. H. Stievater, and W. S. Rabinovich, New Journal of Physics **14**, 105022 (2012).

[63] M. Dykman and M. Krivoglatz, Physica Status Solidi (b) **68** (1975).

[64] M. Ludwig, B. Kubala, and F. Marquardt, New Journal of Physics **10**, 095013 (2008).

[65] K. Vahala, Physical Review A **78**, 023832 (2008).

[66] D. A. Rodrigues and A. D. Armour, Physical Review Letters **104**, 053601 (2010).

[67] A. D. Armour and D. A. Rodrigues, Comptes Rendus Physique **13**, 440 (2012).

[68] J. Qian, A. A. Clerk, K. Hammerer, and F. Marquardt, Physical Review Letters **109**, 253601 (2012).

[69] P. D. Nation, Physical Review A **88**, 053828 (2013).

[70] M. Lax, Physical Review **160**, 290 (1967).

[71] J. B. Khurgin, Physics **3**, 16 (2010).

[72] P. Meystre, Annalen der Physik **525**, 215 (2013).

[73] P. Rabl, Physical Review Letters **107**, 063601 (2011).

[74] A. Nunnenkamp, K. Bø rkje, and S. M. Girvin, Physical Review Letters **107**, 063602 (2011).

[75] I. Wilson-Rae, N. Nooshi, W. Zwerger, and T. J. Kippenberg, Physical Review Letters **99**, 093901 (2007).

[76] D. W. C. Brooks, T. Botter, S. Schreppler, T. P. Purdy, N. Brahms, and D. M. Stamper-Kurn, Nature **488**, 476 (2012).

[77] A. H. Safavi-Naeini, S. Gröblacher, J. T. Hill, J. Chan, M. Aspelmeyer, and O. Painter, Nature **500**, 185 (2013), arXiv:1302.6179 .

[78] G. D. Mahan, *Many-Particle Physics (Physics of Solids and Liquids)* (Springer, 2000).

[79] P. D. Drummond and D. F. Walls, Journal of Physics A: Mathematical and General **13**, 725 (1980).

[80] A. Mari and J. Eisert, Physical Review Letters **103**, 213603 (2009).

[81] C. Genes, D. Vitali, P. Tombesi, S. Gigan, and M. Aspelmeyer, Physical Review A **77**, 033804 (2008).

[82] R. Ghobadi, A. R. Bahrampour, and C. Simon, Physical Review A **84**, 033846 (2011).

[83] S. Aldana, C. Bruder, and A. Nunnenkamp, Physical Review A - Atomic, Molecular, and Optical Physics **88**, 10 (2013), arXiv:1306.0415 .

[84] G. Heinrich, M. Ludwig, J. Qian, B. Kubala, and F. Marquardt, Physical Review Letters **107**, 043603 (2011).

[85] Y. M. Golubev and I. V. Sokolov, Journal of Experimental and Theoretical Physics **60**, 234 (1984).

[86] Y. M. Golubev, Journal of Experimental and Theoretical Physics **80**, 212 (1995).

[87] J. McKeever, A. Boca, A. D. Boozer, J. R. Buck, and H. J. Kimble, Nature **425**, 268 (2003).

[88] S. Y. Kilin and a. B. Mikhalychev, Physical Review A - Atomic, Molecular, and Optical Physics **85** (2012).

[89] S. Barnett and P. Knight, Physical Review A **33** (1986).

[90] J. I. Cirac, Phys. Rev. A **46**, 4354 (1992).

[91] J. Dalibard, Y. Castin, and K. Mø lmer, Physical Review Letters **68**, 580 (1992).

[92] R. Dum, P. Zoller, and H. Ritsch, Physical Review A **45**, 4879 (1992).

[93] K. Mø lmer, Y. Castin, and J. Dalibard, Journal of the Optical Society of America B **10**, 524 (1993).

[94] T. E. Oliphant, Computing in Science & Engineering **9**, 10 (2007).

[95] P. D. Nation, J. R. Johansson, M. P. Blencowe, and A. J. Rimberg, Phys. Rev. E **91**, 013307 (2015).

[96] A. H. Safavi-Naeini and O. Painter, New Journal of Physics **13**, 013017 (2011).

[97] M. Ludwig, A. H. Safavi-Naeini, O. Painter, and F. Marquardt, Physical Review Letters **109**, 063601 (2012).

[98] X. Xu, M. Gullans, and J. M. Taylor, Phys. Rev. A **91**, 013818 (2015).

[99] P. Kómár, S. D. Bennett, K. Stannigel, S. J. M. Habraken, P. Rabl, P. Zoller, and M. D. Lukin, Physical Review A - Atomic, Molecular, and Optical Physics **87** (2013).

[100] V. Braginsky, S. Strigin, and S. Vyatchanin, Physics Letters A **287**, 331 (2001).

[101] X. Chen, C. Zhao, S. Danilishin, L. Ju, D. Blair, H. Wang, S. P. Vyatchanin, C. Molinelli, A. Kuhn, S. Gras, T. Briant, P.-F. Cohadon, A. Heidmann, I. Roch-Jeune, R. Flaminio, C. Michel, and L. Pinard, Phys. Rev. A **91**, 33832 (2015).

[102] H. Wu, G. Heinrich, and F. Marquardt, New Journal of Physics **15**, 1 (2013), arXiv:1102.1647 .

[103] S. L. Danilishin, S. P. Vyatchanin, D. G. Blair, J. Li, and C. Zhao, Phys. Rev. D **90**, 122008 (2014).

[104] L. Ju, C. Zhao, Y. Ma, D. Blair, S. L. Danilishin, and S. Gras, Classical and Quantum Gravity **31**, 145002 (2014).

[105] H. Wang, Z. Wang, J. Zhang, S. K. Özdemir, L. Yang, and Y.-X. Liu, Physical Review A **90**, 053814 (2014).

[106] H. Jing, S. K. Özdemir, X.-Y. Lü, J. Zhang, L. Yang, and F. Nori, Phys. Rev. Lett. **113**, 053604 (2014).

[107] A. Mari, A. Farace, and V. Giovannetti, arXiv:1407.8364 (2014).

[108] A. H. Safavi-Naeini, J. T. Hill, S. Meenehan, J. Chan, S. Gröblacher, and O. Painter, Physical Review Letters **112**, 153603 (2014).

[109] S. M. Meenehan, J. D. Cohen, S. Gröblacher, J. T. Hill, A. H. Safavi-Naeini, M. Aspelmeyer, and O. Painter, Phys. Rev. A **90**, 011803 (2014).

[110] F. Marquardt, J. P. Chen, A. A. Clerk, and S. M. Girvin, Physical Review Letters **99**, 093902 (2007).

[111] J. Chan, A. H. Safavi-Naeini, J. T. Hill, S. Meenehan, and O. Painter, Applied Physics Letters **101**, 081115 (2012).

[112] H. Sekoguchi, Y. Takahashi, T. Asano, and S. Noda, Optics Express **22**, 916 (2014).

[113] H. J. Kimble, M. Dagenais, and L. Mandel, Physical Review Letters **39**, 691 (1977).

[114] H. R. Noh and W. Jhe, Optics Communications **283**, 2353 (2010).

[115] B. J. Bloom, T. L. Nicholson, J. R. Williams, S. L. Campbell, M. Bishof, X. Zhang, W. Zhang, S. L. Bromley, and J. Ye, Nature **506**, 71 (2014).

[116] C. H. Bennett, H. J. Bernstein, S. Popescu, and B. Schumacher, **53**, 20 (1995).

[117] P. Kaye and M. Mosca, Journal of Physics A: Mathematical and General **34**, 6939 (2001).

[118] N. F. Ramsey, Physical Review **78**, 695 (1950).

[119] M. Nielsen and I. Chuang, *Cambridge Series on Information and the Natural Sciences*, Vol. 1 (Cambridge Univ Press, 2000).

[120] G. Morigi and H. Walther, The European Physical Journal D **269**, 261 (2001).

[121] D. Kielpinski, B. King, C. Myatt, C. Sackett, Q. Turchette, W. Itano, C. Monroe, D. Wineland, and W. Zurek, Phys. Rev. A **61**, 32310 (2000).

[122] J. P. Home, Advances in Atomic, Molecular and Optical Physics **62**, 1 (2013).